UNIVERSITÀ DEGLI STUDI DI PADOVA

UNIVERSITA' DEGLI STUDI DI PADOVA

DIPARTIMENTO DI SCIENZE CHIMICHE

CORSO DI DOTTORATO DI RICERCA IN SCIENZE MOLECOLARI
CURRICOLA IN SCIENZE CHIMICHE
XXX CICLO

SCREENING ON THE FUNCTIONALIZATION OF CARBON NANOSTRUCTURES AND THEIR COMPATIBILIZATION IN POLYMER-BASED COMPOSITE MATERIALS

Coordinatore: **Ch.mo Prof. Leonard Jan Prins**

SUPERVISORE**: Ch.mo Prof. Enzo Menna**

Dottorando**: Nicola Vicentini**

Contents

Abbreviations:

CNSs: Carbon nanostructures,

CNTs: carbon nanotubes,

SWCNTs: single wall carbon nanotubes,

MWCNTs: Multi wall carbon nanotubes,

RGO: Reduced graphene oxide,

CNHs: Carbon nanohorns,

NCP: N-Cyclohexyl-2-pyrrolidone,

NMP: N-Methyl-2-pyrrolidinone,

PLLA: Polylactic acid,

DMF: Dimethylformamide,

THF: Tetrahydrofuran,

DCM: Dichloromethane,

EtOH: Ethanol,

MeOH: Methanol,

TGA: Thermogravimetric analysis,

DLS: Dynamic light scattering,

FT-IR: Fourier Transform Infrared spectroscopy,

UV-Vis-NIR: Ultraviolet-Visible-Near Infrared spectroscopy,

NMR: Nuclear magnetic resonance,

SEM: Scanning electron microscopy,

TEM: Transmission electron microscopy,

EPR: Electron paramagnetic resonance,

AFM: Atomic force microscopy,

CAFM: Conductive atomic force microscopy,

Abstract:

Composites of carbon nanostructures (CNSs) and biocompatible polymers are promising materials for a series of advanced technological applications, ranging from biomedicine and bioelectronics to smart packaging and soft robotics. In this thesis, we present three types of organic-functionalized CNSs, namely 4-methoxyphenyl functionalized multi-walled carbon nanotubes, carbon nanohorns and reduced graphene oxide, used as nanofillers for the preparation of homogeneous and well-dispersed composites of poly(l-lactic acid), a biocompatible and biodegradable FDA-approved polymer. A thorough characterization of the composites is given in terms of calorimetric response, electrical and mechanical properties. Significant differences are observed among the different types of CNS nanofillers, underlying the key role played by the nanoscale shape, and distribution of the components in driving the macroscopic behavior of the composite material. Surface properties are probed through advanced atomic force microscopy techniques, on both flat substrates (films) and confined systems (nanofibers). All these composites are found to be fully biocompatible when tested as scaffolds for supporting the proliferation, and differentiations of human neuronal precursor cell line SH-SY5Y, and of human Circulating Multipotent stem Cells (hCMCs). Prototypes of Nerve Guide Conduits (NGCs) for *in vivo* tests were also designed, and obtained using the material based on functionalized Multi Walled Carbon Nanotubes (MWCNTs), and tested on mice, finding promising results. We also propose the functionalization of MWCNTs with “functional” organic groups (4-benzoic acids and styrene), and performed an additional derivatization on them respectively through an amidation reaction, and a “grafting from” polymerization. The so obtained CNSs are promising for the preparation of more complex composite materials. Finally, we analyzed the reaction pathway of the Tour functionalization of CNSs, and we hypothesized that the real reaction scheme could be a balance between two different pathways.

Riassunto:

Le nanostrutture di carbonio (CNS) e i polimeri biocompatibili sono materiali molto promettenti in un grande numero di applicazioni tecnologicamente avanzate, che vanno dalla biomedicina e bioelettronica, allo *smart packaging* e alla robotica *soft*. In questa tesi presentiamo la funzionalizzazione organica tramite addizione della p-metossianilina di 3 diverse CNS: i nanotubi di carbonio a parete multipla, i nanoconi di carbonio e il grafene ossido risotto. Questi materiali sono impiegati come additivi per la preparazione di materiali compositi nanostrutturati a base di acido polilattico (PLLA). In questa tesi è riportata una completa caratterizzazione in termini di proprietà termiche, elettriche e meccaniche. Sono evidenti differenze significative tra le tre nanostrutture e sul loro effetto sulle proprietà dei compositi; ciò sottolinea il ruolo chiave giocato dalla morfologia e forma a livello nanometrico nell'interazione nanostruttura-polimero e quindi nella determinazione delle caratteristiche finali del composito. La superfice dei materiali è stata caratterizzata tramite AFM e CAFM sia nella forma di film piatti sia nella forma di nanofibre ottenute tramite eletrospinning. Sono state quindi testate le proprietà di biocompatibilità e induzione/controllo della differenziazione sia su cellule umane neuronali (SH-SY5Y), sia su cellule staminali umane (hCMCs). I materiali a base di nanotubi di carbonio a parete multipla (MWCNT) ottenuti sono stati utilizzati per la preparazione di prototipi di *nerve guide conduits* (NGC) per operazioni *in-vivo* su topi, ottenendo risultati molto promettenti. Presentiamo anche la funzionalizzazione dei MWCNT con 2 gruppi organici "funzionali" (l'acido p-benzoico e lo stirene) sui quali è stata effettuata una derivatizzazione aggiuntiva sfruttando rispettivamente una reazione di ammidazione e una reazione di polimerizzazione "*grafting from*". Infine abbiamo analizzato lo schema di reazione della funzionalizzazione di Tour delle CNS a abbiamo ipotizzato che la reale via sintetica sia costituita da due differenti vie in equilibrio tra di loro.

1 Introduction

1.1 Carbon nanostructures

Among graphite, and diamond, that are the most common allotropes found in nature, carbon hasmany other allotropes. Among them, there are the so-called carbon nanostructures (CNSs): materials that are obtaining a particular interest in these last years in many research worldwide. Typical example of CNSs are fullerenes, carbon nanotubes, and graphene, but it should be noted that a wider variety of structures is available, like carbon nanohorns, nano diamonds, and nano onions.

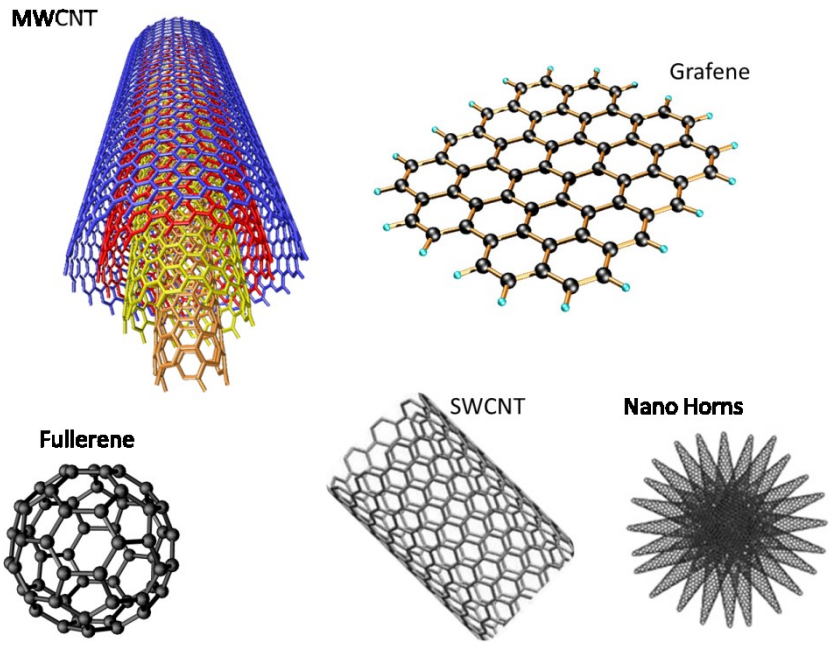

Figure 1-1: Structure of the most common CNSs.

1.1.1 Structure of CNSs

All the different CNSs are characterized by their unique shape and morphology but share the same basic structure based on a sp^2 lattice.

Fullerene

Fullerenes are the CNSs with the closest behavior to a molecule. The most common and studied fullerene consist of 60 sp^2-hybridized carbon atoms organized in hexagons and pentagons to give a spherical shape to the molecule, which is sometimes referred to as buckyball.

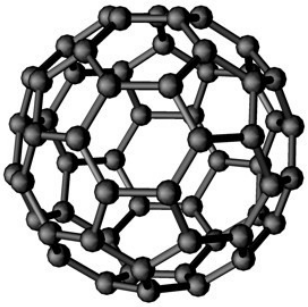

Figure 1-2: Molecular structure of fullerene.

Higher order fullerenes are possible, with combinations of 70 or more atoms.

Fullerenes are the most reactive CNSs because the spherical shape gives the highest strain to the π orbitals, that are responsible for the chemical behavior of the molecule (see below for more details). Given the optoelectronic properties of C_{60}, it can be used as an optical limiter because of the multi photon absorption, and non linear behavior with high intensity lasers. Fullerenes have been studied also as photosensitizers, and used as electron acceptors for solar cells, and light harvesting systems.

Graphene

Graphene is an ideal infinite single sheet of graphite, with all the carbon atoms in the sp^2-hybridized state, creating a planar hexagon lattice confined in two dimensions. This unique structure has the interesting property that at the *K* point of the reciprocal lattice the conduction, and the valence band intersect each other, thus making graphene a zero band gap semiconductor. In principle, this would allow ballistic conduction inside the sheet, so this single layer of carbon atoms candidates itself for electronic applications.

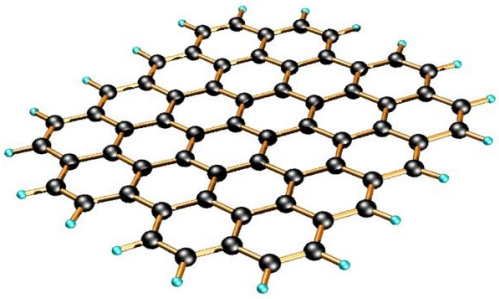

Figure 1-3: Structure of graphene.

By means of a bottom up approach, the production of graphene sheets through chemical vapor deposition (CVD) is the best technique to obtain a material close to the model, although with some limitations. Of course it is impossible to obtain an infinite sheet of carbon atoms, so the biggest defect of real graphene is the external border of

the structure; in order to keep the model reliable, the study of real graphene must be confined to a sufficiently small area of the sheet, so that the borders are enough far away, hence negligible. For this reason, true graphene is yet hardly implemented in technological devices, as it is limited to very controlled conditions, and quite small amounts, suitable for fundamental scientific studies only.

Given the promising properties, but also the compromising limitations of graphene, new approaches to its production, and handling were studied. Most of them are based on a top down approach, where graphite is used as starting material.

During this thesis work, studies were performed on reduced graphene oxide (rGO), so its production is described in detail in this section. Alternative methods like mechanical or chemical exfoliation should be mentioned, where viscous friction or small molecules able to produce gas are exploited to separate the layers of graphite.

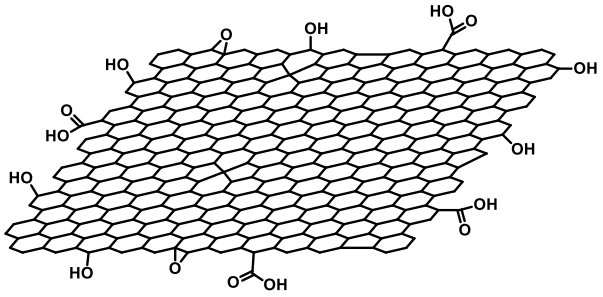

Figure 1-4: Schematic representation of a single player of RGO.

The production of rGO starts with the oxidation of graphite using strongly oxidant solutions, usually a combination of phosphoric acid, sulphuric acid and potassium permanganate. This process oxidizes the layers of graphite, and induces an increased spacing between the layers that enables the intercalation of water between the planes. A further step is required to turn graphite oxide into graphene oxide where, by means of mechanical stirring or sonication, the expanded multilayer structure is separated into single sheets or few layers graphene oxide. It must be noted that all the aforementioned procedures can be quite destructive for the starting material, that is not only exfoliated, but also fractioned into small flakes. It is then necessary to restore the sp^2 network to regain the electrical properties of graphene, as graphene oxide (GO) is an insulator, due to the lack of the shared π orbital network. The most common method found in literature is the chemical reduction of GO by means of hydrazine, but many other strategies are possible, including thermal, plasma or high intensity light pulses reduction. It is important to understand that the process is never completely reversible: there is always a residual component of defects and oxides that lowers the quality of the structure. Furthermore, the final material is hardly a single layer of

graphene, but rather a stack of few layers with residual defects. As the percentage of oxygen and the number of layers decreases, the cost of the material gets higher.

Trading quality for quantity of available material, it is possible to work with milligrams or even grams of rGO, thus opening the road to study chemical reactions, and surface modification of graphene for technological applications.

Carbon nanotubes

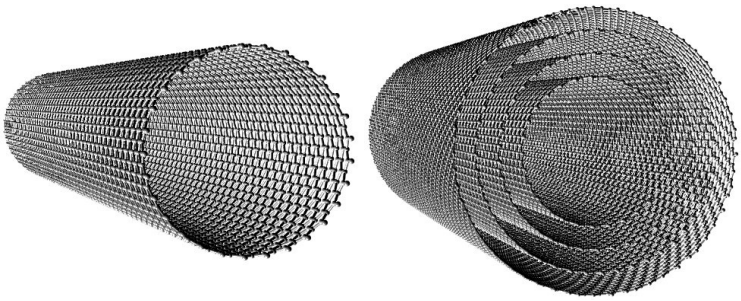

Figure 1-5: Structure of SWCNTs and MWCNTs.

Carbon nanotubes (CNTs) can be thought as hollow cylinders of graphene sheets. There are many ways to roll a sheet into a cylinder, and the properties of the CNT vary greatly with the diameter, and the microscopic structure of the tube. CNTs are usually separated in two categories depending on the number of sidewalls: single walled carbon nanotubes (SWCNTs), whose electronic properties are related to the nanotubes construction, and multi walled carbon nanotubes (MWCNTs), that are a conductive and robust nanostructure with averaged properties compared to the variety of SWCNTs. It is convenient to describe SWCNTs in terms of the chiral vector around which the nanotube is rolled.

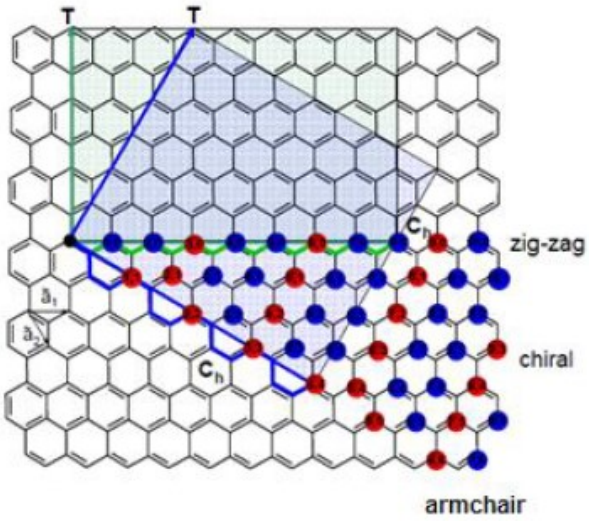

Figure 1-6: Chiral vector construction.[1]

The chiral vector is defined as:

$$C = na_1 + ma_2$$

where a_1 , and a_2 are the basis vectors of the unit cell separated by an angle of 60° due to the hexagonal honeycomb lattice of graphene.

The pair of integers (*n,m*) defines the nanotube structure. The so-called armchair structure hasindex *n* = *m,* and is denoted (*n,n*), while the zig-zag structure hasindex (*n,*0). Those two kinds of CNT are the only achiral tubes, while all the other combination defined by (*n,m*) indexes are chiral tubes with chiral angle given by:

$$\theta = cos^{-1}\left[\frac{n + m/2}{\sqrt{n^2 + nm + m^2}}\right]$$

By these two indexes that define the chiral vector, it is possible to determine the diameter, the unit cell, the number of carbon atoms, as well as the size and shape of the Brillouin zone.

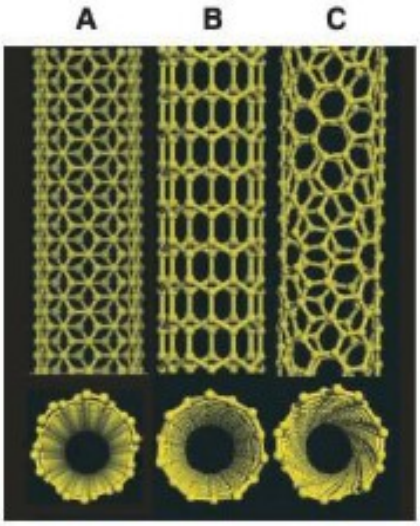

Figure 1-7: Examples of SWCNTs with different chirality.

SWCNTs can be either metallic, if they have an armchair structure, or semiconducting if *n*−*m* is a multiple of 3.[2] CNTs are produced at high temperatures using metals as catalyst for the nucleation and growth of the tube. Many processes have been developed exploiting different precursors: arc discharge, and laser ablation use an elemental carbon target, while HiPco, CoMoCAT, and CVD growth have molecular precursors like carbon monoxide, or hydrocarbon gases as methane or acetylene. The most used processes nowadays are HiPco, and CoMoCAT because they afford high yields and quality nanotubes, while laser ablation, and arc discharge are almost

dismissed, due to the heterogeneous products, and demanding process parameters, with temperatures up to 1200°*C,* and 4000°*C* respectively.

SWCNTs production, and properties were described so far, as they are the highest quality CNTs, but also the most difficult to handle. In order to fully make use of the electrical properties of SWCNTs it is necessary to purify the mixture of CNTs to remove the metallic catalyst. Furthermore, an extraction procedure is required to separate the metallic and semiconducting fractions. The purification process usually requires the oxidation of metal particles, in order to remove them as metal oxides, and of carbonaceous fragments. This procedure can be quite harsh, and introduces oxygenated defects on the side walls, such as hydroxyl, carboxylic or carbonyl groups.

Given the high cost of purified SWCNTs, when applications do not require a semi-conducting behavior, MWCNTs are a good alternative.

MWCNTs are conductive, and have an extraordinary high Young modulus, up to the TPa range. The overall conductivity of MWCNTs is lower than SWCNTs, as the amount of sp^2 carbon is lower, due to a higher density of defects. Nevertheless, they're still excellent nanoparticles for composite materials, as they can still be considered an almost one dimensional particle, given the radius-lenght ratio. Furthermore, MWCNTs are cheaper, and can be handled more easily than SWCNTs for a medium-large scale production.

One of the main problems related to the implementation of CNSs into new technologies is the difficulty to handle these materials, especially in solution, where they go towards aggregation due to Wan Der Walls forces, and high surface-volume ratios. The chemical modification of CNTs can be an efficient route towards the implementation in new functional materials.

1.2 CNSs functionalization

The chemical modification of CNSs can greatly affect the solution stability of a CNS. The grafting of small molecules with proper affinity with the solvent or medium where the CNSs are dispersed can prevent the aggregation, and allow homogeneous dispersion of the CNSs. The reactivity of CNSs is generally similar to that of electron-poor olefins. So, the principal reactions are additions of nucleophiles or radicals, cycloaddition reactions, hydrogenations, and halogenations. The chemical modification of the CNSs can be performed through several reactions: figure shows some synthetic routes to introduce functional groups on the CNSs.

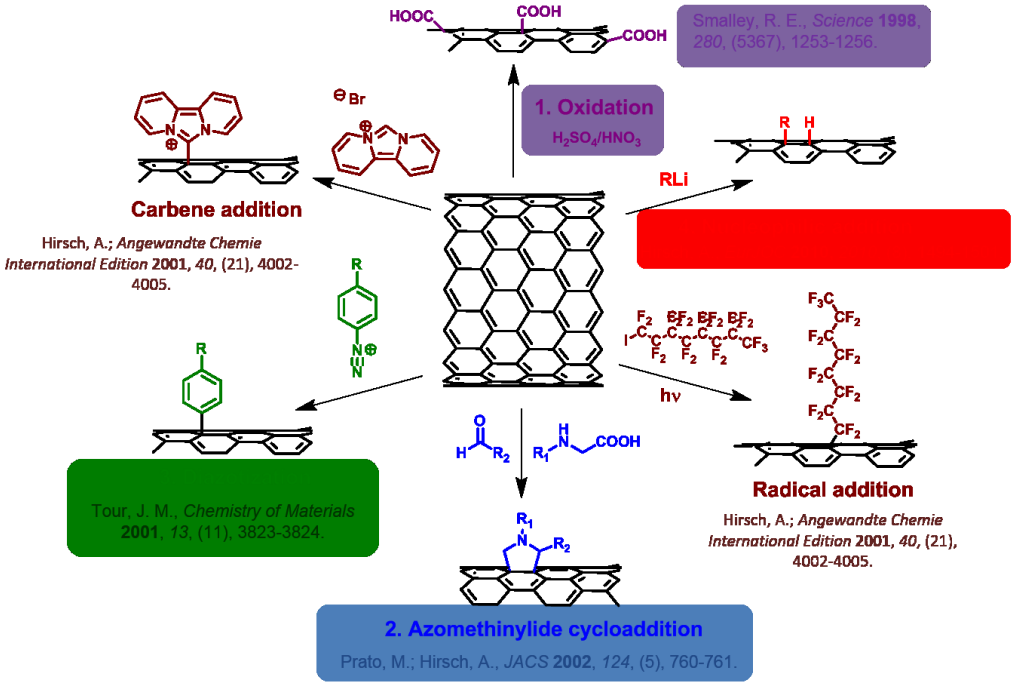

Figure 1-8:CNSs chemical modification synthetic routes.

The oxidative method (reaction 1 in figure) is the most common way to introduce carboxylic acids on the surface of CNTs by a two-step treatment. Many variations of this method are found in literature, based on the extent of oxidation desired; the common principle is that the first step provides the purification from metal residue by oxidation with nitric acid at reflux for several hours. This step is followed by filtration, and washing of the product in order to remove the smaller carbonaceous fragments and metal oxides. The second step provides the reduction of the heterogeneous oxygen defects to charboxylic acids through piranha solution.[3] The resulting CNTs are highly damaged, since very aggressive solutions are used to induce the oxidation. The control over the final product is obtained by the timing of each step, even though it is only a qualitative control.[4] The oxidation of the CNSs is widely used because it affords a reproducible chemical behavior of the CNSs, even though some of their properties are lost during the process.

Except for graphene, CNSs have an extensive conjugated π system characterized by a non-planar conformation. This curvature of the structure determines pyramidalization, and misalignment between the π orbitals, with strong effects on the reactivity of CNSs. The pyramidalization of carbon atoms is quantified by the θ_p angle defined as:

$$\theta_p = (\theta_{\sigma\pi} - 90)^\circ$$

So, for a sp^2 carbon atom θ_p is 0°, but for a sp^3 is 19.47°.

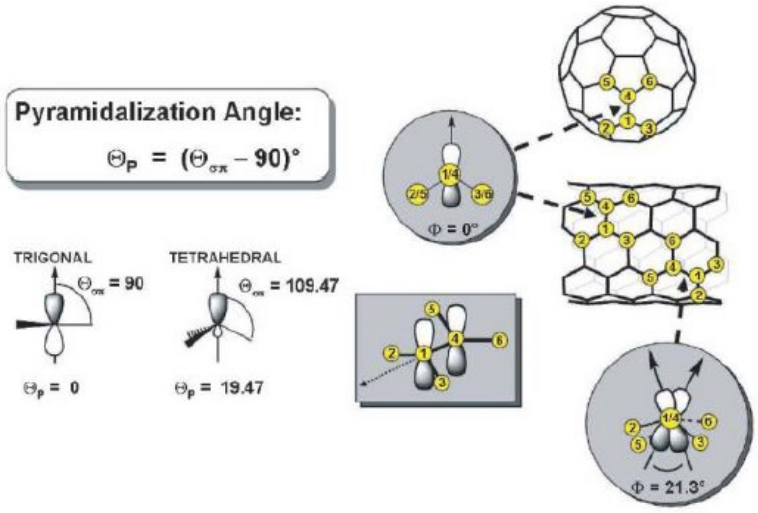

Figure 1-9: Pyramidalization and misalignment of CNSs[5].

This is the phenomenon that gives to CNSs their typical reactivity of electron-poor olefins, as this distortion of the π system brings to a reduction of the electron density on the convex surface of the bended structure.

Misalignment of p orbitals is quantified by the ϕ angle between the atomic p_z orbitals involved in the π bond formation.

These distortions induced by curvature generate local tensions in the sp^2 lattice, so reactions that convert sp^2 carbon atom into less strained sp^3 atoms are favored thanks to tension release.

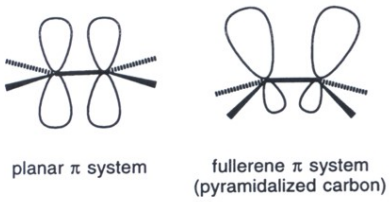

Figure 1-10: Orbital strain.

General approaches to the functionalization of CNSs can be grouped into two categories: (a) covalent attachment of chemical groups onto the π-conjugated backbone, and at defect sites located either onto the graphitic surface or at the edges, and (b) non-covalent adsorption or wrapping of various functional molecules onto the external surface.[6] The attachment of proper residues to the surface of CNSs can bring solubility, and induce the disentanglement of aggregates, thus also favoring homogeneous mixing with polymeric matrices.[7] Moreover, a solubilizing functionalization can allow the removal of impurities trapped inside bundles.[8] On the

other hand, chemical modification of CNSs can modify their native features, thus bringing to the loss of certain properties, but also providing new ones, which may cause their better integration into inorganic, organic, and biological systems.

1.2.1 **Covalent functionalization**

Covalent functionalization is based on the intrinsic reactivity of CNS sp^2 carbon networks, and on the possible presence of different kinds of defects on the external surface of CNSs. The degree of aggregation of the starting material is a crucial point too, since it determines the exposure of the surface to reagents. Pristine sp^2 structure of CNTs, and fullerenes is generally more reactive than that of graphene, due to the curvature-induced strain.[9] Among the most common reactions used for the functionalization of CNSs, Prato reaction, namely the 1,3-dipolar cycloaddition of azomethine ylides (AmYs), provides a convenient mean to get soluble, and functional derivatives.[10] The resulting pyrrolidine rings introduced on the CNS surface can carry a wide variety of functional groups, and allow the simultaneous attachment of different moieties. Usually, 1,3-dipolar cycloaddition reactions on CNSs are carried out on a small scale, owing to long reaction times, and big amounts of solvents required to disentangle, and disperse the starting materials. To mitigate this problem, our group reported on the alternative use of flow chemistry,[11] since continuous processes are intrinsically easier to scale up than their flask counterparts, besides offering a safer processing, and the opportunity to rapid reaction screening and optimization using relatively small amounts of reagents.[12]

Aryl diazonium derivatives (either pre-formed as diazonium salts, or generated *in situ*) are also a valuable family of reactive species for the functionalization of CNSs.[13] The reaction is fast, and effective, resulting in C-C bond formation at the graphitic surface and consequent generation of single-site sp^3 defects. Nevertheless, the involvement of diazonium salts hampers full exploitation of this process, due to the risks associated with the manipulation of these potentially explosive derivatives.

The flow methodology was also extended to the addition of diazonium salts to SWCNTs.[14] Besides reducing processing times, the flow approach allows controlling the degree of CNT functionalization, leading to products with enhanced solubility that retain the electronic properties of the pristine tubes. Such features make these derivatives ideal candidates for applications related to organic electronics or photovoltaics.

Defects on CNSs can be already present or deliberately created, as reactive sites for the subsequent functionalization, through an assortment of oxidation reactions.[4] Typical defects are carboxylic groups at the edges of CNTs, and GO or RGO, which can be used to graft molecules through the formation of amide or ester bonds, and hydroxyl or

epoxide groups available respectively for esterification, and epoxide ring-opening reactions.[15] Oxygenated groups resulting from CNT oxidation, and naturally found in GO also provide solubility in water and polar solvents (GO is undoubtedly a water soluble CNS).

Attachment of proper chains, such as poly(ethylene glycol) (PEG), can effectively help to disentangle CNTs in order to achieve solubility and to improve the dispersion in a polymeric matrix.[16]

Microwave irradiation has also been proposed as a fast, and scalable protocol for the covalent functionalization of CNSs. Microwave irradiation may allow to perform reactions in solvent-free conditions, and, compared to conventional thermal methods, reduces reaction times, and gives rise to higher degrees of functionalization. For more details, we address the reader to more specific contributions.[17]

1.2.1.1 Tour reaction: diazotization of CNSs

Tour et al. proposed a functionalization based on the addition of aryl derivatives to CNTs starting from primary aryl amines (anilines) through diazotization reaction.[13b] The corresponding diazonium salt is first isolated as a tetrafluoroborate salt, and then added to a CNTs dispersion at room or slightly higher temperature. This procedure is inconvenient because it requires the isolation of an unstable and light-sensitive aryl diazonium salt. It has been demonstrated that an equivalent functionalization is obtained, in the presence of SWCNTs, by treating in situ aniline derivatives with isopentylnitrite[13b] or nitrous acid[13c], whether the reaction is carried in organic solvent or aqueous solution.

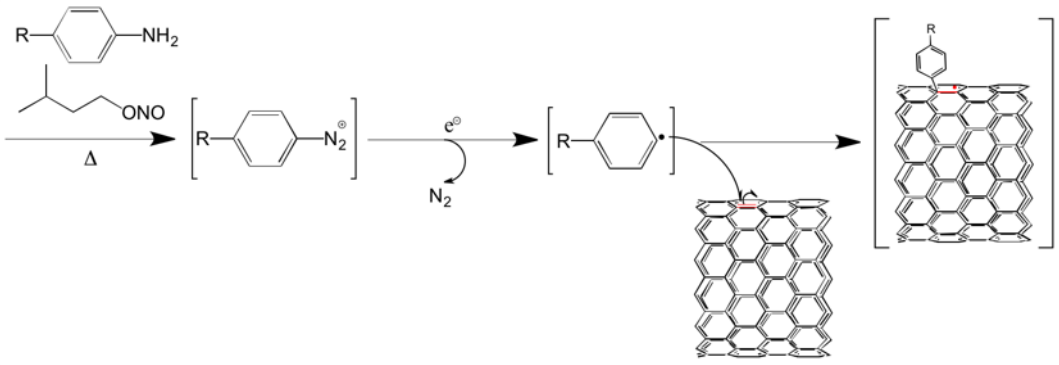

Figure 1-11: Tour reaction mechanism.

Although the actual mechanism is still under investigation, it was proposed that the first step of the reaction involves the reductive dissociation of the diazonium salt, with loss of N_2, and formation of an aryl radical.[18] This in turn may react with carbon–carbon double bonds along the nanotube walls according to the so-called Meerwein arylation.[19]

Moreover, recent investigations have been pointing out that the chemistry involved may not be as straightforward as initially suggested. Indeed, the removal of physisorbed byproducts may be difficult[20], and the high reactivity of the species involved in the process may cause degradation of the functional groups.[13d] In this context, the functionalization of MWCNTs with aryl diazonium derivatives generated *in situ* by treatment of 4-methoxyaniline (**1**) with isopentylnitrite (**2**) was studied.[21]

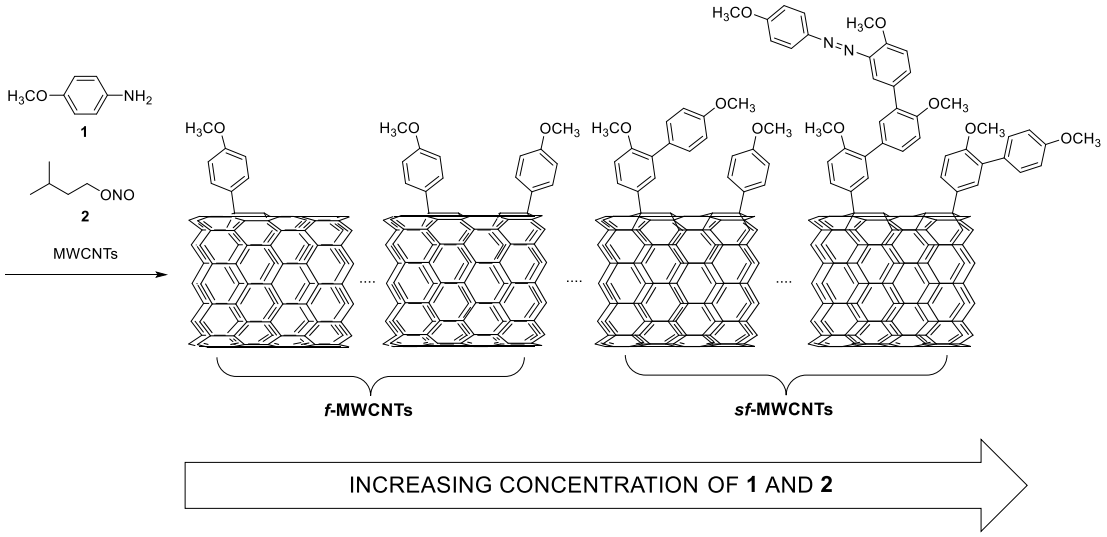

Figure 1-12: The addition of the diazonium salt generated *in situ* from 4-methoxyaniline (1) and isopentylnitrite (2) to MWCNTs affords a range of different products, including functionalized (*f*-MWCNTs) and superfunctionalized (*sf*-MWCNTs) nanotubes, depending on the amount of reactants 1 and 2 relative to that of MWCNTs. [22].

Following a thorough purification, and characterization protocol (UV/Vis/NIR, TGA, ATR-IR, cyclic voltammetry and AFM), the formation was observed of both functionalized CNTs (*f*-MWCNTs), where the amount of functional groups anchored to the carbon surface is less than a monolayer, and superfunctionalized CNTs (*sf*-MWCNTs), where the aromatic groups already grafted to the CNT have been further functionalized. The molar ratio between reactants, and nanotube carbon atoms resulted to be the key parameter, granting access to either *f*-MWCNTs (lower ratios) or *sf*-MWCNTs (higher ratios) starting from the same pristine material.

1.2.2 **Non-covalent functionalization**

An alternative strategy to tailor the interfacial interactions of CNSs with matrices, yet preserving the integrity of their electronic properties, is the non-covalent functionalization based on van der Walls forces or π–π stacking interactions. Surface coating or wrapping with low molecular weight amphiphilic surfactants[23] or with various types of polymers[24] ensures the effective solubilization of CNSs in water and organic solvents.

The strong interaction between the π-network of CNS surfaces, and a π-conjugated system like naphthalene[25] or pyrene[26] has allowed the attachment of many functional groups to CNSs. These nanohybrids could find use in many plasmonic applications related to photovoltaics, photocatalysis, photodetectors, and sensing, to cite a few.

This approach is currently under extension for the design of soft functional materials to be used in organic electronic applications. Such a supramolecular strategy is indeed a promising tool to control the morphology of bulk-heterojunction solar cells, and construct supramolecular light-harvesting antennae with well-defined disposition of the chromophores.

1.3 Composite materials

Composite materials are multi component materials composed of a polymeric matrix filled with a proper reinforcing phase that can be in the form of fibers or particulates. The use of composite materials is continuously growing in the present days for a large number of applications, ranging from transportations to constructions, and consumer products, as more manufacturers discover their benefits, and versatility. Composites are obtained by combining two or more materials that have different physico-chemical properties: by merging, they confer the composite its unique character while retaining their own peculiarities. In a composite, one or more phases (the fillers) are dispersed in a continuous phase (the matrix). Composite materials can be divided into polymeric, ceramic, and metallic, according to the nature of the matrix phase. Polymers offer many advantages over other materials, and they are widely used in various technical applications thanks to their ease of production, light-weight, and ductility, even if they offer lower mechanical strength compared to metals, and ceramics.

A nanocomposite is defined as a composite material with at least one of the filler components having a size in the nanometer scale (< 100 nm). In polymer nanocomposites (PNCs), the fillers' nano-scale dispersion within the polymer matrix leads to extremely large interfacial contacts between the components, thus resulting in superior properties with respect to bulk polymer phases.[27] PNCs show a number of interesting phenomena related to the fact that a consistent fraction of polymer is close to a solid interface. The peculiar role of interfaces in modifying polymer properties within their proximity is recognized since the discovery of semicrystalline polymers, and the proliferation of PNCs has largely widen this awareness. Advanced technologies can be developed for light-weight applications, aerospace structural components, actuators, adaptive, and smart materials using multifunctional PNCs. Clays are, for example, a group of inorganic nano-fillers which have been widely used for the preparation of PNCs. Clay-PNCs[28] are appealing materials for a wide range of

applications in engineering, and manufacturing thanks to their durability, and strength, coupled to low density, but their potential has been so far only partially realized. CNSs are particularly interesting for this field thanks to their high elastic modulus, and electrical conductivity; they could not only bring a mechanical reinforcement, but also allow electrical conductivity on otherwise insulating materials.

1.3.1 **CNSs-based composite materials**

Due to their unique structures, composed of sp^2 carbon networks, characterized by high aspect ratios, electrical, and thermal conductivities, high Young's modulus, and tensile strength, CNSs are considered ideal filler phases to improve electrical, thermal, and mechanical properties of polymers.[7, 29] The first example of CNS-PNCs was obtained through mechanical mixing of purified MWCNTs and an epoxy resin.[30] Since then, attention has been addressed mainly to composite materials with uniform, and high nanostructure loading, focusing on their mechanical properties.

Nevertheless, the combination of CNSs with polymers offers an attractive route not only to reinforce polymer phases, but also to introduce new properties deriving from morphological modifications or interactions between the two components.

Industrially produced composite materials usually involve a simple blending of the two components, where the filler is frozen inside the polymer network. The aim of this work is to explore the effects of a better dispersion of the filler, and a stronger interaction between the polymer, and the CNSs by covalently bonding the two components. A better interface could lead to better load transfer under stress, hence better mechanical properties.

1.3.2 **Electrospinning**

Electrospinning is a polymer transformation technique that allows to obtain huge amount of nanofibers starting from the melt or dissolved polymer by applying a strong electric potential during the spinning.

The electrospinner consists in an extruder (A), that controls the polymer flow through a metallic needle (B), and a generator that can apply an electric potential in the order tens of kV between the needle, and the collecting plate (E). During the extrusion, on the tip of the needle, the polymeric material form a Taylor cone from which starts a continuous nanometric jet of polymer (D).

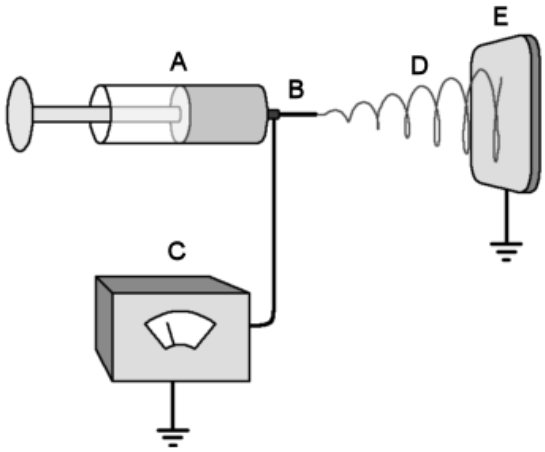

Figure 1-13: Schematic representation of an electrospinner.

This technique is of great scientific interest because it is almost the only method to obtain big quantity of polymeric fibers with a sub-micrometer diameter. The first studies on electrospinning date back to the first half of the last century, when many physicists begin to analyze the dynamic of fluids under strong electric fields. For more than 50 years, however, these studies have not had the possibility to deepen. Only in the second half of the last century it has been possible to study all the basic principle of electrospinning, and the properties of the electrospun fibers, thanks to the develop of microscopies (SEM, TEM, AFM), diffractions (WAXD, SAXS), and many other characterizations techniques. It has also been possible to study its operation with a large number of polymer not available in the past. From these studies, it has emerged that almost all thermoplastic polymers that are soluble in a volatile solvent can been spun through electrospinning. This is not true for melt polymers, which can be really hard to spin due to their higher viscosity.

Electrospun nanofibers are characterized by an extremely high surface/volume ratio, and this makes them of considerable interest in the science of composite materials, in which a filler interaction with the external environment is important.

Researchers used elettrospinning for the preparation of polymeric nanofibers functionalized on their surface with silver nanoparticles for catalytic purpose.[31] In the last years, many researchers have demonstrated that electrospinning can enhance the biocompatibility, and bioactivity of the polymer used with respect to the bulk material.[32] Nanofibers obtained through electrospinning of Polylactic acid (PLA) are really gaining lots of interest in many researches in the field of biomedical engineering, drug delivery, and biotechnologies in general.[33] It is clear that the high surface/volume ratio, and ease of preparation are the main strengths of the electrospinning in this kind of applications.

1.3.3 **Polylactic acid**

Polylactic acid, or polylactide is an aliphatic thermoplastic polyester with molecular formula $(C_3H_4O_2)_n$.

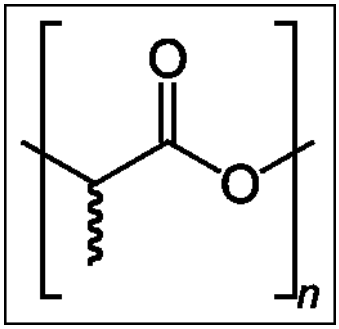

Figure 1-14: Molecular structure of PLA.

It is clear from its structure that it is an homopolymer that can exist in two different configurations, namely PLLA, and PDLA, due to the chiral nature of lactic acid.

Its synthesis can be performed by step-growth polycondensation of lactic acid, or by ring opening polymerization (ROP) of the lactide. (see figure)

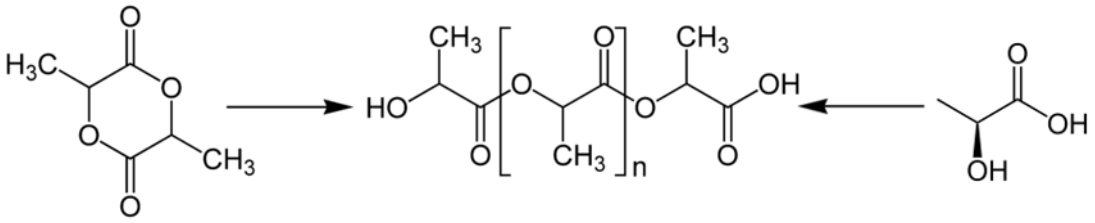

Figure 1-15: Reaction scheme for the synthesis of PLA.

Lactic acid needed for the polymerization can be obtained through fermentation of renewable biomass, mainly accomplished by the bacteria belonging to the genus *Lactobacillus.* Of course, from this production method it can be obtain only the L-lactic acid. So, for the synthesis of PDLA it is necessary to chemically synthetize the D-lactic acid. From an industrial point of view, the synthesis of PLA (in any configurations) is however preferable performing the ring opening polymerization that allows to obtain higher molecular weight. Moreover, ROP can be catalyzed to obtain a polymer with a much higher quality.[34] PLA can crystalize with 3 different conformation, α, β or γ, depending on the conditions. The α form is the most common one; it is obtained by melting or solution crystallization in normal conditions. The crystalline structure consists in two antiparallel chain in a 10_3 levorotary helix conformation forming an orthorhombic unit cell.[35]

Usually PLA can be electrospun from solutions from 5% to 20% in polar solvent like acetone or chloroform, applying an electric potential of 15-30 kV, and a needle/plate

distance of 10-20 cm. For example, S. Wang et al. electrospun PLA from a chloroform/acetone (2:1) solution at 5% w/w, with an electric potential of 25 kV, a needle/plate distance of 15 cm, and an extrusion flow of 0.1 mL/h.[36]

1.3.4 **Application fields**

Advanced polymer-based nanocomposites are appealing materials for many different biomedical applications, ranging from scaffolds for tissue engineering[37] to releasing matrices for drug delivery,[38] biosensors[39], or artificial muscles, tendons, and other bioactuators.[40] Being their uses addressed towards living organisms or *in vivo* testing, naturally occurring polymers are preferred over traditional petro-polymers as nanocomposite matrices. These polymers can either derive directly from natural sources, like polysaccharides such as starch, alginate, chitin, chitosan, and cellulose, or be synthesized from naturally occurring monomers, like poly(lactide), or be the products of microbial fermentation, like poly(hydroxybutyrate)[41]. CNSs are considered ideal polymer nano-fillers also for these materials, allowing the preparation of functional nanocomposites with improved mechanical, electrical, and thermal properties, but also able to perform more complex functions, the choice of which is related to the final goal for which the material is envisaged. In this case again, chemical functionalization of CNSs can be significantly helpful in achieving better dispersion within polymeric matrices, but also in introducing tailored moieties aimed to gaining the specific functions.[42] Carbon nanostructures, including carbon nanotubes, and graphene-based materials, are largely employed fillers for polymer phases, being able to confer novel properties to the latters. [43]

CNSs are promising scaffolds for neuronal, bone, and cardiac tissue engineering.[44] Nevertheless, CNSs suffer from biocompatibility issues depending on the type, and doses employed, and on the tested cell populations.[45] For this reason, incorporation into a polymeric, bio-compatible matrix emerges as a key requirement to further extend these potentials. Furthermore, the dispersion of CNSs into such a matrix can help generating a freestanding, and implantable device.[46]

1.4 Characterizations

In order to describe the properties of the CNS before and after the functionalization, it is mandatory to have a protocol for the characterization of the material. Many of the conventional characterization techniques used for molecular species have limited applicability to CNSs, due to the size of the particles, and the number of atoms they are comprised of. Optical spectroscopies have to face problems related to the low solubility of CNSs in common solvents, and their strong absorption, and scattering properties. NMR measurements can hardly give any information, given the number of atoms, and the heterogeneous nature of the particles. Those are just a few of the problems that needs to be faced when characterizing CNSs.

For these reasons, it is necessary a synergic work between different techniques to obtain a univocal information about the properties of a CNS. The techniques used in the characterization workflow are described below.

1.4.1 **Thermal characterizations**

Thermogravimetric analysis (TGA) are a class of characterization extremely important in many field like material science, and nanotechnology. In a TGA, the sample is heated slowly while measuring the weight loss resulting from combustion, decomposition or evaporation process.

This technique is very useful for the characterization of CNSs because they present a really high thermal stability strictly influenced by their structure or by any chemical modification performed. In case of functionalized CNSs, it is possible to analyze the difference in decomposition temperature of the CNSs itself (usually at a temperature higher than 500 °C), and the decomposition of the functionalized moieties (usually between 100 °C and 400 °C). In this way, it is possible to estimate the degree of functionalization of the CNSs, expressed as the ratio between the moles of the functional groups, and the moles of carbon in the CNSs.[11a]

If $W_{CNT,500}$ is the residual weight of CNSs at 500 °C, and MW_C is the molecular weight of carbon, the moles of carbon atoms in the CNSs (mol_C) results:

$$mol_C = \frac{W_{CNT,500}}{MW_C}$$

The moles of the functional groups (mol_{FG}) can be obtained from the weight loss at 500 °C divided by the molecular weight of the functional group (MW_{FG}):

$$mol_{FG} = \frac{(W_{100} - W_{CNT,500})}{MW_{FG}}$$

The degree of functionalization (FD) can be defined as the ratio between the moles of the functional group (mol_{FG}), and the moles of carbon atom of the CNSs structure (mol_C)

$$FD = \frac{mol_{FG}}{mol_C}$$

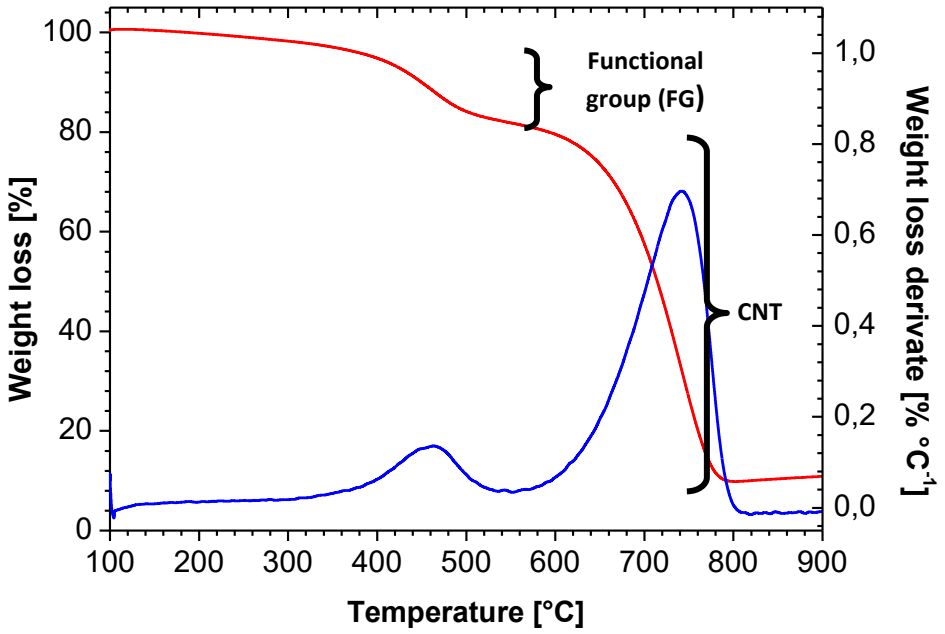

Figure 1-16: TGA of a sample of functionalized MWCNTs.

TGA is extremely useful also for the characterization of composite materials, in which the matrix, and the filler have a remarkable difference in their degradation temperature.

1.4.2 Optical characterizations

Uv-Vis-NIR spectroscopy

Uv-Vis-NIR absorption spectroscopy is a very important technique for the characterization of CNSs, both from a qualitative, and a quantitative point of view.[47]

The absorption spectrum of CNSs is due to the electronic transitions in the range 400-2500 nm, and it is characterized by a plasmon plateau relative to the absorption of the big delocalized sp^2 structure.

For SWCNTs, it is possible to see specific absorption bands due to the confinement of the density state, resulting in the so-called Van Hove singularities in the band structure. These transitions are partially superimposed on the aforementioned plasmonic contribution, and are specific of a single family of CNT.

Uv-Vis-NIR absorption spectroscopy is very versatile, and, in combination with Raman spectroscopy, can provide information on the chiral distribution of a sample of SWCNTs. In condition of good dispersion in solution, it is also possible to correlate the absorbance of the sample to its concentration through the Lambert-Beer law:[47b]

$$Abs = c \times l \times \varepsilon$$

Where *Abs* is the absorbance of the sample, ε (mL mg^{-1} cm^{-1} for CNSs) is the molar extinction coefficient, *c* is the concentration (mg mL^{-1}), and *l* is the pathlength.

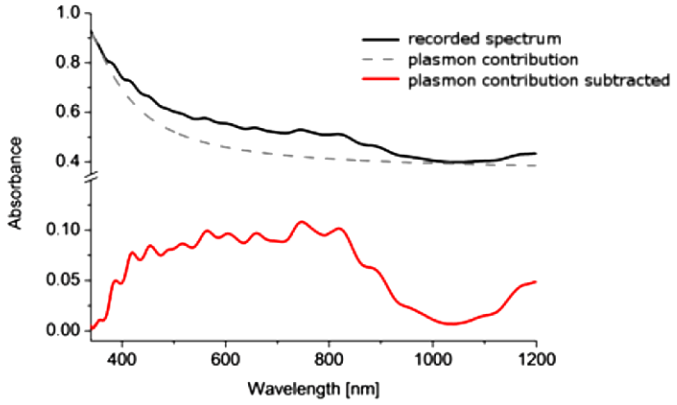

Figure 1-17: Uv-Vis-NIR absorption spectra of a sample of SWCNTs (black curve), the plasmonico contribution to the absorption (dashed curve) and the difference between them (red curve).

The analysis of the SWCNTs diameter population distribution allows correlating the transitions with higher energy to the Van Hove bands of metallic CNTs (M11 in figure), and the transitions with a lower energy to the bands of the semiconducting ones (S11, S22 in figure).

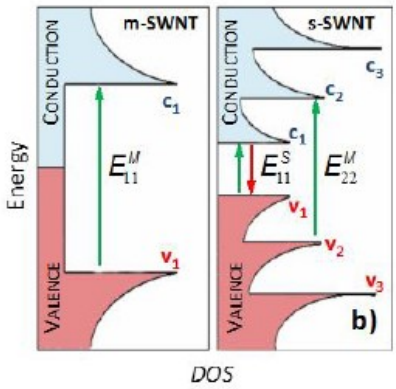

Figure 1-18: Density state representation and electronic transitions for metallic and semiconducting SWCNTs.[48]

Raman spectroscopy

Raman spectroscopy is a fundamental tool for the characterization of CNSs. Into the spectra of all the different carbon nanostructures, the three following important bands are evident:

- *G band (graphite)*: centered in the interval between 1550, and 1605 cm^{-1}, this band corresponds to the vibrations of sp^2 carbon atom in the CNSs structure. For samples of purified semiconducting CNTs this band can be split in two different bands in a range of 6-15 cm^{-1}: G- (at lower energies) associated to the vibrations along the circumference of the tube, and G+ (at higher energies) associated to the vibrations oriented longitudinally to the main axes of the CNT.
- *D band (diamond)*: centered in the interval between 1250 and 1450 cm^{-1}, this band is due to the defects in the sp^2 lattice. In particular, it comes from the vibrations associated to sp^3 carbon atoms. Due to its nature, this band increases in intensity as the CNSs become more covalently functionalized. From this fact, and from the definition of the G band, comes that the ratio between these two bands gives a quantitative analysis of the density of defects present in the sample. This value, namely D/G ratio, is correlated with the degree of functionalization of the CNS.
- *G' band*: between 2500 and 2900 cm^{-1}, this spectral band is due to all the non-longitudinal vibrations mode.

- *RBM (radial breathing mode):* detectable only in for SWCNTs, it represent the radial vibrations in the region at lower frequency, usually below 400 cm^{-1}. The frequency of the bands in this spectral region is inversely proportional to the diameter of the SWCNTs as follow:[48-49]

$$\omega_{RBM} = C/d_t$$

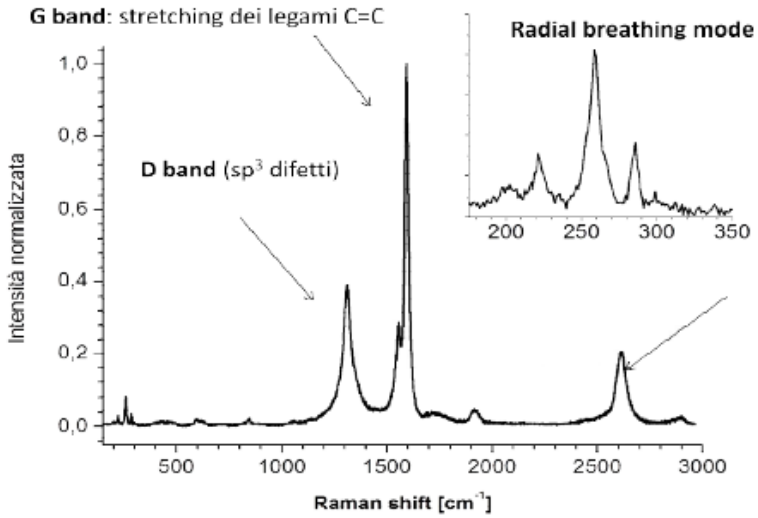

Figure 1-19: Example of a Raman spectrum of a sample of SWCNTs.

1.5 Aim of the thesis work

Moving from the experience of the research group where I am carrying out my PhD studies, and from results obtained during my previous master thesis work, the objectives of this project are focused on the chemical functionalization of carbon nanostructures, and their compatibilization into polymer matrices to generate functional polymer-based nanocomposites.

At first stage, the main aim of the research is the optimization of the functionalization with 4-methoxyaniline of three different CNSs: multiwalled carbon nanotubes (MWCNTs), carbon nanohorns (CNHs), and reduced graphene oxide (RGO) as "graphene like" material. The aim of the functionalization is to enhance the solubility of the CNSs in organic solvents like DMF or chloroform. Indeed, the optimization of the reaction parameters is performed in order to maximize the gain in solubility of the product. After that, we want to prepare and characterize polymer-based nanocomposite (PNC) materials based on the 4-methoxyphenyl functionalized carbon nanostructures (namely CNS-PhOMe) dispersed in a poly(L-lactic acid) (PLLA) matrix

(namely CNS-PhOMe@PLLA). These materials are obtained both in the form of freestanding films, and in the form of nanofibrous substrates (the latter obtained by electrospinning, and defined as eCNS-PhOMe@PLLA). With these materials, we want to study the effect of the incorporation in the PLLA matrix of different CNSs, and at different loadings, on the mechanical, thermal, electrical and biological properties. The main aspect that we want to analyze is the difference in properties of the final composite material due to the particular morphology, and shape of the CNSs used. Thanks to these studies, it will be possible to establish the best fields of application suitable for the different CNSs, based on their particular effects on the electrical mechanical and thermal properties when used as fillers.

Therefore, we want to perform in vitro tests using human neuroblastoma cells (SH-SY5Y), and human peripheral blood stem cell (hCMCs), in collaboration with the research group of Prof. F. Filippini from the department of Biology. These last cells have the advantage of not being embryonal, and therefore not subjected to ethical restrictions. With these tests, we want to study the biocompatibility, and the neuritogenic properties of our new composite materials. In particular, we want to analyze if the well known biological properties of CNTs are preserved in the composite materials, and moreover, if these properties can be combined with the biocompatibility of the full-biocompatible, FDA approved, PLLA matrix.

After that, we want to study *in vivo* the possibility to integrate our PNCs scaffolds containing CNSs in implants for peripheral nerve surgery on living organisms, in collaboration with the group of Prof. Bassetto from the Clinic of plastic and reconstructive surgery at the department of neuroscience,

After this first part, we want to analyze the use of the Tour reaction for the introduction of different, and more useful moieties, like carboxylic acid, and styrene groups. Carboxylic groups are used to perform an amidation reaction onto the CNSs in order to obtain a more complex functionalization. In particular, our aim is to study the conjugation of bio-mimetics peptides onto CNSs in order to further enhance their biocompatibility, and bioactivity. On the other hand, styrene functionalizations are used to study a “grafting from” polymerization of polystyrene on the CNSs. In this way, thanks to the covalent link between the nanofiller and the polymer matrix, it should be possible to enhance the mechanical interaction between them, determining a modification of the properties of the final material.

Finally, we want to study the reaction scheme of the Tour functionalization analyzing the importance of triazenes species in the generation of the aryl radicals. In particular, we want to study the effects of different acidic, and basic conditions onto the overall reaction pathway and the consequent reaction efficiency.

2 Results and discussions

This chapter is composed of three sections, corresponding to three main tasks of my research activity.

The first section reports on the optimization of the functionalization of CNSs aimed to maximize their solubility in organic solvents, and then describes their use as filler inside a PLLA matrix with the purpose of obtaining good quality biocompatible composite materials.

In the second section, it is presented the use of the Tour reaction to introduce reactive functional groups onto the outer surface of CNSs that can be useful for a second derivatization of the nanostructures.

Finally, it is presented a study on the reaction pathway of the Tour functionalization that analyzes the importance of triazenes species in the process providing a hypothesis of reaction scheme characterized by two different pathways.

2.1 PLA-Based composite materials

This section is focused on the preparation of PLLA based composite materials containing well-dispersed functionalized CNSs. The functionalization with 4-methoxyaniline through Tour reaction provides an enhancement in the solubility of the CNSs, decreasing their strong interaction, and thus the consequent tendency to aggregation. The so-obtained functionalized CNSs can be used as filler inside a polymeric matrix, easily obtaining an extremely good dispersion. CNSs have unique, and interesting electrical, thermal, mechanical, and biological properties, therefore the possibility to obtain good quality composite materials based on them can provide useful compound for many application fields. Indeed, understanding the different effects of the different CNSs when used as filler is extremely important.

2.1.1 **Functionalization of CNSs**

The functionalization of CNSs consists in the addition of a functional group on the outer layer of the nanostructure, with the main aim of limiting the wan der Waals interactions, and so prevent their aggregation in solution. The best solvents for this reaction are of course those that can better disperd the pristine CNSs: in particular, NCP (N-cyclohexyl-2-pyrrolidone), NMP(N-methyl-2-pyrrolidinone), and DMF are in this order the best. NCP, that is the solvent that will be used in all the functionalization performed in this thesis, has however a big drawback: it has an extremely high boiling point that can be a problem in the purification steps, and in a scale up process. Though,

in the lab scale, and with an appropriate reaction protocol,this solvent can provide the best results. .

The functionalization reaction that will be used in this work is the so-called Tour reaction. It consists in the addition of a diazonium salt to the double bonds present in the sp^2 lattice of the CNSs. We decided to use this particular reaction because of its high efficiency in the functionalization of CNSs with a good variety of different functional groups. We also already reported that controlling the parameter of the reaction, in terms of temperature, time, and stoichiometry, it is possible to obtain a good control on the modification of the material. [22] the main parameter used here for the optimization of the functionalization of the 3 different CNSs is the relative amount of reactants with respect to the carbon nanostructure. All the other parameters will be fixed respectively to 80° C, and 15 minutes, as it was found during the optimization of the reaction on MWCNTs.

The three types of CNSs considered in this work, namely MWCNTs, CNHs, and RGO, were first subjected to the functionalization process to obtain the corresponding 4-methoxyphenyl derivatives. The functionalization was carried out in NCP in the presence of 4-methoxyaniline, and isoamyl nitrite. The reaction between these two species leads to the formation *in situ* of the reactive intermediate that actually functionalizes the CNS. (see experimental details in chapter 3)

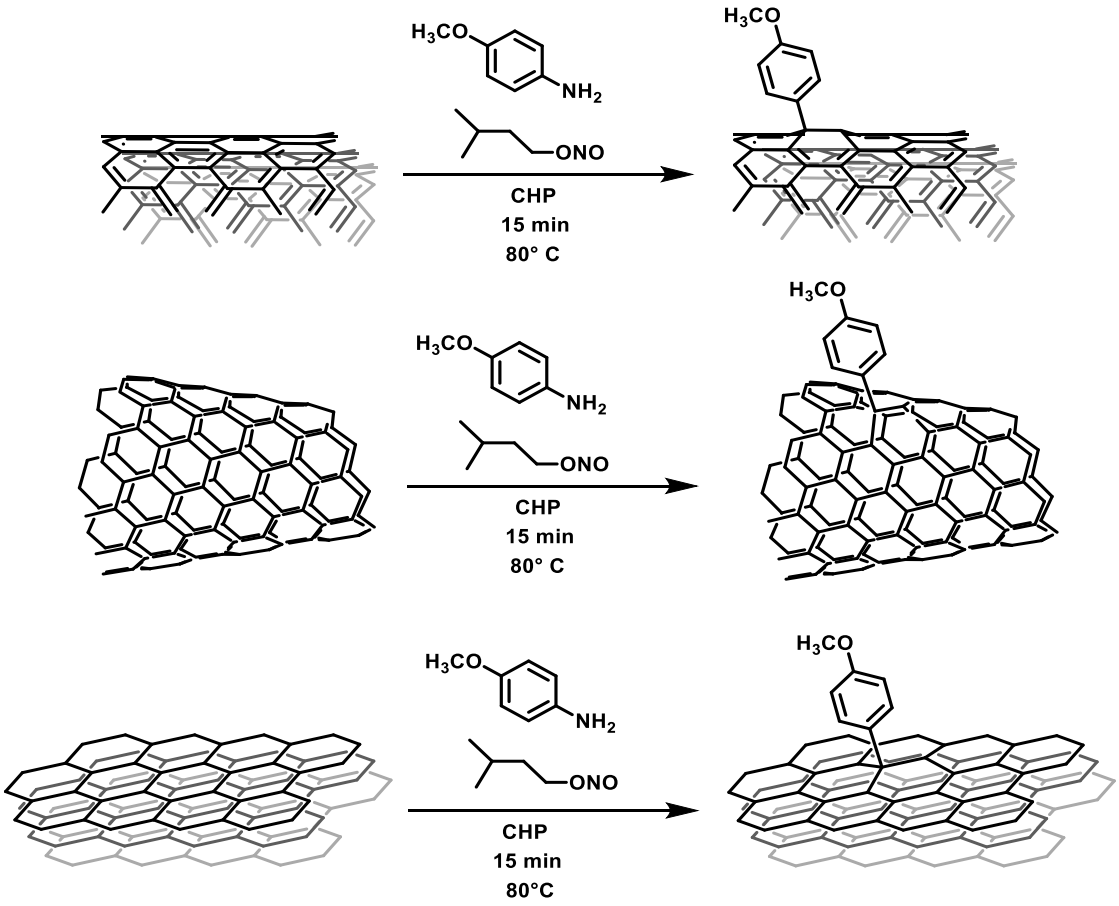

Figure 2-1: Covalent functionalization of MWCNTs (top), CNHs (center) and RGO (bottom) with 4-methoxyphenyl substituents via diazotization reactions.

Reactant amounts were screened in order to determine the best condition for the highest dispersion of the functionalized CNSs in chloroform (the solvent of choice for PLLA). As already reported by our research group, in order to express the relative amount of reactants, we defined the ratio between the moles of aniline, and the moles of carbon atoms of the CNS as the number of equivalents used for the reaction.[22, 50] It is important to note that in this calculation it is considered the whole amount of carbon atoms of the CNS, and not only those available for the reaction (e.g. the outer wall of MWCNTs). Therefore, the number of equivalents is a convenient way to express the reaction conditions for the functionalization, but it gives only qualitative information and not a real stoichiometry of the reaction. Moreover, since different CNSs are characterized by unique shape and morphology, the amount of carbon atoms available for the reaction is different for each of them. For this reason, the number of equivalents of aniline used for the functionalization of one particular CNS is not easily comparable with those used for other nanostructures. In our case, the maximum dispersion of MWCNTs, and RGO in chloroform was obtained when the reaction was carried out with 0.5 equivalents of 4-methoxyaniline, whereas for CNHs this happened when one equivalent of reactants was used. For every CNS, at least five different conditions were

tested (0.1, 0.25, 0.5, 1 and 5 equivalent). The need of different reaction conditions to gain the best solubility appears reasonable when considering the differences in morphology existing among the three CNSs, which lead to different reactivity, and tendency to aggregate. The resulting functionalized CNSs, namely MWCNT-PhOMe, CNH-PhOMe, and RGO-PhOMe, were characterized in terms of functionalization degree (FD),[22, 51] determined with a good precision through thermogravimetric analysis (TGA, the corresponding thermograms are reported in chapter 3). Particularly, FD values of 91, 47 and 44 were found for MWCNT-PhOMe, RGO-PhOMe, and CNH-PhOMe respectively, indicating that one 4-methoxyphenyl substituent is present every 91, 47 and 44 carbon atoms of the CNS. As before, it is important to note that also the FD calculation takes into account the whole amount of carbon atoms of the CNS, including those not exposed to the reaction. Indeed the highest number obtained for MWCNT-PhOMe is consistent when considering that only carbons of the outer walls are reactive. The FD provides useful information on the total amount of functionalization, but gives only qualitative information onto the real surface coverage of the functionalized CNS. Nevertheless, it can be used as a relative parameter to compare different derivatives of the same CNS. CNS-PhOMe were also characterized by RAMAN spectroscopy, Uv-Vis-NIR absorption spectroscopy, and DLS analysis. The characterizations agree with a good grade of functionalization able to enhance the solubility of the CNSs, and decrease the dimension of aggregates in solution while maintaining the main sp^2 structure of the material.

2.1.2 **Preparation of the composite materials**

The obtained CNS derivatives were effectively dispersed in chloroform, and then mixed with PLLA in different weight percentages (wt%) with respect to the polymer. In this way, films of MWCNT-PhOMe@PLLA, RGO-PhOMe@PLLA, and CNH-PhOMe@PLLA containing different concentrations of functionalized CNSs in PLLA were prepared. The resulting films were all free-standing, and characterized by a glossy texture.

CNS-PhOMe@PLLA blend solutions in $CHCl_3$ were prepared by adding a dispersion in chloroform of MWCNT-PhOMe or CNH-PhOMe or RGO-PhOMe obtained through sonication to a chloroform solution of PLLA (final concentration of PLLA: 6 wt%). The amount of CNS-PhOMe within the various blends was varied among 0.1, 0.25, 0.5, 1, and 5 wt% with respect to the polymer content. Films of the various composite materials were obtained through solvent evaporation into a petri dish at 50 °C, each of them having a diameter of about 6 cm except the film of RGO-PhOMe@PLLA 5 wt%, which had a diameter of 2.75 cm

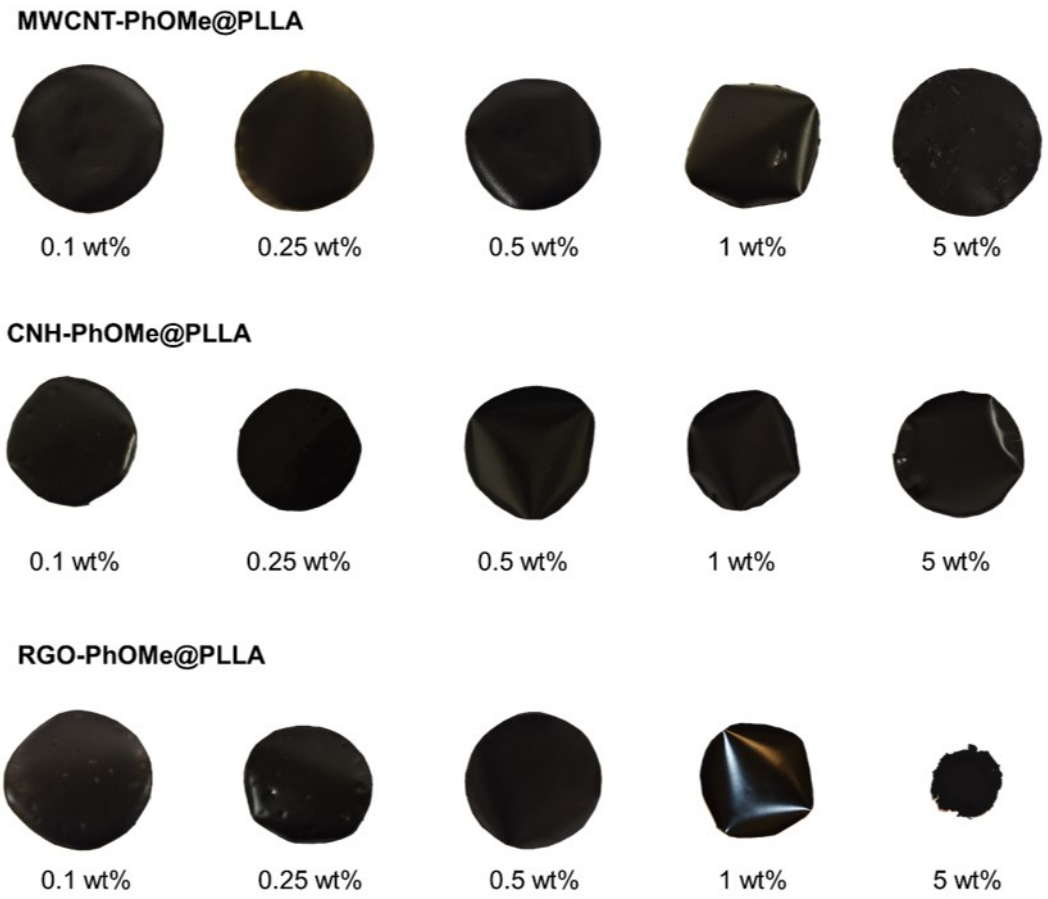

Figure 2-2: Photographic images of the functionalized-CNS@PLLA films considered in this work.

The thickness of each sample was measured at different points using a Mitutoyo Digimatic micrometer with a precision of 10^{-4} cm. Resulting thicknesses were found uniform among the films, and all included in the range between 300 and 350 μm (see chapter 3 for the exact values).

The 0.25% and 5 wt% functionalized-CNS@PLLA composites were also produced in the form of nanofibers by electrospinning. This process has been performed in the laboratories of Prof. C. Marega. Solutions of CNS-PhOMe@PLLA blends (0.25, 5 wt%) to be used for electrospinning were prepared following an analogous procedure to that described for the preparation of the films, but using a $CHCl_3$:DMF 9:1 (v/v) mixture as solvent. The small DMF portion in the solvent was introduced in order to increase the boiling point of the solution, and optimize conditions for electrospinning. Electrospinning was performed by means of a home-made apparatus with an applied voltage of 18 kV. Transmission electron microscopy (TEM) images were recorded with a Tecnai G2 microscope (FEI) operating at 100 kV. Samples were spun directly onto TEM copper grids for 60 seconds. AFM images were recorded on samples spun onto Graphene Supermarket silicon prime wafers (oxide thickness: 285 nm) for 60 seconds (see AFM details later in the text). In this work, the electrospun material analogous to CNS@PLLA will be named eCNS@PLLA. (this is also applied to bare PLLA fibers that will be named ePLLA).

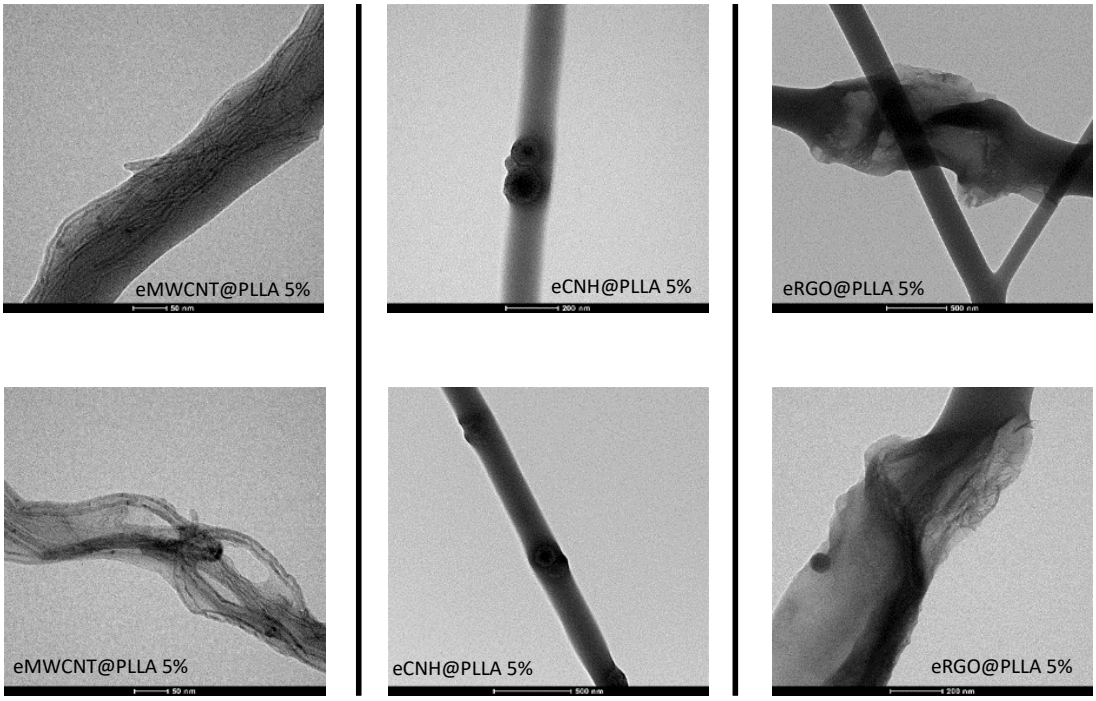

Figure 2-3: TEM images of the electrospun fibers of eCNS-PhOMe@PLLA 5%.

2.1.3 Characterizations of the composite materials

2.1.3.1 Optical analysis

The good dispersion of the functionalized CNSs within the polymer matrix was qualitatively evident after backlight inspection of the films with the lower concentrations of CNSs (0.1 wt%, see Figure 2-4a), in which the presence of macroscopic aggregates was not evident, while at higher concentrations transparency was lost, and backlight inspection was not feasible.

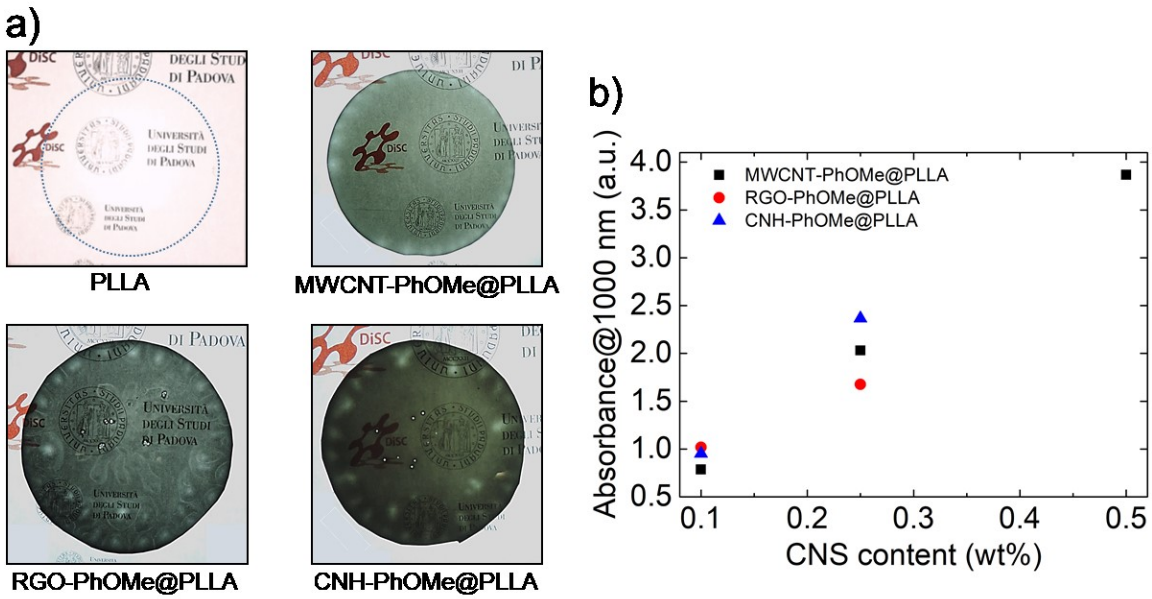

Figure 2-4: a) Backlight photos of sample films (~6 cm diameter) of 0.1 wt% functionalized-CNS@PLLA films and of a pure PLLA. b) Absorbance at 1000 nm of nanocomposite films as a function of filler wt% (high filler concentrations giving signal saturation are omitted)..

Absorbance values at 1000 nm were measured with a Varian Cary 5000 spectrophotometer equipped with a solid sample holder. For the case of MWCNT-PhOMe@PLLA films, an almost linear trend in the optical absorption at 1000 nm (a wavelength where only CNSs absorb) can be observed for the first three wt% examined, as reported in Fig. 2-4b, while at higher concentration saturation of the signal was achieved, not allowing to extend the extrapolation. For the other two functionalized-CNS@PLLA films only two points were extracted due to saturated absorption at lower wt% compared to MWCNT-PhOMe@PLLA films (see Fig. 2-4b).

2.1.3.2 Thermal analysis

DSC measurements were carried out with a DSC Q20 (TA Instruments) under nitrogen by heating the samples at 1 °C min^{-1} over a temperature range from 40 to 200 °C.

A further proof for the good dispersion of the functionalized CNSs within the PLLA phase was obtained by considering the crystallization temperature (T_c) extrapolated from

calorimetric data resulting from differential scanning calorimetry (DSC) analysis (see chapter 3 for the DSC traces of the three types of functionalized-CNS@PLLA composites at all the studied concentrations, and a complete resume of calorimetric data).

Actually, T_c values are significantly influenced by the presence of well-dispersed nanofillers, which can act as nucleating agents, allowing crystallization to happen at lower temperatures (PLLA usually crystallizes on heating in a cold crystallization process) [50]. This was particularly evident in MWCNT-PhOMe@PLLA composites [52], for which an almost linear decrease of T_c was observed when increasing the quantity of nanofillers up to the 1 wt% limit (see Fig. 2-5b. Fig. 2-5a reports the detail of DSC traces in the region where polymer crystallization takes place).

A decrease in T_c was also recorded for the RGO-PhOMe@PLLA composites as a function of CNS concentration, but it did not follow an almost linear regime as for MWCNTs. For CNH-PhOMe@PLLA composites, an apparent opposite behavior was observed, since at lower CNH-PhOMe concentrations (up to 1 wt%) an increase in T_c was detected, followed by a decrease at the highest concentration examined (5 wt%). This apparent mismatch in crystallization trends is significantly related to the particular size, and shape of each different nanofiller, which in turn influence dramatically the crystallization behavior of the resulting PLLA composites.

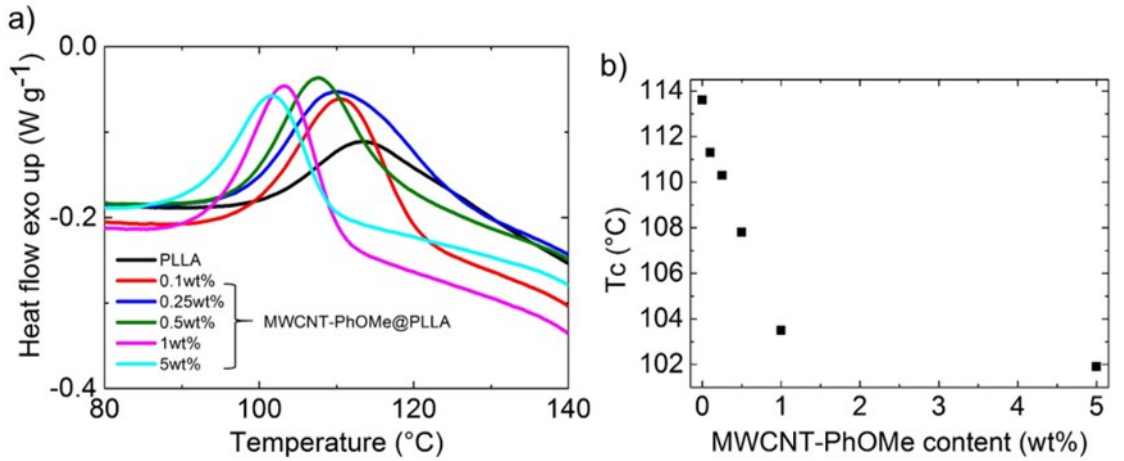

Figure 2-5: a) Zoom of DSC traces of MWCNT-PhOMe@PLLA composites with five different filler concentrations and of pure PLLA in the zone where polymer crystallization takes place. b) Variation of T_c (taken at maximum of the curves in a) as a function of MWCNT-PhOMe in the composite..

Also the thermal behavior of the electrospun samples have been evaluated by menas of DSC analysis as previously described for films. The first difference between these fibrous samples, and the corresponding films is the presence of a crystallization peak in the first heating ramp. This is due to the fact that, during the super-fast evaporation of the solvent in the electrospinning process, the PLLA matrix is not able to completely crystallize, as happens in the slow solvent evaporation process used in the preparation

of the films. This crystallization, that occurs inside the fibers, is visible at a lower temperature with respect to the one that normally happens in the bulk film samples; this is certainly due to the peculiar morphology of the electrospun fibers.

For the fibrous samples of CNH@PLLA, and RGO@PLLA, all the other parts of the thermograms are completely analogous to the corresponding one obtained for the bulk material. On the other hand, for the fibers of MWCNT@PLLA, it is possible to see a complete shift of the cold crystallization peak from the second heating ramp to the cooling ramp. This big enhancement of the melt crystallization due to the presence of MWCNTs in PLLA has already been reported, but in our sample it is visible only in the fibrous substrate probably because of the extremely good dispersion obtained in the electrospinning process. Furthermore, cycling the DSC with the same temperature program, this melt crystallization peak gradually moves at lower temperature, and disappears, leaving place to the normal cold crystallization process.

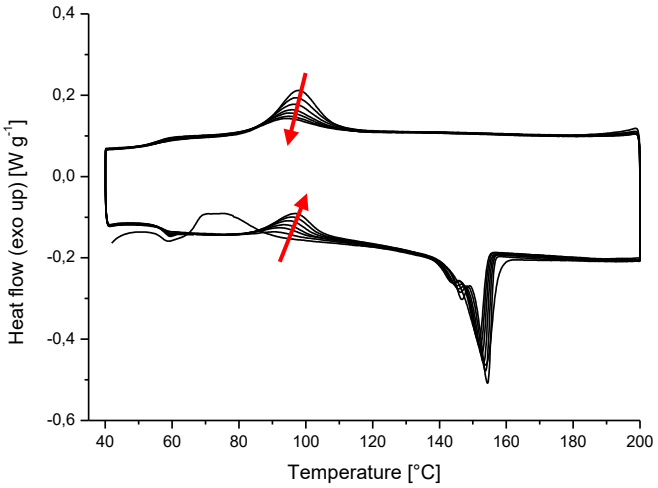

Figure 2-6: ***DSC of the fibers of MWCNT@PLLA at 5% of CNSs content.***

Since this effect is present only with the MWCNT@PLLA fibers, it is possible to suppose that it can be due to a partial retain after the melting process of the local alignment, and good dispersion of MWCNTs that characterize these fibers. This is probably due to fact that, the viscosity of the melt PLLA is high enough to prevent MWCNTs from completely reorienting randomly. Of course, cycling the melting process will give to the CNSs the opportunity to gradually reorganize in a complete isotropic way.

Performing the DSC with different temperature programs affect the rate at which the melt crystallization process tends to disappear. A comparison between the already described DSC, performed with a temperature program that reaches 200°C (Prog200),

and a second analysis that reaches as maximum temperature 180°C (Prog180) is shown in figure 2-7.

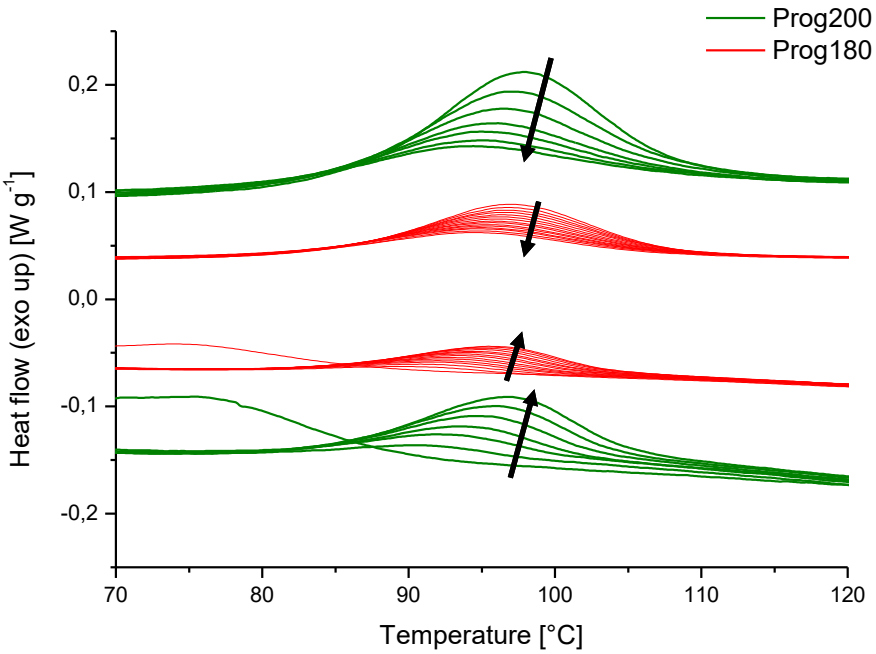

Figure 2-7: ***DSC of the MWCNT@PLLA fibers performed with different temperature program*****.**

As it is possible to see also from the melt crystallization enthalpies shown in figure, there is a strong dependence on the decreasing rate of the peak due to the temperature program used. In particular, the rate is lower if the temperature program reaches 180 °C instead of reaching 200 °C.

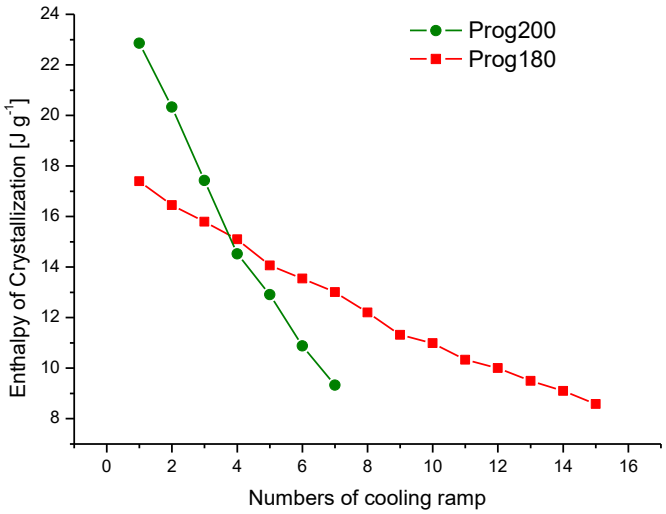

Figure 2-8: ***Enthalpy of crystallization as a function of the number of cooling ramp*****.**

Indeed, the program Prog180 maintains the sample in the melt state for a shorter time in each cycle, and, since reaching a lower temperature, the viscosity of the polymer is higher. Both these two aspects will surely hinder the diffusion of the MWCNTs inside the melt polymer, thus letting a slower loss of their retained local alignment, and anisotropic dispersion.

2.1.3.3 Mechanical analysis

Tensile mechanical properties of rectangular-shaped specimens were measured using an Instron model 3300 mechanical tester at room temperature. The strain rate was 10 mm min^{-1}. At least five measurements were performed for each sample.

The mechanical behavior of the functionalized-CNS@PLLA composites was investigated to determine the effect of the three nanofiller types at their different relative concentrations. The tensile strength was measured for all the examined materials on samples of the same size, and thickness, except for the 5 wt% RGO-PhOMe@PLLA composite, which was too brittle to undergo mechanical testing (too brittle even for handling, as it can be somehow inferred from its picture in Fig. 2-2). The variation in Young's modulus (Fig. 2-9a), and the variation in the percentage of film deformation at the fracture point (Fig. 2-9b) as a function of the nanofiller concentration are shown in figure.

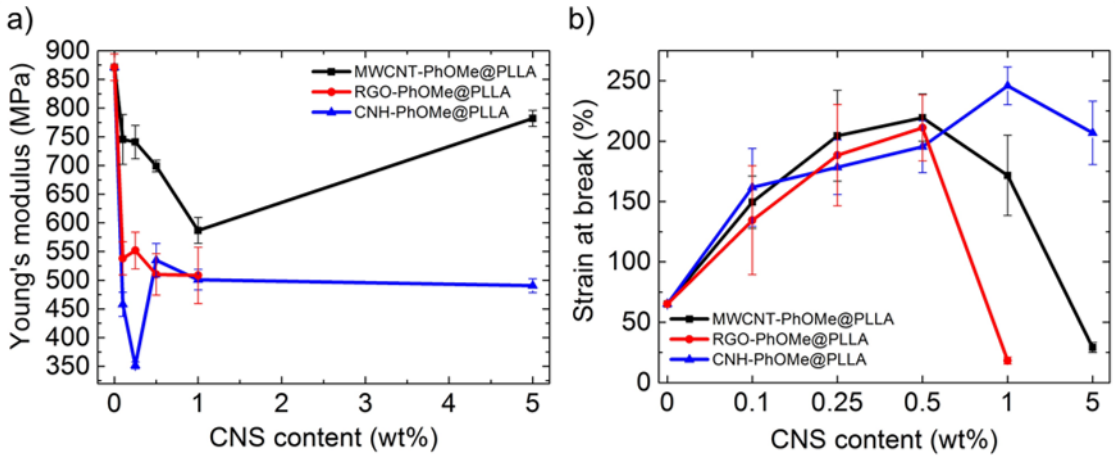

Figure 2-9: a) Young's modulus and b) strain at break for functionalized-CNS@PLLA composites as a function of nanofiller concentration.

The elastic modulus changes significantly when functionalized-CNSs are dispersed in PLLA: the pure polymer has a modulus of 871 MPa, whereas the inclusion of small amount of fillers (0.1 wt%) surprisingly drops it down to 745, 458, and 538 MPa for MWCNT-PhOMe, CNH-PhOMe, and RGO-PhOMe, respectively. In general, loading polymers with stiffer fillers (normally in the pristine form and thus lacking functionalization and good dispersion) is expected to increase Young's modulus [53]. In the present case, small amount of functionalized-CNSs in PLLA behaves more as plasticizers, rather than as reinforcing agents. This has been observed before for

poly(lactic-acid) phases plasticized with palm oil, and filled with small amount (up to 1wt%) of graphene nanoplatelets [54]. Since in our case no plasticizers have been added to PLLA, the effect must be likely driven by the presence of the 4-methoxyphenyl substituents covalently bound to the CNSs, that allow their homogeneous dispersion within the polymeric phase, and act as plasticizer. After the initial decrease at low CNSs concentrations, Young's modulus undergoes a slight increase only at higher concentrations of the fillers for the case of MWCNT-PhOMe (at 5wt%), and CNH-PhOMe (at 0.5 wt%), but remains still lower than that of bare PLLA. However, the trend in elongations at the fracture point for the three types of composites (Fig. 2-9b) is noteworthy: the increase in ductility with increasing filler content, up to 0.5 wt% for both MWCNT-PhOMe, and RGO-PhOMe, and up to 1 wt% for CNH-PhOMe, brings to final lengths at break 3-4 times longer than that of PLLA. Unfortunately, in the RGO, and MWCNTs based composites, this effect drops down for higher concentrations, eventually leading to materials which are more fragile than bare PLLA at 1 wt% for RGO-PhOMe, and 5 wt% for MWCNT-PhOMe. For the RGO-based composite at 5 wt% concentration, it was not even possible to measure any tensile strength because of the brittleness of the material, as already mentioned. Such a drop in ductility was not observed with CNH-PhOMe as a filler up to 5 wt%. While at lower concentrations CNS fillers are more homogeneously dispersed, it is reasonable to assume that at higher loadings they start to form larger aggregates, which affect the macroscopic ductility of the resulting composite. The overall mechanical response of the three types of composites is significantly influenced by the type of contained nanofiller, as it was observed for the calorimetric behavior. Different behaviors among CNSs can be due to their different size, and shape, and to their different tendency to aggregate, even if strongly mitigated by the covalent functionalization.

2.1.3.4 Electrical analysis

The surface resistance of the films was measured with two different instruments depending on resistance. For films with resistance lower than 10^6 Ω, a digital multimeter, Keithley 2000 provided with 4 probes positioned at a distance of 1 cm with respect to each other was used. Each film sample was measured in different points, and average values are given. For films with resistance higher than 10^6 Ω, a Keithley electrometers for Ultra-High Resistance *6517B*, coupled to a resistivity text fixture (Model 8009) for measuring surface resistivity was used. Measurements were performed alternating the polarity between 100 V and -100 V, and acquiring each point for 60 s. Average values over 10 repetitions are reported.

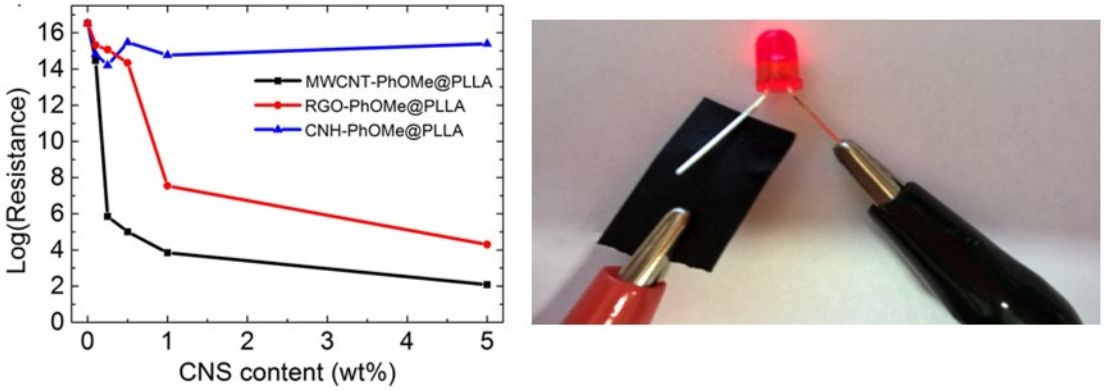

Figure 2-10: Electrical resistance in a logarithmic scale for functionalized-CNS@PLLA composites as a function of nanofiller concentration (left) and image of a led powered by a 9V battery and a speciment of MWCNT-PhOMe@PLLA at 5 wt% as resistance.

The bulk electrical properties of the functionalized-CNS@PLLA films were measured, showing again a behavior deeply influenced by the type of CNS used as nanofiller. In Fig. 2-10 the electrical resistance is shown as a function of the concentration of CNS in PLLA. A percolation threshold at very low filler content is observed for the composites based on MWCNTs, with a significant variation in resistance when moving from 0.1 to 0.25 wt%, this correspond to the formation of conductive networks. Indeed, it is known that CNTs are more effective than other fillers, such as carbon black, in conferring conductive properties to insulating polymers [55]. The fact that this happens at a low concentration of MWCNT-PhOMe deserves special attention,[56] it confirmes that the CNSs dispersion is optimized, and the occurrence of aggregates is negligible, which is possible thanks to the organic functionalization that drives the homogeneous distribution of nanotubes among PLLA chains. Also the extremely low value of resistance (120 Ω) obtained using only 5 wt% of MWCNTs is clearly a result of the efficient dispersion of the CNSs inside the polymer matrix. The recorded low resistance also evidences that our functionalization approach avoided excessive modification of the CNTs structure, which could result in the loss of the electronic properties of pristine nanotubes.[57] For the RGO-PhOMe@PLLA composites, a percolation threshold was found between 0.5, and 1 wt% nanofiller concentration. These fillers appeared to be less effective in increasing electrical conductivity in PLLA, with electrical resistance being 2 orders of magnitude higher than that reached with CNTs at the maximum concentration (5 wt%). On the other hand, with the CNH-PhOMe fillers, no percolation threshold was observed at the considered CNS concentrations, demonstrating again that the differences in nanomorphology among the components largely determine the macroscopic behavior.

2.1.3.5 AFM analysis

In order to electrically characterize the composites at the single filler size resolution, the materials were also investigated by means of AFM techniques. Only composites with the highest filler concentration (5 wt%) were considered. All the AFM analysis were performed in collaboration with Dr. Marco Salerno from the Materials Characterization Facility, at the Istituto Italiano di Tecnologia of Genova.

For AFM analysis of the film samples, small specimens (~5 × 5 mm) were cut and mounted each on a different optical microscope glass slide (1" × 3") by means of double-sided sticky tape. In case of topographic-only measurements, a standard tape was used, while for the CAFM measurements a conductive carbon tape (normally used for scanning electron microscopy as a drain layer for the injected electron beam current) was employed. The goal was to obtain a measurement of local transversal (i.e. out of plane) conductivity, perpendicularly to the film, and through that. For the fiber samples, few fibers were directly deposited by electrospinning on an insulating substrate of oxidized silicon wafer. The fibers were sparse enough to allow us to address, and image them independently. The fibers crossed the whole silicon substrate diameter, and touched the substrate edges on both opposite sides. There, a contact was provided all around the substrate edges by means of silver paste. The goal was to obtain a measurement of local longitudinal (i.e. in plane) conductivity, axial to the fibers, and provide a value of single fiber conductivity. Because the fibers were contacted on both opposite side ends, and in order to minimize the possible voltage drop along the fiber, the measurements were always carried out on fiber regions close to one edge of the silicon substrate, in the range of 100-300 µm distance from that. In both cases of CAFM samples (films on carbon pad or fibers with silver paint), the contact was taken away to the AFM head by means of adhesive copper tape stuck to the glass slide, and, later on, at a magnetic contact pad, to the head through a thin compliant wire.

The conductance was addressed by means of conductive AFM (CAFM) measurements. The film of bare PLLA did not show any measurable current, as expected, and the same occurred also for the CNH-PhOMe@PLLA composite film, even when probed at several different positions on its surface and with different contact forces. This confirms the data obtained through the macroscopic electrical characterization. The samples of MWCNT-PhOMe@PLLA, and RGO-PhOMe@PLLA exhibited instead measurable currents. Representative current images for the MWCNT-PhOMe@PLLA, and for the RGO-PhOMe@PLLA samples are presented in Fig. 2-11b and 2-11d, respectively (Fig. 2-11a, and 2-11c report the corresponding topography).

When considering for example the MWCNT-PhOMe@PLLA composite film (Fig. 2-11b), one can see that the current image is partly correlated with the surface topography, as

few high regions show no current (see filled arrows). However, these are real effects associated with the feature contents, and not topographical artifacts. The different compositional contents in the aforementioned tall features is also apparent in other surrounding regions with similar low current level (black areas), yet without outstanding heights (see void arrows). Obviously, independently on their height, areas of the films exist which are locally devoid of the CNS fillers imparting conductance to the composite. Conversely, the conducting regions emerging in Fig. 2-11b show a finer structure (down to the single pixel size i.e. ~40 nm) than in Fig. 2-11d. Indeed, in the former case, they are likely associated with smaller sizes of the carbon-based fillers (single MWCNTs or bundles of few of them), whereas in Fig. 2-11d the bright regions include several adjacent pixels up to ~2 μm linear size (see the arrowed zone) which are likely associated with sparse RGO flakes.

Fig. 2-11 further shows that, under the same conditions of vertical force (~18 nN), and bias (+1 V), the current levels observed on the MWCNT-PhOMe@PLLA film surface are higher than those for the RGO-PhOMe@PLLA one (see the vertical scale bar of the color palettes). Additionally, the total conductive area is higher for the MWCNT-PhOMe@PLLA composite, (17±5 % versus 7±4 % of the RGO containing composite film). When considering the means of the current levels on the different images of the samples, and averaging them, from the applied sample voltage (+1 V) resistance values of 2.6 ± 1.2 MΩ and 530 ± 230 MΩ are obtained for the MWCNT-PhOMe@PLLA, and the RGO-PhOMe@PLLA sample, respectively, which can be considered representative of the whole films. These values are in a similar ratio (about 200×) to that of film resistances measured macroscopically (see Fig. 2-10), yet are both shifted to approximately 4 orders of magnitude higher values. This likely depends on the very small contact area of the AFM tip, for the considered technique, at the limited vertical force used (see details in appendix). The agreement between electrical measurements made at the macro, and nanoscale is a proof of the good homogeneity achieved in dispersing the functionalized-CNS within the polymer matrix.

In Fig. 2-11e also single I-V curves typical of points in which conduction occurred (i.e. within bright regions in Fig.s 2-11a and b) have been plotted. One can see that the composite film with CNT fillers exhibits an almost ‘metallic’ behavior (straight Ohmic I-V profile), while the RGO film shows a passive region close to zero bias (sigmoidal profile), more similar to a semiconductor. An analogous difference in current values (about two orders of magnitude) between the two different samples is observed as described above, in favor of the MWCNT-PhOMe@PLLA film.

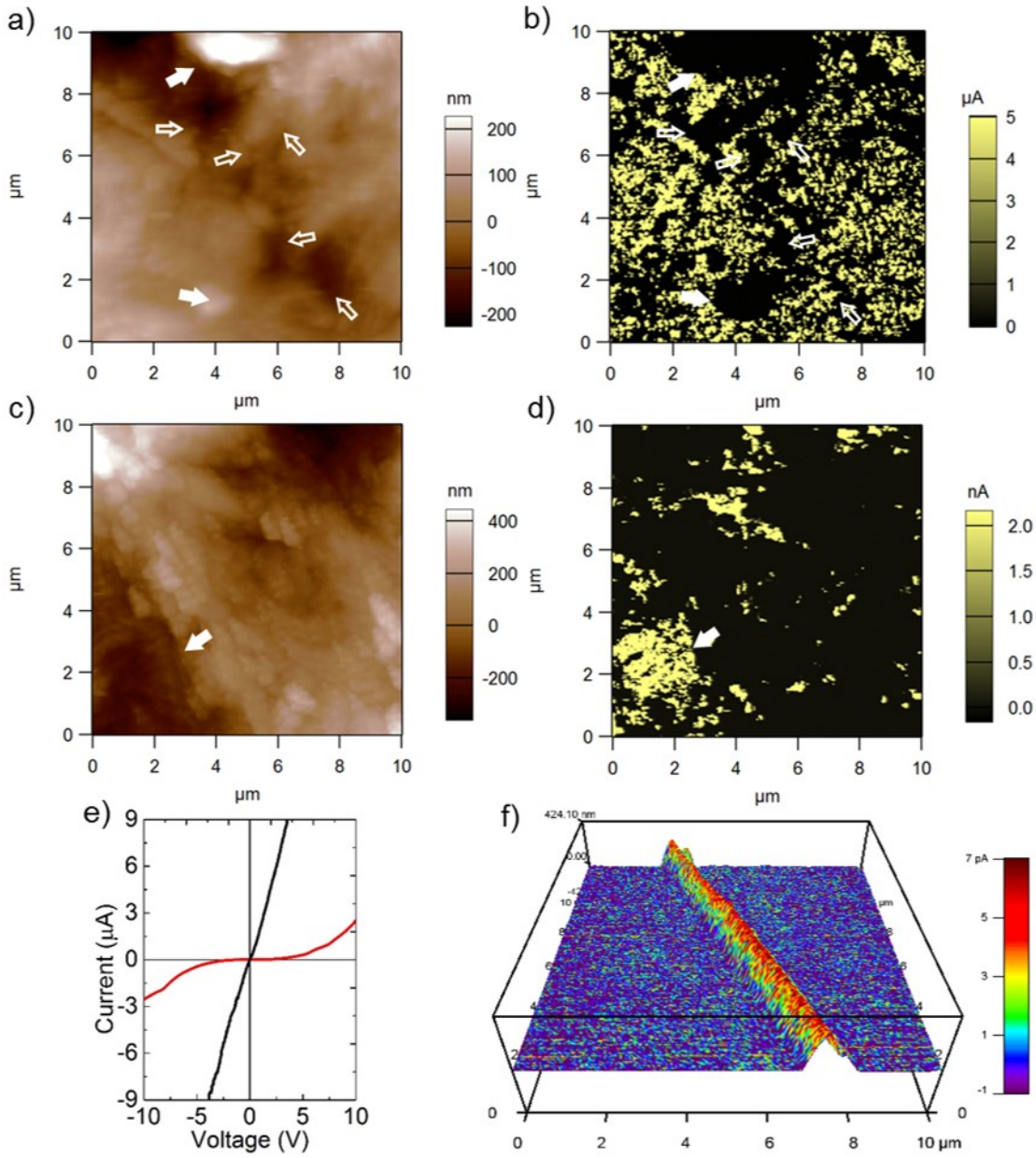

Figure 2-11: a-d) Representative CAFM images of films of a,b) MWCNT-PhOMe@PLLA and c,d) RGO-PhOMe@PLLA; a,c) topography, b,d) current images (at +1 V). d) I-V characteristic curves obtained at conductive points on the two samples of composite films. Black curve: MWCNT-PhOMe@PLLA film; red curve: RGO-PhOMe@PLLA film. f) 3D rendering of a current image taken on a MWCNT-PhOMe@PLLA electrospun nanofiber, with the current overlaid as a color onto the topographic 3D profile..

Finally, we investigated by means of CAFM the conductive properties of the functionalized-CNS@PLLA composites in the form of nanofibers, obtained with the electrospinning technique. This morphology was selected in order to study the electrical properties of the composites in nanoscale-confined model systems along a single direction. In Fig. 2-11f a CAFM image of a single MWCNT-PhOMe@PLLA nanofiber is shown. The current level has been rendered as the color, overlaid on the 3D profile of the height. For composite nanofibers, the CNT based sample was the only

one, which allowed current imaging, while in this form also the RGO-based composite did not show any conductivity. This can be justified by considering that, for the same filler concentration, percolation along a narrow conductor such as a nanofiber (200-600 nm diameter) is more difficult, and is detected in the present case only for monodimensional conductive fillers as CNTs. Also the geometry of the CAFM contact was significantly different in this case, in-plane along the fiber axis, and not through the fiber to the substrate. Actually, in the case of fibers, the substrate used was insulating, which allows us to obtain a typical value of fiber conductance. When the resistance is calculated, a value of ~7.1 GΩ is obtained, another factor 300× higher than what measured for the film of the same composite, and close to the lower detection limit level of the setup (mean current along fiber axis in Fig. 2-11f is 4.8 pA).

In order to support the electrical characterization of the different composites, we carried out AFM electrostatic measurements (scanning Kelvin probe microscopy –SKPM- and/or electrostatic force microscopy –EFM-) on the functionalized-CNS@PLLA composite with fibrous morphology. These AFM techniques are based on potential contrast due to accumulation of electrical charges, instead of their flow within a current, as for CAFM. Therefore, insulating fiber portions, , are expected to exhibit stronger contrast since not allowing the charge to be drained away. This was actually observed with fibers of bare PLLA (see appendix). The typical nature of the electrostatic contrast is apparent when noticing that the bright regions spread around the physical lateral extension of the fibers, which was not the case for the current in Fig. 2-11f. Similar results have been obtained also for the other samples of insulating (i.e. non-conductive) fibers (namely those containing RGO and CNH fillers). For the fibrous sample containing MWCNTs instead, in few cases, we observed fibers that looked from less bright (i.e. with only some degree of conduction) to completely dark (i.e. completely conductive). Unfortunately, it was not possible to acquire CAFM, and SKPM/EFM images simultaneously on the same fiber portion, because the two classes of techniques require different probe-holders. An interesting representative SKPM image of the MWCNT-PhOMe@PLLA fibers is shown in Fig. 2-12. In Fig. 2-12a a region is evident where several fibers cross each other. In the corresponding surface potential (SKPM) image of Fig. 2-12b, three different levels appear, namely an intermediate level background (associated with the substrate), a higher level (bright regions) spreading around the fibers (the typical bleeding effect of electrostatic charging), and a negative contrast (black) region localized only on some positions along the fibers, which can be associated with the functionalized MWCNT fillers. Such three regions are more clearly represented in Fig. 2-12c, where the same maps of topography (height), and surface potential and as in a) and b) have been rendered again in a 3D fashion, using a multicolor palette to segment the above-mentioned regions in different levels associated with red, green, and blue colors, respectively.

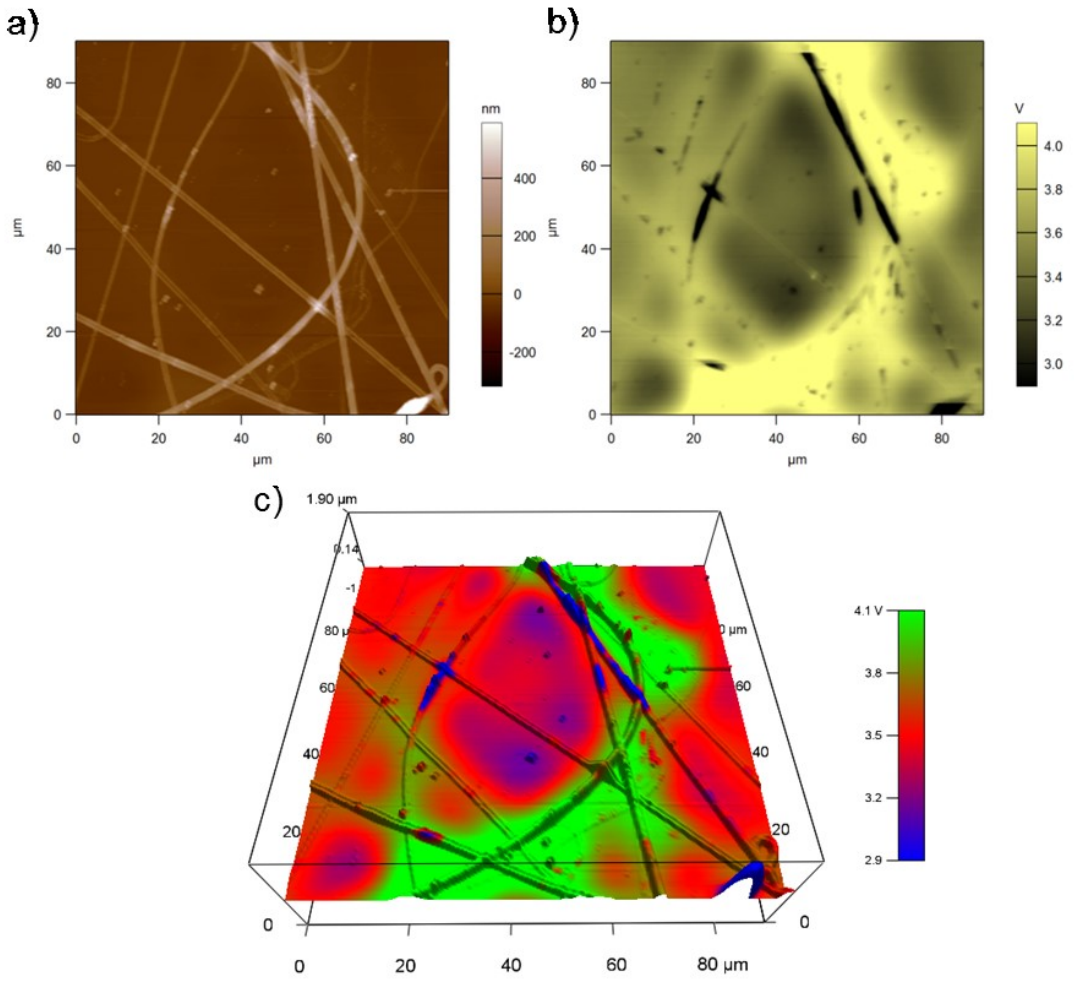

Figure 2-12: Large-area SKPM images of a sample of MWCNT-PhOMe@PLLA composite fibers, a) topography; b) surface potential; c) 3D topography of a) 'colored' with the surface potential in b).

As a final step of surface characterization of the functionalized-CNS@PLLA composites, the roughness of the film samples has been assessed by standard AFM (in non-contact mode). The 2D roughness amplitude parameter S_q was evaluated. The two composite materials based on CNH, and RGO fillers result in films with higher surface roughness (S_q~155 nm), whereas the composite based on MWCNTs is smoother, on the same level as the film of bare PLLA (S_q~70 nm). The differences between the two groups are statistically significant ($p<0.05$). Therefore, the well-dispersed MWCNT-PhOMe fillers provide a good uniformity in the overall electrical properties, resulting in a percolation network that endows the films with a good electrical conductivity, and, in addition, turns out to determine the least amount of surface roughening, compared to the bare polymer film.

2.1.4 **Biological tests**

In collaboration with the group of Prof. F. Filippini, in particular with Yuriko S. Hernandez Gomez from the Department of Biology, we tested the biological properties of our composite material. We studied the biocompatibility and bioactivity of the CNS-PhOMe@PLLA materials both in the form of freestanding film, and fibrous scaffold.

The functionalized-CNS@PLLA films were firstly tested for biocompatibility by employing them as scaffolds for the growth of SH-SY5Y cells. These cells are a well-known, and well-studied neuronal lineage often used as in vitro models of neuronal function, and differentiation. For both cell death, and cell proliferation assays, only two percentages per each type of CNS filler were selected, namely a lower one (0.25 wt%), and a higher one (5 wt%), assuming that the biocompatibility of all the intermediate concentrations will be preserved. In all assays, results from CNS scaffolds were compared to those obtained on bare PLLA, and on control wells coated with poly-l-lysine.

Cell death was evaluated 24 and 72 hours from seeding in order to combine cell viability to proliferation data, and, more importantly, to properly consider factors underlying cell viability.

Cells grown onto 0.25 or 5% functionalized-CNS@PLLA films showed viability values in the same range as control and as PLLA samples (figure 2-13a), moreover no meaningful effect was found on cell proliferation (figure 2-13b), thus demonstrating full biocompatibility is kept and the potential cytotoxicity of the three types of CNSs is prevented when employing them well functionalized, and dispersed within a biocompatible polymer matrix.

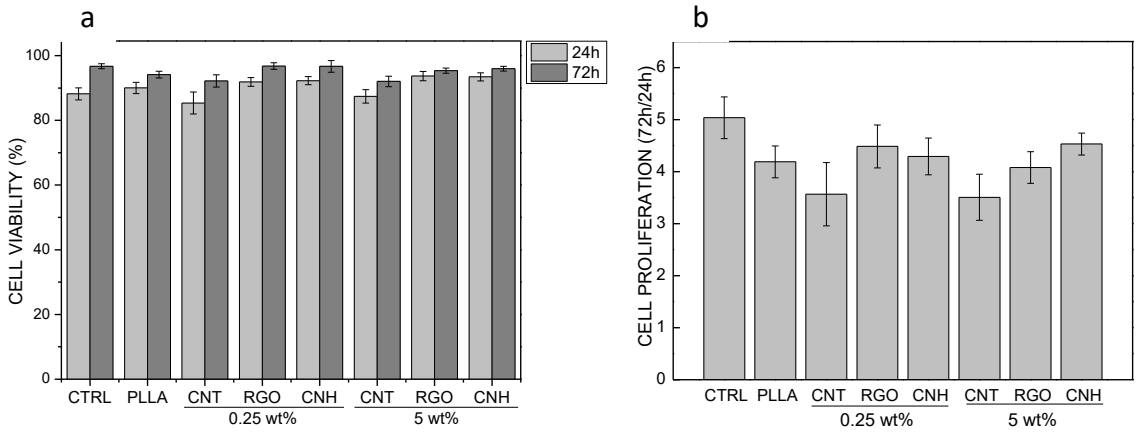

Figure 2-13: Percentage of viability (a) or proliferation (b) for SH-SY5Y cells grown onto control (poly-L-lysine coated) wells, pure PLLA film or functionalized-CNS@PLLA films. Data represents the mean ± SEM of four independent experiments performed in duplicate.

At the same time, this first study reveals that also cell adhesion on the substrate is not compromise by the presence of the nanostructures into the polymer matrix, and that is not influenced by the concentration and type of CNSs.

Finally, for what concerns cell differentiation, different morphological parameters have been evaluated: the number of neurites for cell, the total length of the neurites, the number of neurites longer than 100 µm, and the numbers of neurites longer than 150 µm. In figure 2-14 are reported the results obtained for MWCNT@PLLA films (the analogous results obtained for CNH@PLLA and RGO@PLLA films are reported in appendix).

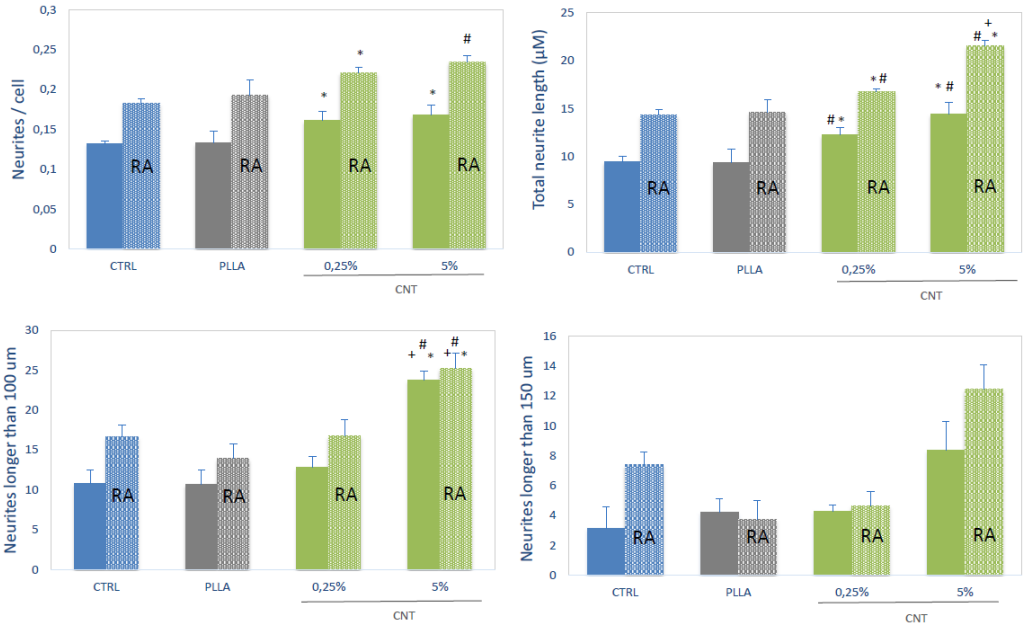

Figure 2-14: Differentiation results obtained with MWCNT@PLLA films at 0.25 and 5 wt%, as reference are reported the results for bare PLLA and for a polylisine-coated glass. All the tests were performed both in the presence and in absence of retinoic acid.

It is possible to note that the presence of CNSs inside the polymeric matrix can favor the growth of neurites. In particular, for all the CNSs is visible an increase in the mean number of neurites per cell, and in their length. This effect is much more remarkable in the sample containing 5 wt% of CNSs, and in particular with MWCNTs. With these CNSs also the number of neurites longer than 150 µm is remarkably enhanced.

At this point, we compared eMWCNT@PLLA 0.25% with ePLLA, and MWCNT@PLLA for both biocompatibility, and neuritogenic properties.

The highly porous morphology obtained through electrospinning is expected to better mimic the environment in which neurons normally develop.[58] In particular, the obtained geometry is similar in scale, and in 3D arrangement to the collagen, and

laminin fibrils of the extracellular matrix (ECM).[59] This aspect has fundamental implications in the further refinement of our bioengineering capability to mimic the neural environment. Moreover, the presence of MWCNTs within the PLLA matrix is thought to: (i) locally reduce the polymer electrical resistance at the nanoscale level which enhances neuronal network activity[60], and (ii) to feature nanoscale meshwork within the polymer, hence providing fibers with an optimal surface nanoroughness, and texture, ideal for cell adhesion, and for protein/growth factor retention.[61]

No difference in cell proliferation, and viability was found when growing cells onto the fibrous or film scaffolds, or onto the poly-L-lysine coated control wells (Fig. 2-15A).[50]

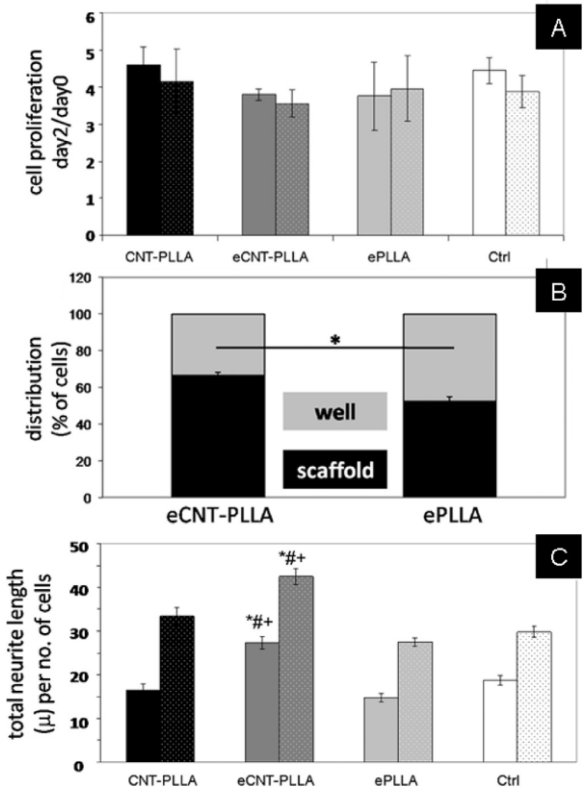

Figure 2-15: eMWCNT@PLLA scaffold effect on SH-SY5Y cell adhesion, growth and differentiation. (A) cell proliferation; (B) cell distribution and (C) cell differentiation. Data represent the mean ± SEM of three independent experiments performed in duplicate. (*) shows significance at p < 0.05 between cells seeded onto eMWCNT@PLLA scaffolds and control (poly-L-lysine coated wells). (#) shows significance at p < 0.05 between cells seeded onto eMWCNT@PLLA scaffolds and ePLLA scaffolds. (þ) shows significance at p < 0.05 between cells seeded onto MWCNT@PLLA scaffolds and eMWCNT@PLLA/ePLLA scaffolds. Dotted bars refer to the corresponding retinoic acid treated samples.[50]

However, cells better adhere onto eMWCNT@PLLA (~66%) than onto ePLLA (~53%) (Fig. 2-15B). Furthermore, the total neurite length is significantly increased in samples seeded onto eMWCNT@PLLA. These results highlight an improved adhesion, and differentiation of cells growing onto eMWCNT@PLLA, possibly due to the combination of two factors. First, the fibrous morphology of the scaffold, with fiber diameters partially overlapping the diameter range of both axons (80 nm - 20 mm)[62] and collagen

fibrils (260 - 410 nm).[37a] Second, the presence of MWCNTs that (i) lower scaffold resistance and, most important, can induce beneficial effects at the nanoscale based on their electronic properties[60a, 63], and (ii) can provide sites for cellular anchorage and guidance of cytoskeletal extensions thanks to their nanotopography.[64]

Indeed, the superimposition (Fig. 2-16C, F, I) of the fluorescent images of the cells (Fig. 2-16B, E, H) stained with a cytoplasmatic dye, and the bright field images of the corresponding portion of the scaffold (Fig. 2-16A, D, G) shows that the newly formed neurites elongate following the direction of fiber orientation. This is a strong indication that the scaffold topography guides cells outgrowth, and opens up the bright perspective of obtaining a polarized neurites outgrowth and elongation upon previous fibers alignment.

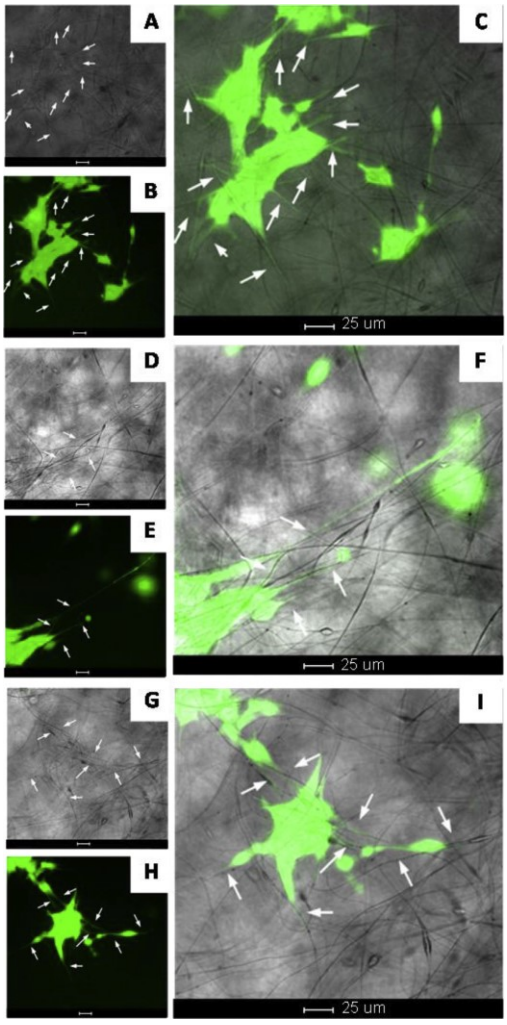

Figure 2-16: SH-SY5Y cells extend neurites following the scaffold fiber orientation. (A), (D), (G), bright field images of the eMWCNT@PLLA scaffold; (B), (E), (H), fluorescent images of RA treated SH-SY5Y cells stained with Calcein-AM; (C), (F), (I), superimposition of the fluorescent and corresponding bright field images. White arrows indicate neurites following the scaffold fibers orientation. Image magnification is 32X.

For comparison to previous performance with SH-SY5Y cells,[50] we used the same electrospun eMWCNT@PLLA 0.25% scaffolds to provide human circulating multipotent cells (hCMCs) with submicrometric-sized fibers able to mimic the neuronal processes and the fibrillar collagenous, and laminin component of the ECM. Cell proliferation is not impaired with respect to control when culturing hCMCs onto eMWCNT@PLLA scaffolds, which show to drive cell morphological changes toward neuronal differentiation (Figure 2-17), such as diameter narrowing and fusiform shaping of the cell bodies.

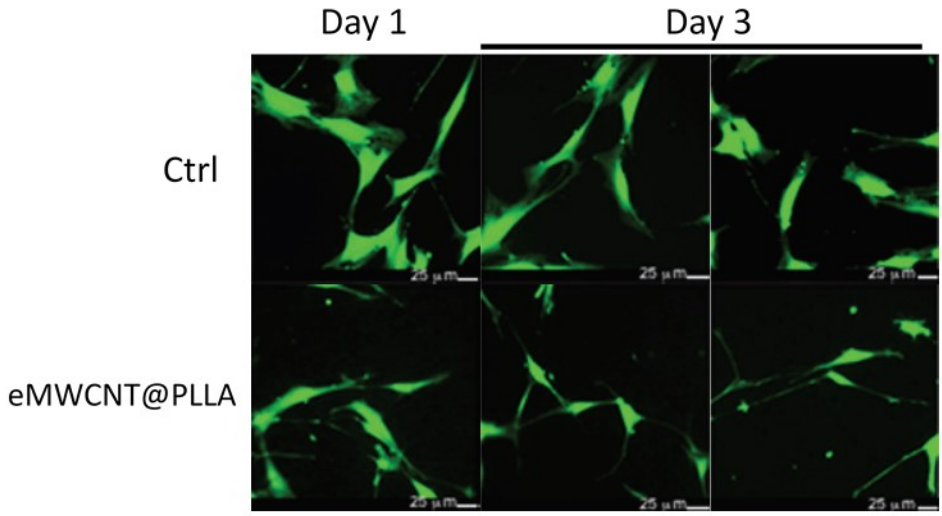

Figure 2-17: Human circulating multipotent cells (hCMCs) stained with Calcein-AM; image magnification is 32X. .

Moreover, in comparison to control, hCMCs increasingly show a polarized appearance with longer, and numerous neurite-like protrusions. The superimposition of the Calcein-AM stained cells, and the bright field images of the corresponding portion of the eCNT–PLLA scaffold shows that hCMCs protrusions follow scaffold Fiber orientation (as highlighted by white arrows in Figure 2-17). Quantitative gene expression analysis reveals a scaffold- dependent upregulation of some markers of the neuronal lineage. Indeed, a higher expression of *Nestin*, *TUB*β*3* and *MAP2* is observed in cells grown onto eCNT–PLLA compared with controls, suggesting that a neuronal differentiation program activation has started.

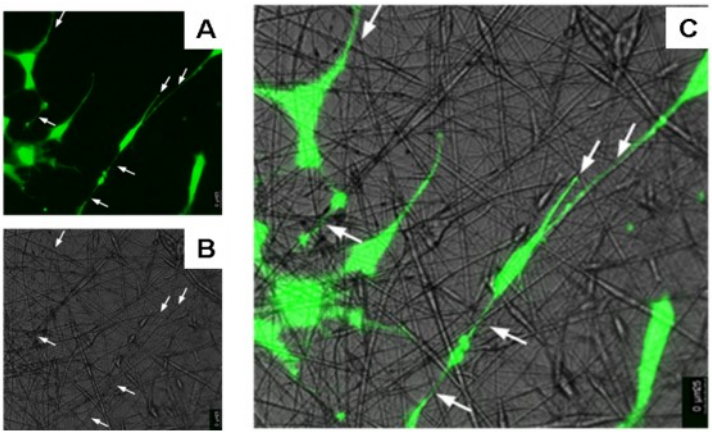

Figure 2-18: hCMCs cells differentiating on. (A) bright field images of the eCNT-PLLA scaffold; (B) fluorescent images of RA treated SH-SY5Y cells stained with Calcein-AM; (C) superimposition of the fluorescent and corresponding bright field images. White arrows indicate neurites-like features following the scaffold fibers orientation. Image magnification is 32X.

Morphological evidence highlights that, when growing onto MWCNT@PLLA scaffolds, hCMCs are committed toward neuronal lineage, and show typical features of neuronal differentiation, such as reduced size of cell bodies, polarized appearance, and presence of neurite-like protrusions. Moreover, such protrusions (which align to fibers, when growing onto eMWCNT@PLLA, confirming observations with SH-SY5Y cells) are tipped with fan-shaped structures resembling growth cones. Concerning qPCR evidence, hCMCs seeded onto the CNT@PLLA scaffolds show an early upregulation of *Nestin*, indicating that cells are undertaking the differentiation pathway toward neural progenitor cells like neurons, oligodendrocytes and astrocytes. Concomitant upregulation of *TUBβ3*, specific to immature, and post-mitotic neurons[65] confirms that the majority of cells are acquiring a neuron-specific commitment. *MAP2* expression is upregulated as well in CNT@PLLA samples and it progressively increases until day 5 of differentiation. Indeed, it is known that the expression of *MAP2* is temporally shifted with respect to neuron-specific *TUBβ3* as, during neurite initiation, *MAP2* is later involved in the coordinated reorganization of cytoskeleton networks of microtubules, and filamentous actin.[66] Aforementioned results suggest that our nanocomposite scaffolds are able to initiate hCMCs neuronal differentiation through the expression of neuronal specific markers.[67]

2.1.5 **Preparation and tests of nerve implant prototypes**

Peripheral nerve injuries following traumas are an epidemiologically relevant problem due to their poor outcome. They still need an appropriate and effective management. In the last decades, improvements in the field of biomaterials and nanotechnologies have offered a suitable alternative to more invasive methods such as autografts or allografts, leading to the production of far more sophisticated scaffolds which are able to interact with cells and macromolecules on a nanoscale.[68]

Starting from the promising results obtained with our composite materials in terms of biocompatibility and bioactivity, we began to prepare prototypes of Nerve Guide Conduits (NGCs) for *in vivo* tests. Due also to our results with neurons, and stem cells obtained *in vitro* with our eMWCNT@PLLA 0.25%, we decided to use this kind of fibrous materials for the preparation of our first substrates. The main problem to overcome was that such nanofibers tend to be too much electrostatic, and soft to be handled alone as implant. So, we decided to deposit a layer of PLLA fibers containing MWCNT-PhOMe onto a thin film of neat PLLA; in this kind of prototypes the film layer have to sustain the active fiber layer giving to the substrate the mechanical properties needed for the use as an implant. Through solvent evaporation in a Teflon mold, and optimizing the concentration of the PLLA solution (3% wt% in $CHCl_3$), we have been able to obtain thin film of PLLA of 80 µm of thickness (height 5 cm, length 7.5 cm), that was the best compromise between flexibility and tightness of surgical stiches. (Fig. 2-19)

Figure 2-19: Image of the PLLA film used to prepare our first implant prototype.

To deposit the fibers layer onto the film of PLLA firstly we tried to combine them after their separate preparation, but the conjunction between the two layers was not very stable. So, we decided to try to electro-spin the fibers layer directly onto the film. We firstly perform a low deposition of electrospun nanofibers in order to analyze the

contact point between the two layers. As we can see from the SEM images (Fig. 2-20) there are lots of points in which a section of a fiber is embedded into the film.

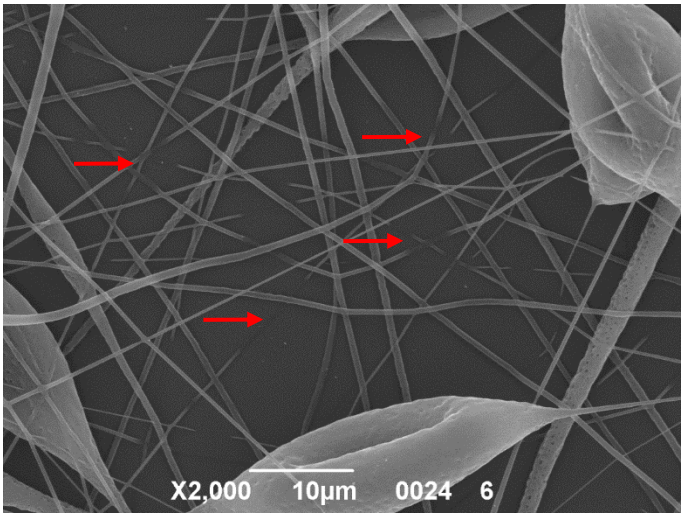

Figure 2-20: SEM image of the surface of the PLLA film with a low deposition of electrospun fibers (red arrows mark conjunction points between the two layers)

These conjunction points, together with electrostatic interactions will surly provide good stability to the substrate mantaining the fibrous and the film layers well attached. After that, we prepare the real first prototype performing a complete deposition of the fibers onto a PLLA film obtaining the scaffold in figure 2-21.

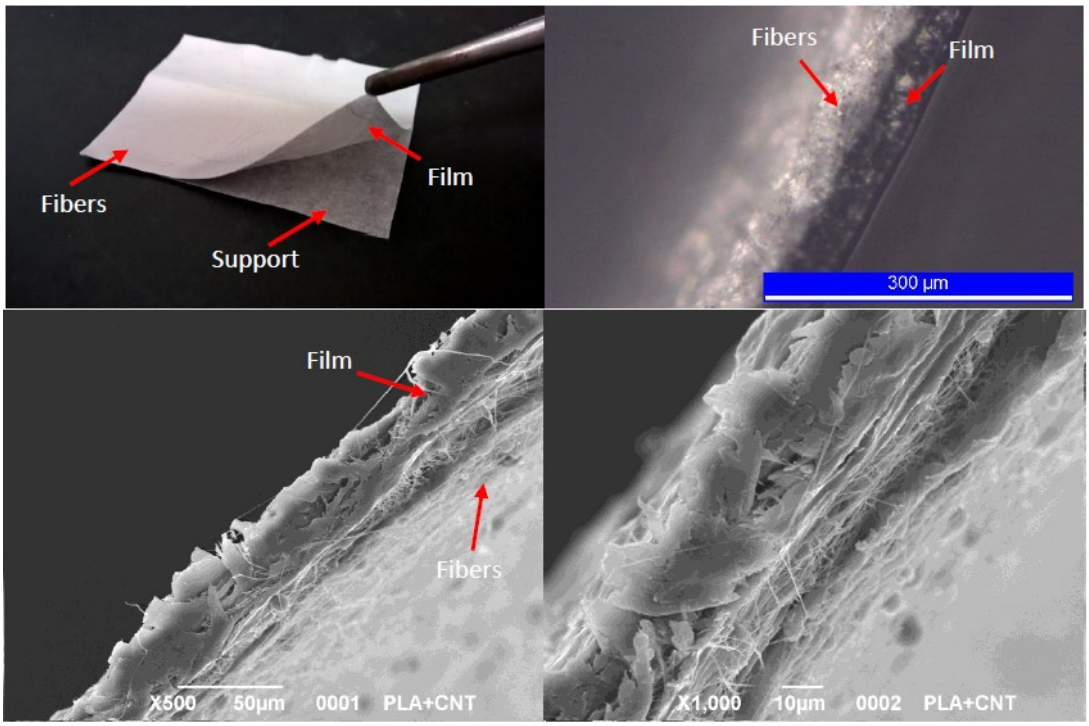

Figure 2-21: Images of the impermeable prototype. In the first image it is possible to see the scaffold onto the support and protective non-stick layer. In the microscope images it is possible to see the PLLA layer covered of the fibers layer.

As it is clear from its structure, this first prototype results completely impermeable to water, since the PLLA film layer is not porous. In literature it is, instead, well reported the importance of using permeable substrate as NGCs.[69] So, we decided to use the 3D printing technology to find a way to replace the impermeable PLLA layer. Using a fused filament fabrication (FFF) 3D printer, we have been able to design and obtain PLLA grids, that can be use as support for the fibers layer maintaining the mechanical properties of flexibility and biocompatibility but giving to the scaffold a complete permeability. Using this technique, we can obtain grid with the desired shape, dimension and permeability (two examples with different mesh size are shown in Figure 2-22).

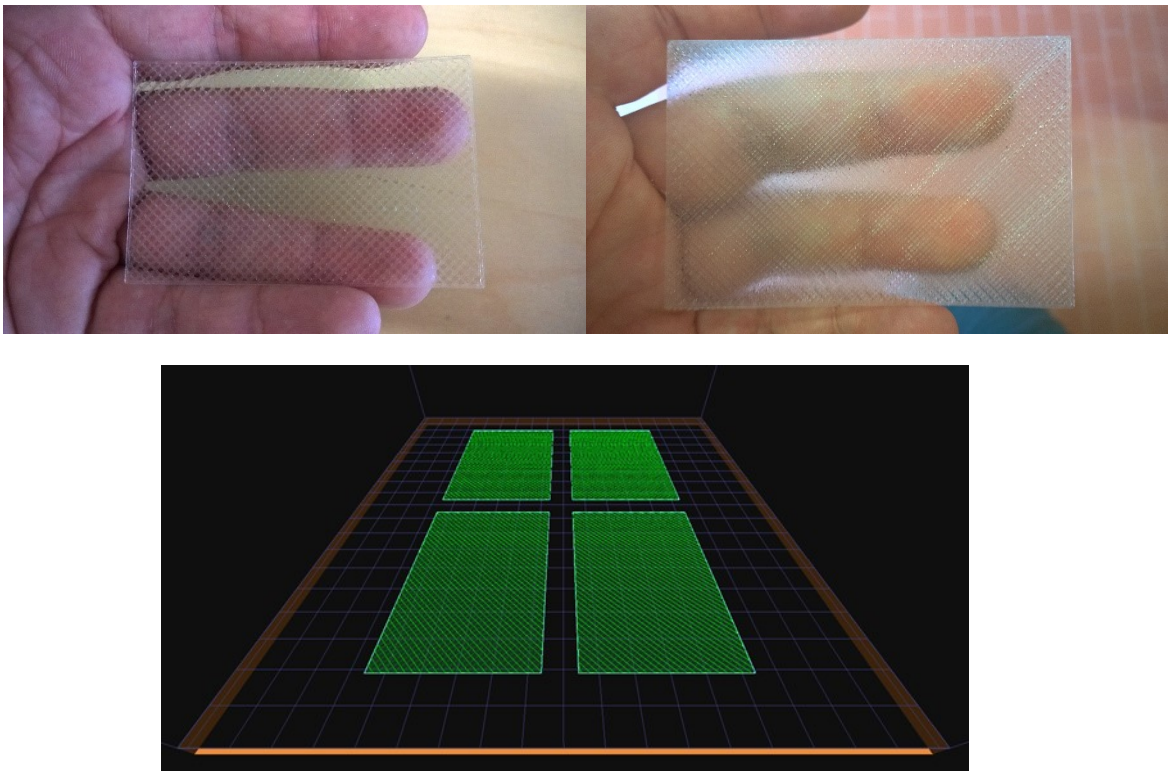

Figure 2-22: Images of two different 3D printed PLLA grids and the model used for the printing process.

With these 3D printed grids we moved to the preparation of the "permeable" prototypes simply using the same procedure used for the PLLA films before, performing the electrospinning to cover the grids with the layer of PLLA fibers containing the functionalized MWCNT-PhOMe. (Fig. 2-23)

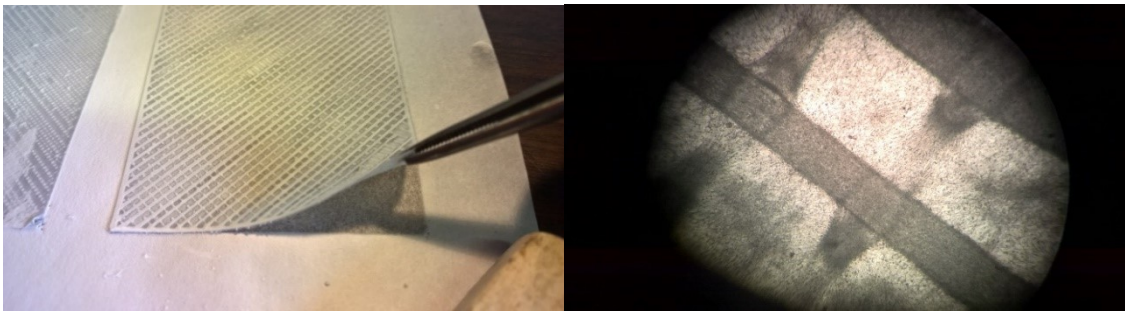

Figure 2-23: Images of a permeable prototype, in the microscope magnification it is possible to see the PLLA fibers layer covering a pore of the grid.

2.1.5.1 In vivo tests

We have then perform the first *in vivo* tests of these substrates. In order to understand the effect of the presence of MWCNT into the PLLA matrix all our prototypes have been prepared also in a "blank" version made only of neat PLLA. *In vivo* tests have been performed on sciatic nerve of mice; the nerve was transected, repaired with suture and then wrapped with our novel wrapping sheet. (Fig. 2-24, 2-25). Control mice were only transected and repaired with suture. All the operation and analysis on mice were performed in collaboration with the group of Prof. Bassetto from the Clinic of plastic and reconstructive surgery at the department of neuroscience, and in particular with Dr. A. Pontini.

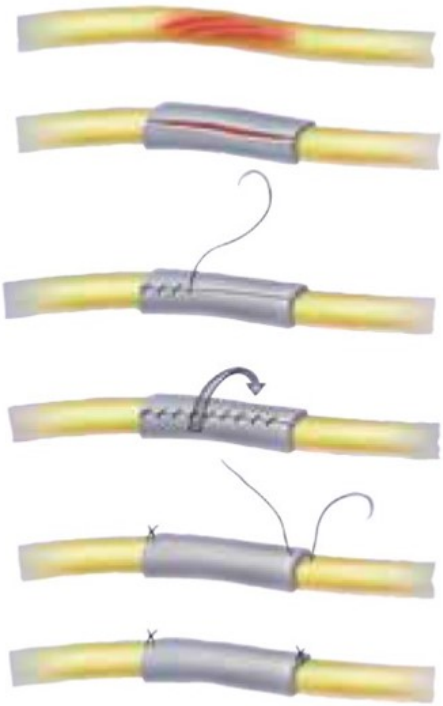

Figure 2-24: Schematic illustration of the use of a NGCs. Image provided by Integra®.

Figure 2-25: Photo of one of the in vivo tests, in the image on the left it is possible to see the sciatic nerve before the operation and the implant; in the image on the right it is possible to see the sciatic nerve after the operation with the implant in his position. (the implant is barely visible when wet)

We test our implant on 10 mice, and we monitored their status several times after the operation until the day of sacrifice.

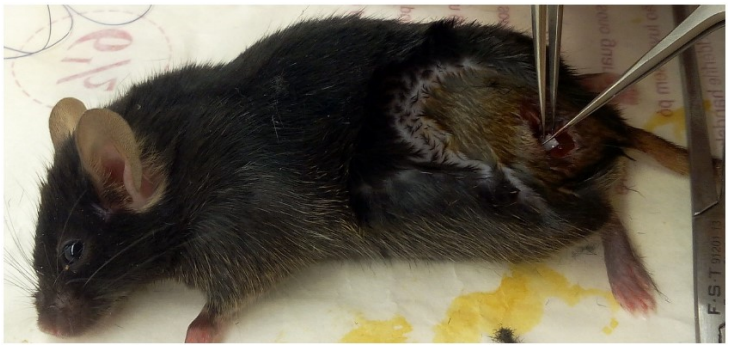

Figure 2-26: Photo of one of the operations.

We performed general evaluation, the De Medinaceli test, the Open Field test and electromyography (Fig. 2-27) before the sacrifice, and after that a histology of the nerve.

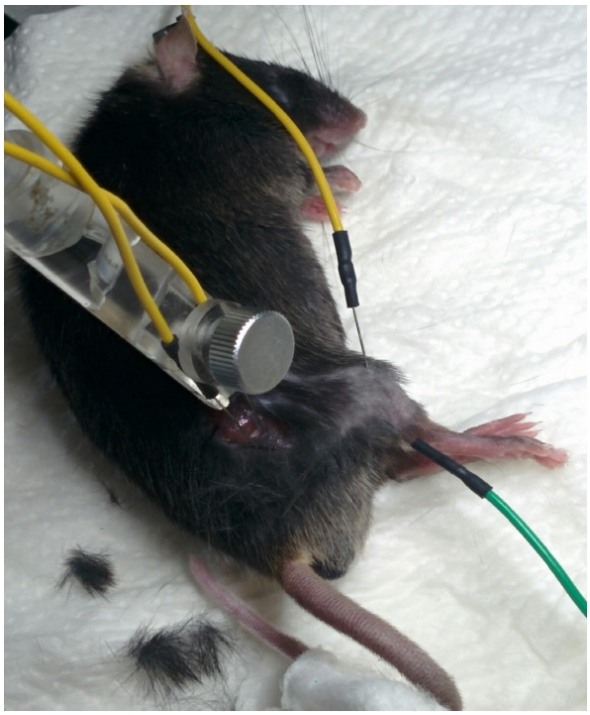

Figure 2-27: Electromyography performed on an operated mouse.

In particular, for the general evaluation the animals were monitored since the first day after surgery until the day of sacrifice. We evaluated their motor behaviors, gait abnormalities, limb displacements, walking and running behaviors, general well-being, appetite and arousal. The De Medinaceli test is used to evaluate walking tracks, and can be very useful to study functional recovery since proper walking requires coordinated functions involving sensory input, motor response, and cortical integration. The open field activity monitoring system comprehensively assesses locomotor and behavioral activity levels of mice, which can be correlated with locomotive function. In particular, the open field is a useful tool for assessing locomotive impairment in animal models of neuromuscular disease. This tecnique measures the *total distance travelled,* and thereby measures the *medium speed*, focus on submaximal exercise performance and quality of life. Overall, this makes the open field activity test a useful outcome measure to use in preclinical trials.

Results from De Medinaceli and Open Field tests were statistically different between CNT-PLLA mice and sutured mice. The CNT-PLLA group showed a faster, and greater improvement in all the performed tests. Friedman's test indicated improvement in the CNT-PLLA group has been far more relevant. Electrophysiology confirmed the absence of Wallerian degeneration and the presence of a biphasic compound muscle action potential (CMAP). Histology showed no adhesions, and no fibrotic reaction. Muscle showed a certain grade of atrophy, albeit higher among the suture group.

We can state that our technology is really promising for the preparation of implant for neural surgery. Our eMWCNT-PhOMe@PLLA nanofibers based scaffold has proved to prevent Wallerian degeneration, being fully biocompatible and protective from adhesions and the neuromas at the same time.

2.2 Carboxylic and vinylic functionalizations

In this section, it is presented the use of the Tour reaction to introduce onto the CNSs functional groups useful for a second step derivatization. The most used reaction in literature for the functionalization of CNSs is the oxidation, that can both provide an enhancement in the solubility of the material, and carboxylic moieties that can be really useful to anchor other group onto the nanostructures. As mentioned before, this procedure can greatly reduce the conjugation of the CNSs, and so compromise their properties. Indeed, we perform the functionalization with p-benzoic acid, in order to obtain the introduction of carboxylic acid with a limited introduction of sp^3 defects into the sp^2 lattice of the CNSs.[70] The reactivity of the introduced carboxylic groups can be tested through the amidation with labeled moieties, as a model for a possible post-functionalization with biologically relevant molecules. In particular, this could open the door to a future covalent grafting of the biomimetic peptides, that we already studied in our previous works for their effect on the differentiation of neural cells.[50, 67, 71]

After that, we will study the introduction of styrene groups, that can provide anchor point for the "grafting from" polymerization of polystyrene. In this way, the functionalization of the nanostructure can provide a covalent interaction with the polymer matrix. This should provide a more efficient contact between the matrix and the filler, determining the properties of the final composite material.

2.2.1 **Functionalization with benzoic moieties**

Most of the chemical modifications of the CNSs found in literature make use of carboxylic groups for the decoration of the CNSs.

The carboxylic groups are usually introduced by oxidation of the CNSs, a methodology highly invasive that introduces a wide variety of oxygen-related groups, that can only partially be converted in carboxylic functionalities. Furthermore, the CNSs increase their resistivity due to the high level of damage introduced with the oxidation.

The addition of *p*-carboxyphenyl groups on the CNSs through the Tour reaction allows us to obtain a selective introduction of the functional group with the choice of the reagent. The introduction of defects is contained, as the addition of the molecules to the outer layer of the CNSs prevents further undesired damaging of the structure.

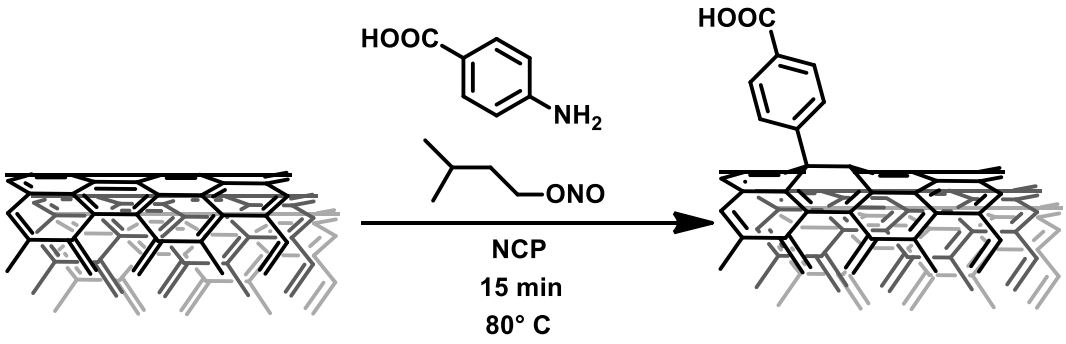

Figure 2-28: MWCNT-PhCOOH reaction scheme.

The carboxylic functionality can enhance the solubility of the CNTs in water, a parameter that is used as a figure of merit for the evaluation of the reaction outcome.

The grafting of MWCNTs with *p*-carboxyphenyl groups (in this section we will refer to p-carboxyphenyl functionalized MWCNTs as: MWCNT-PhCOOH) was studied in a wide range of reactant equivalents, in order to find the optimal reaction conditions. The reaction was at first tested on 0.5 eq of *p*-aminobenzoic acid at 80 ˚*C* for 15 minutes. The TGA of the product shows a weight loss lower than 4% at 450 ˚*C* suggesting a low degree of surface modification.

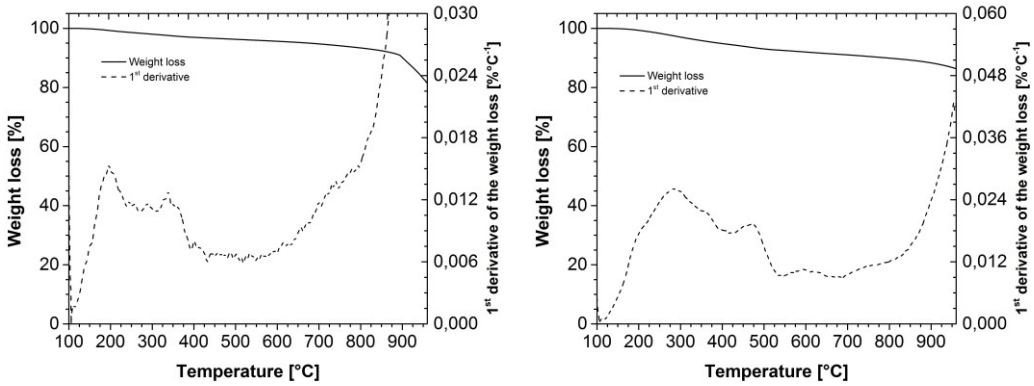

Figure 2-29: TGA of MWCNT-PhCOOH functionalized for 15 min (left) and for 24 hours (right).

The reaction was also tested with the same amount of reagents but with a 24 hours reaction time, in order to understand if the low grafting was due to the formation of side products or to kinetic reasons. For a 24 hours reaction time the weight loss is above 8%, validating the hypothesis of a kinetic limitation on the 15 minutes reaction that, requires indeed more time to reach higher yields.

A higher degree of functionalization can be detected also because the degradation of the grafted molecules shifts to higher temperatures. The outline of the first derivative of the weight loss does not change, as it presents in both cases two main peaks, but the onset temperatures of the two degradation processes are shifted to higher temperatures.

In order to understand whether the grafting can be boosted toward higher yields, maintaining the profitable short reaction time of 15 minutes, the number of equivalents of p-aminobenzoic acid was explored maintaining constant the other reaction parameters.

In table are summarized the results obtained in terms of weight loss and the solubility of the first extracted fractions.

Equivalents of *p*-aminobenzoic acid	Weight loss at 500°*C*	Solubility in water [mg/mL]
0.1	3.4%	null
0.5	3.6%	null
2.5	9.6%	0.31

The best result was reached at 2.5 eq of *p*-aminobenzoic acid with a solubility of 0.31 mg/mL in deionized water.

In order to further prove the presence of carboxylic groups, it was studied the stability of the dispersion in different acidic, and basic aqueous environment. The hypothesis is that the aggregation of MWCNT-PhCOOH in water is controlled by two components. The first one is common to all functionalized-CNSs, and is the steric hindrance between the functional groups that can prevent CNSs aggregation; the second, and more relevant from our perspective, is the presence of charged groups on the CNSs due to the protonation/deprotonation of the carboxylic groups. If we reduce the experimental situation to a simplified model, where the pristine MWCNTs are ideal nanotubes without any defects, that can provide charged groups, and the MWCNT-PhCOOH are nanotubes with the outer layer grafted by *p*-carboxyphenyl groups. In the first case the nanotubes aggregation should be controlled only by Wan der Walls forces, so it should not be affected by acidity or basicity of the solution. Instead in the second scenario the solution stability should be governed by the protonation, and deprotonation of the carboxylic groups.

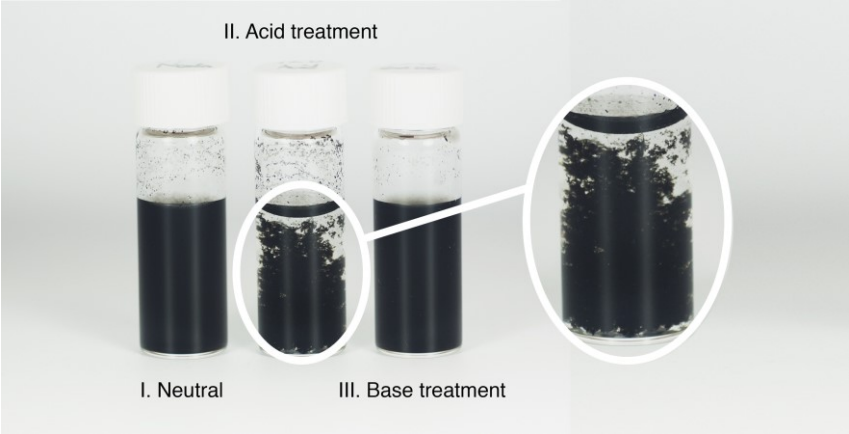

Figure 2-30: Acidity dependent solubility.

By controlling the acidity and basicity of the solution, it should be possible to protonate the carboxylic groups in acid conditions, hence lowering the solubility in water of the CNSs, while under basic conditions their deprotonation should enhance the solubility. Following this guideline, it was verified that indeed adding a droplet of acidic solution (0.1N HCl_{aq}) to a stable dispersion of MWCNT-PhCOOH the CNSs formed macroscopic flakes characteristic of unstable dispersions. When a droplet of basic solution (0.1N $NaOH_{aq}$) was added instead, any major difference could not be detected in the stability of the solution. Moreover, adding the basic solution to the acidified dispersion of MWCNT-PhCOOH, that have lost their stability in solution, will bring back the initial solubility. To make sure to evaluate the dispersion stability under the same timeline, the two dispersions have been sonicated for a minute after the droplet addition, in order to restore the dispersion at time zero. Starting from these qualitative but substantial results, a quantitative prove of the presence of the carboxylic acids was researched.

2.2.1.1 XPS characterization of MWCNT-PhCOOH

XPS measurements were performed in collaboration with Dr. Francesco Sedona from the Department of Chemical Sciences on MWCNT-PhCOOH, and pristine MWCNTs for comparison. The peaks of interest are relative to carbon 1s (C1s), and oxygen 1s (O1s) electrons. Given the structure of MWCNTs, oxygen should be present in small percentages due to a certain extent of defects on the nanostructures, therefore a hardly detectable oxygen signal is expectet for pristine MWCNTs. A significant increase in the O1s emission could be a good indication of the addition of p-carboxyphenyl groups on the CNTs.

A study on terephthalic acid multilayer adsorbed on epitaxially grown graphene was used to assess the expected peak shape, and energies relative to carboxylic groups.[72]

Figure 2-31 shows the superimposition of O1s data from pristine MWCNTs and the functionalized MWCNT-PhCOOH. As expected, the starting material shows a weak signal that is unsuitable for peak analysis, as the noise/signal ratio is too high, but it is a good reference for the comparison of the signals. The O1s emission from the functionalized product is significantly higher, confirming a successful addition of oxygen containing molecules by Tour reaction.

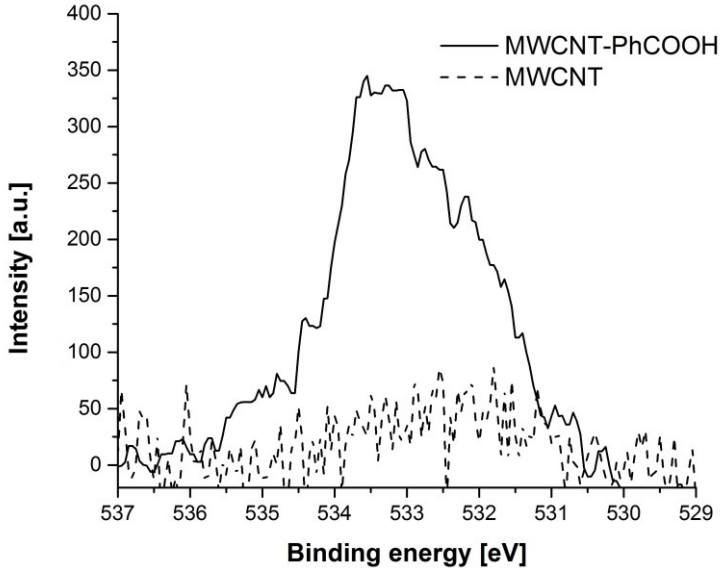

Figure 2-31: XPS O1s spectra prior (MWCNT) and after the functionalization (MWCNT-PhCOOH).

The analysis of the O1s and C1s signals is reported to verify if the signal is quantitatively compatible with carboxylic oxygen.

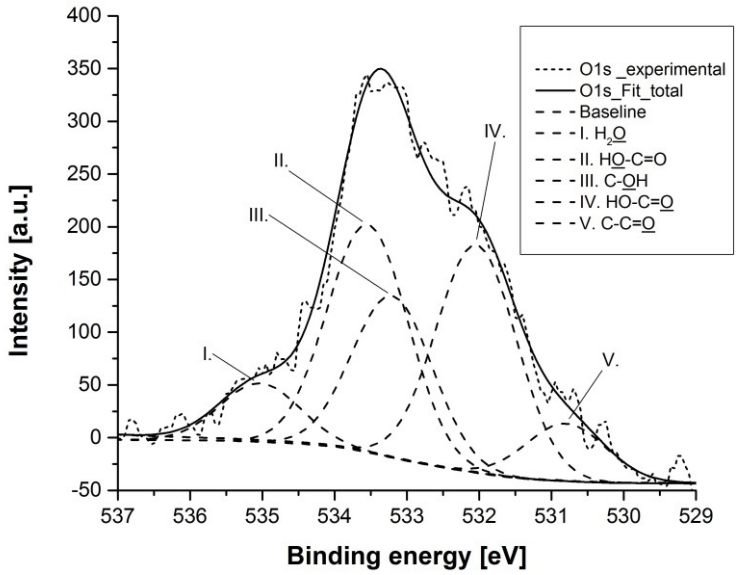

Figure 2-32: *O1s* XPS analysis.

The deconvolution of the O1s peak shown in Figure 2-36 was performed with *XPSpeak* software. According to the literature,[72] a chemical shift of 1.5 eV was imposed between the two main peaks ascribable to the OH, and CO signal of a carboxylic group. Furthermore the area of the two peaks is expected to be equal because there is one oxygen of each type for every group. In order to have a convergent fit, three auxiliary peaks are necessary.

	C−C=O	HO−C=O	C−OH	HO−C=O	H_2O
Binding energy [eV]	530.8	532.0	533.2	533.5	535.0
Area	77.4	303.1	211.4	303.1	69

O1s MWCNT-PhCOOH peak assignment and area

In table are shown the results of the deconvolution, where the peaks C−C=O, and C−OH are relative to non-carboxylic signals, and H_2O is attributed to water according with the literature.[73]

The analysis of C1s was performed on the basis of these results; due to the different cross sections of the elements and the apparatus configuration, the signal O1s is about twice as intense as that of C1s. The fit on C1s was performed by imposing the area of the COOH peak as half of the intensity of that found in the (O1s) signal.

	C sp^2	C sp^3	HO−C	C=O	COOH	$\pi - \pi^*$
Binding energy [eV]	284.5	286.1	286.21	287.6	289.22	291.3
Area	7633	1.222	105	37.5	150	351.6
% respect to C sp^2		16%	1.37%	0.5%	1.96%	4.6%

C1s MWCNT-PhCOOH peak assignment and area

In table are reported the results of the fit on the carbon signal. The quantitative analysis shows that the carbon bond to carboxylic groups constitutes almost the 2% of the whole structure. Considering that the TGA suggests the molecules grafted on the CNTs are the 9% (w/w) of the structure, and that the carboxylic group contributes roughly as a third to the total weight of the grafted molecule (p-carboxyphenil groups), the 2% signal obtained by XPS measurement is consistent with the amount of carboxylic groups selectively introduced by Tour reaction. Even though the signal could be attributed to carboxylic groups, it must be mentioned that given the shift range of the peaks reported in literature, the peaks could be also associated to different functional groups as the assignment in different works can be quite arbitrary.

2.2.1.2 Amidation on the functionalized CNSs

Given the absence of indisputable results from the spectroscopies, an indirect evidence of the presence of carboxylic groups could come from an amide coupling that would prove both the presence of the functional groups and their availability for further reactions.

Considering those assumptions, the coupling of a paramagnetic label was studied. 4-amino-TEMPO was used because it is a well known paramagnetic molecule detectable by EPR spectroscopy. and should be easily identifiable. EPR measurements have resolution limit in the order of the nanomole. which is compatible with the degree of coupling expected in our sample. The technique's signal is only responsive to the paramagnetic molecules that are selectively introduced, so the presence of contaminations affecting the signal of the TEMPO group should be avoided. Furthermore amino-TEMPO moieties can't give strong π-π staking with the surface of the CNSs like usually do chromophores and fluorophores so the only interaction that can occur between the EPR label and the nanomaterial is the amide bond formation.

The coupling was carried on the most soluble fraction of MWCNT-PhCOOH, in order to minimize the presence of unfunctionalized MWCNTs, that would lower the statistical probability of positive encounter between the amine, and the activated carboxylic acid.

The amidation reaction with NHS, DIPEA, and EDC·HCl coupling agents was carried out for 4 days at room temperature to obtain the EPR labeled MWCNTs (MWCNT-PhCONH-TEMPO).

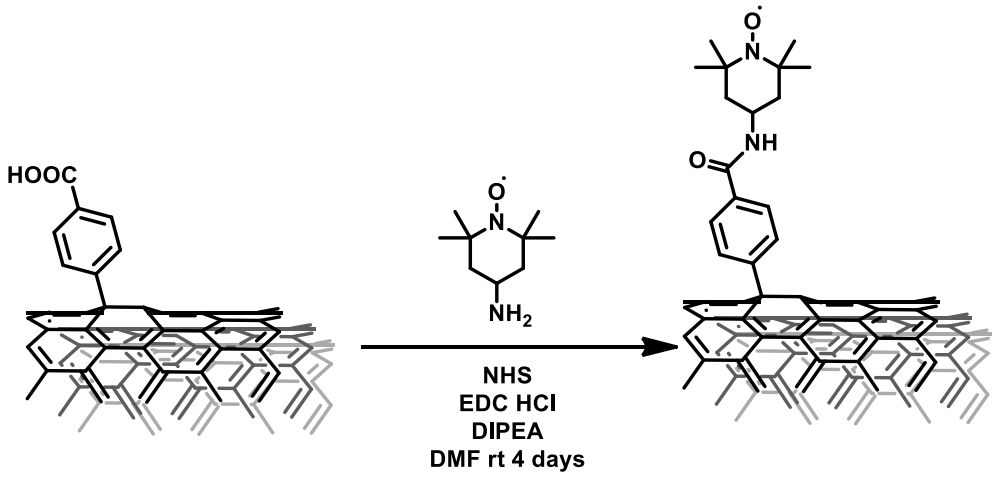

Figure 2-33: Amide coupling of 4-aminoTEMPO.

The EPR measurements were performed in collaboration with Prof. Lorenzo Franco, from the Department of Chemical Sciences. Figure 2-34 reports the EPR spectrum of MWCNT-PhCONH-TEMPO in solid phase deposited on a polytetrafluoroethylene (PTFE) membrane filter. Prior to the acquisition of the spectra, it was checked that the

membrane did not interfere with the measurements. The typical EPR spectrum of TEMPO molecules bound to CNSs can be recognized in figure.[74]

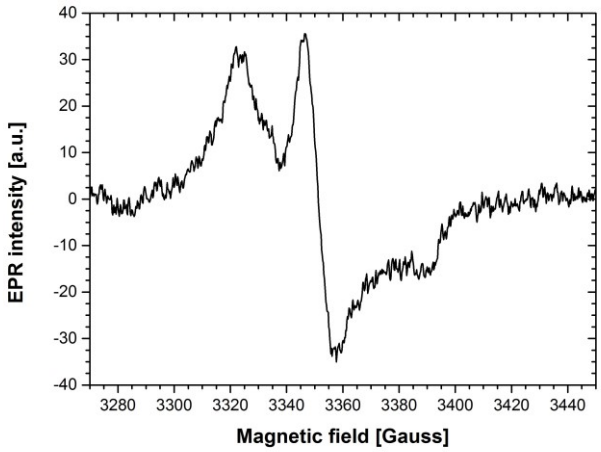

Figure 2-34: EPR spectra of MWCNT-PhCONH-TEMPO.

The interaction between nitroxide radicals can bring to the broadening of the EPR lines.[75] Such a broadening, detected on MWCNT-PhCONH-TEMPO, can be explained by the presence of regions characterized by a high density of nitroxide radicals on the CNTs. In fact, a local higher degree of functionalization on MWCNT-PhCOOH can be expected for the strained portions of the CNTs. Therefore such regions are susceptible to a high density of amide bonds, hence a high density of nitride radicals.

Control measurements were performed on the wastewater of the washing procedure in order to verify the effectiveness of the protocol.

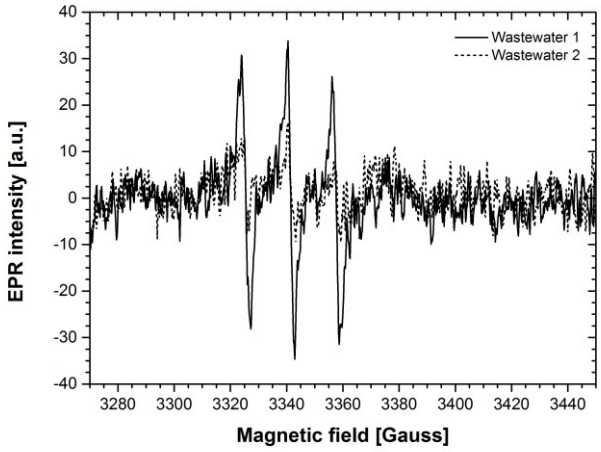

Figure 2-35: EPR spectrum of the wastewater of MWCNT-PhCONH-TEMPO.

In these spectra it is possible to see the typical spectral behavior of TEMPO label molecules free in solution, that decrease in intensity from the wastewater of the first purification step to the second one disappearing completely in the third.

After the amidation with the small amino-TEMPO molecules, we test the possibility to use the same amidation reaction to functionalize the MWCNTs with a bigger molecule, a peptide synthetized by Prof. A. Moretto from the Department of Chemical Sciences. The peptide, again, present in the sidechain the TEMPO group for the EPR analysis.

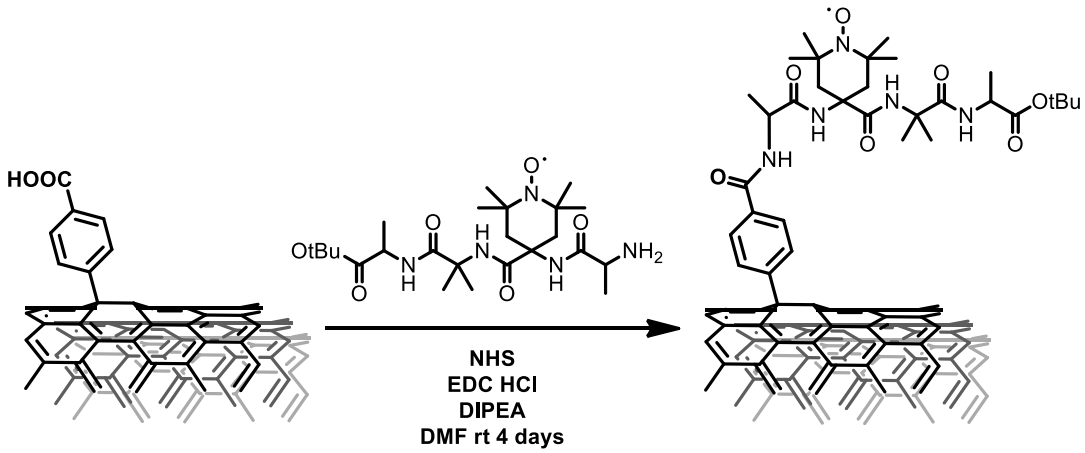

Figure 2-36: Reaction scheme for the amidation with the TEMPO-labeled peptide.

After the amidation and the purification procedure we have been able to detect the presence of the TEMPO group also in this product. All the parameter for the reaction and for the purification was the same used for the amidation of amino-TEMPO. This tells us that this reaction is extremely useful for the functionalization of CNSs, also with complex and big structure, and in particular could be used to functionalize the MWCNTs with biomimetic or bioactive molecules enhancing their biological properties.

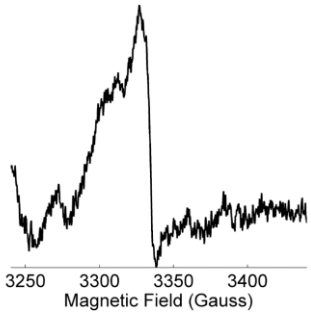

Figure 2-37: EPR spectra of the peptide-functionalized MWCNTs.

Comparing the TGA analysis of the MWCNTs before and after the amidation (MWCNT-PhCOOH and MWCNT-Peptide), it is possible to see that there is an enhancement in the weight loss due to the decomposition of the organic moieties. This is a second confirm that the amidation take place. Analyzing more quantitatively the thermograms, and

comparing the weight loss it is possible to estimate that almost 10% of the carboxylic moieties have been amidated.

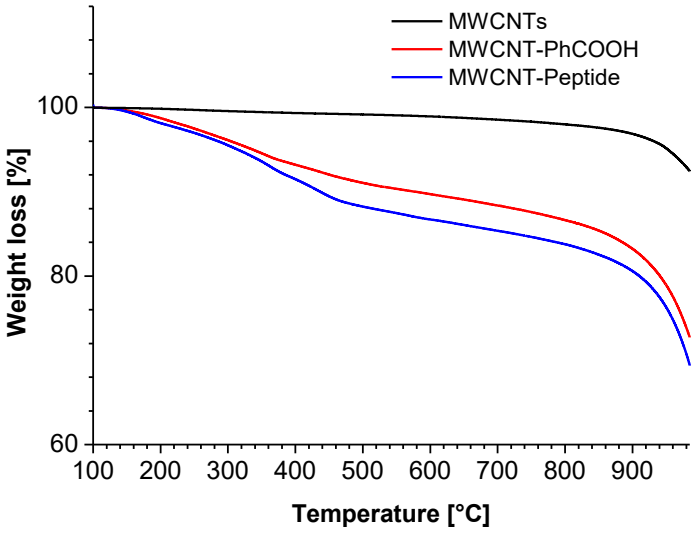

Figure 2-38: Overlap of the TGA of pristine MWCNTs (black curve), MWCNT-PhCOOH (red curve) and MWCNT-Peptide (blue curve).

These results suggest us that the introduction of carboxylic acid through the Tour reaction can be an useful tool for the preparation of more complex material by amidation reaction. In particular, of great interest for biological application, it is possible to perform the amidation with synthetic biomimetic peptide that can enhance the biocompatibility and the bioactivity of the CNSs.

2.2.2 **Functionalization with styrene moieties**

One of the polymers often found as a matrix for nanocomposite materials is polystyrene. It has great number of application due to its good mechanical, and thermal properties. In this section, we want to test the possibility to use the Tour reaction in order to prepare a functionalized CNS that could be covalently grafted to the matrix: aiming at the development of a nanocomposite material with covalent bonds between filler and polymer. With this aim, it was considered the decoration of MWCNTs with *p*-vinylphenyl (styrene) groups. A vinyl functionality should provide an anchor point for the *in-situ* polymerization of polystyrene. It should also guarantee a better interface between the functionalized MWCNTs and the polymer matrix regardless the *in-situ* polymerization.[76]

We start performing the functionalization in "common" conditions with 4-vinylaniline. In particular, the reaction was performed in NCP, for 15 minutes, at 80 °C, using isopentylnitrite, and p-vinylaniline in a stoichiometry of 1:1 between them.

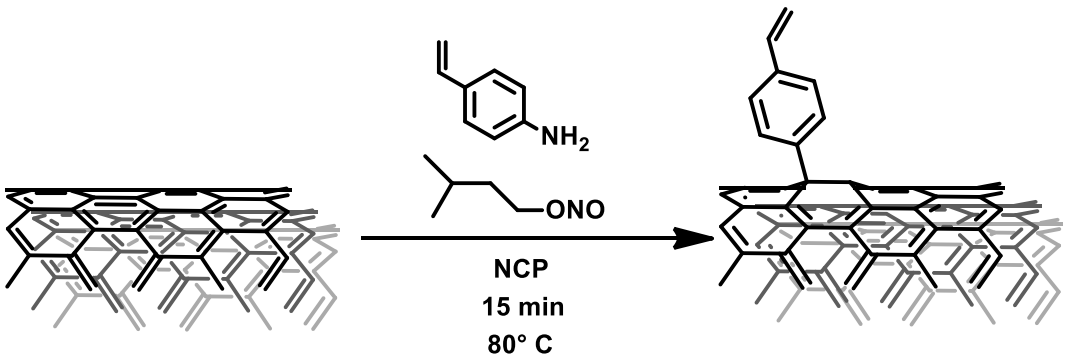

Figure 2-39: MWCNT-styrene functionalization scheme.

We tested the reaction using 2 equivalent of reactants with respect to the carbon atoms inside the CNSs but we did not obtain any increase in the solubility of the functionalized CNSs (MWCNT-styrene). Figure 2-40 shows clearly that the functionalization with styrene results in an efficient coverage of the CNS. The decomposition of the grafted molecules ends at around 450 °*C* and contributes with a 13% weight loss.

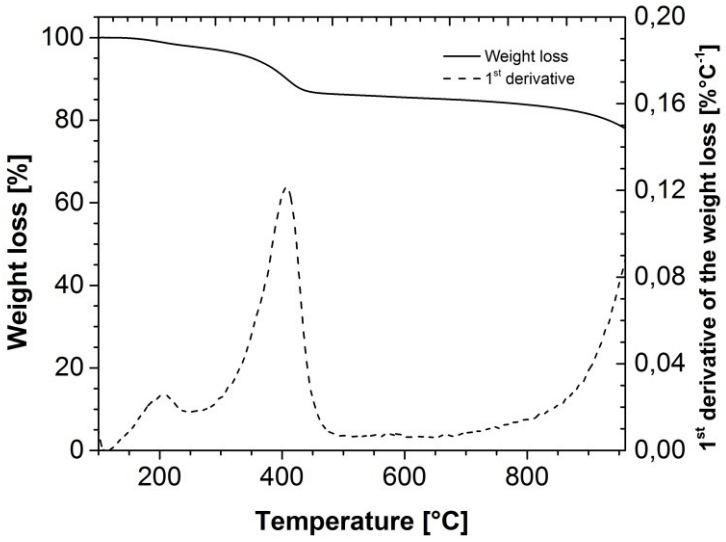

Figure 2-40: TGA of MWCNT-styrene in nitrogen atmosphere.

A weight loss above 10% suggest a high degree of functionalization, probably above the saturation density of the surface.

The solubility in DMF, and chloroform was studied, as the two solvents were employed in previous evaluations of the dispersion stability of MWCNTs derivatives. Unfortunately as mentioned above, the *p*-vinylphenyl group does not provide an improvement in the solubility, as it is null in chloroform, and comparable to pristine MWCNTs in DMF.

Therefore, it was necessary to look after a functionalization strategy that would enhance the solubility while maintaining the *p*-vinylphenyl functional groups.

A co-functionalization with *p*-vinylphenyl, and 4-methoxyphenyl groups was studied to counterbalance the low solubility of MWCNT-styrene with the well known contribute of 4-methoxyphenyl groups to the enhancement of the CNTs dispersibility.

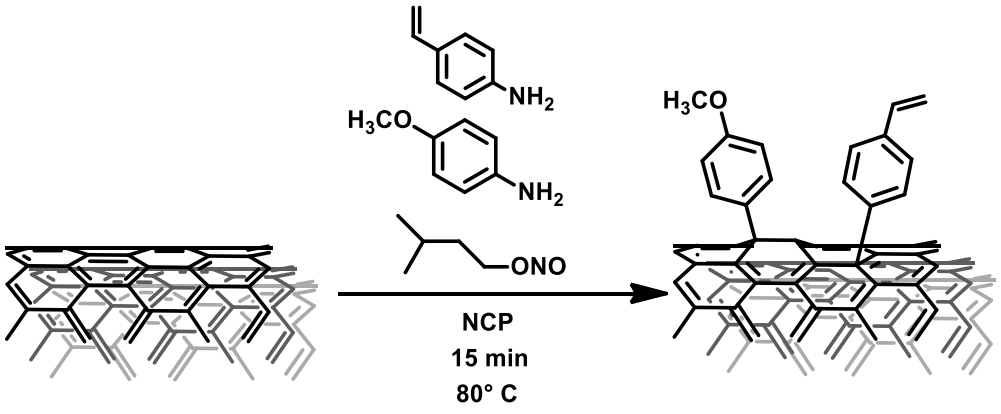

Figure 2-41: MWCNT-styrene-methoxyphenyl co-functionalization scheme.

The stoichiometry of the reaction was chosen on the basis of the previous results. The co-functionalizations were realized in two stoichiometric ratios: MWCNT-Cof-A was prepared using 1.5 eq of 4-vinylaniline plus 0.5 eq of 4-methoxyaniline, while MWCNT-Cof-B was prepare with 1.0 equivalents of both the reagents. 2.0 eq of isopentylnitrite were added matching the total equivalents of aniline derivatives in both cases. The reactions were carried for 15 minutes, at 80 °*C* under stirring and nitrogen flux following the standard protocol.

TGA measurements on co-functionalized does not provide relevant information regarding the composition of the over layer, apart from the total amount of molecules grafted. The two species added to the CNTs have a similar thermal degradation, and their contributions overlap. The measured weight loss at 500 °*C* is 14.4% for MWCNT-Cof-A, and 11.9% for MWCNT-Cof-B.

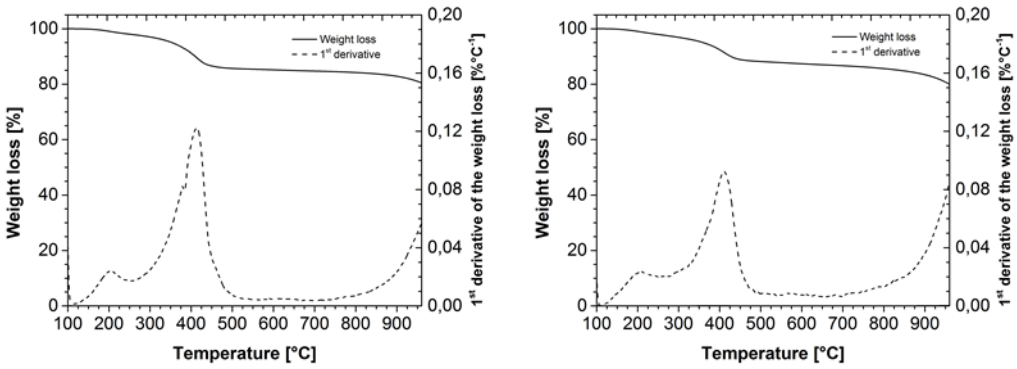

Figure 2-42: TGA of MWCNT-Cof-A (left) and MWCNT-Cof-B (right) in nitrogen.

The kinetic of the addition reaction is dependent from the substituent on the aniline derivative.[77] Aryl radicals with electron donating substituents showed faster additions, while derivatives with electron withdrawing groups required longer reaction times or higher concentrations of the reagents to achieve the same grafting degree. Therefore, the co-functionalization result could be related to a faster kinetic in the addition of the *p*-vinylphenyl groups, as the overall decoration follows the amount of the reagent. Nevertheless, is not available a characterization able to asses the local microstructure of the over layer. Therefore, the chemical composition of the over layer was researched by indirect evidence, such as the chemical reactivity of the *co-f* -MWCNTs and their solubility.

As the interest is focused on the composite preparation, the figure of merit relative to the outcome of the two co-functionalizations is left to the composite analysis.

2.2.2.1 "Grafting from" on the functionalized CNSs

The polystyrene composites were tested with different MWCNTs derivatives: MWCNT-Cof-A and MWCNT-Cof-B were co-functionalized, for a better compromise between anchor points and solubility and as reference pristine MWCNTs.

The composites were prepared by in-situ polymerization on dispersions of functionalized MWCNTs in styrene monomers, initiated by benzoyl peroxide. The nanotubes were dispersed by ultrasonication, and the reactions were carried at 80 °*C* for four hours. The degree of polymerization is time dependent, so the reaction time was set to obtain a solid material with high molecular weight chains.

Therefore, the characterization of the mechanical properties of the composite was not possible due to lack of a reproducible standard specimen. TEM measurements were performed to assess the surface modification of the nanotubes after the polymerization.

The TEM samples were prepared removing the polymer not attached to the CNTs, by dissolving the composite in THF and centrifuging the mixture to precipitate the CNTs; the supernatant containing the polymer was extracted and the CNTs were re-dispersed in fresh THF by ultrasonication. Repeating this procedure, it was possible to perform TEM measurements on CNTs clean from un-grafted polymer.

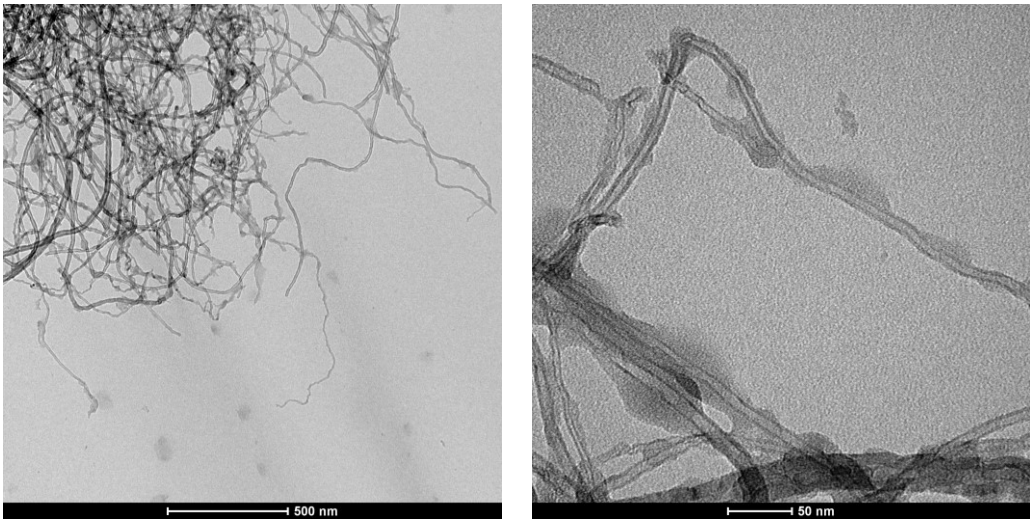

Figure 2-43: TEM images of MWCNT-Cof-A in situ polymerized.

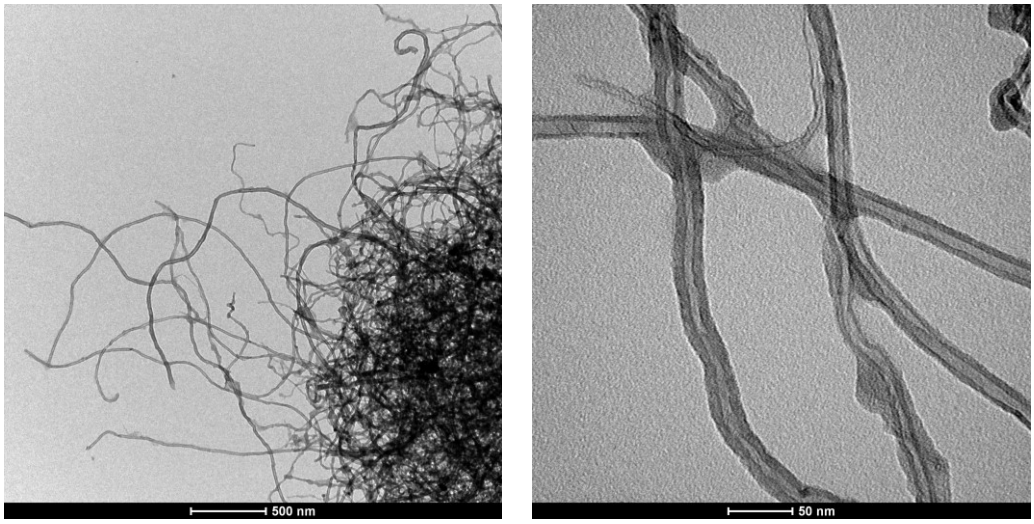

Figure 2-44 TEM images of MWCNT-Cof-B in situ polymerized.

As a control for the separation procedure polystyrene was polymerized on a dispersion of un-modified MWCNTs, and the aforementioned washing procedure was applied.

The in-situ polymerizations MWCNT-Cof-A and MWCNT-Cof-B resulted in CNTs coated by a layer of polystyrene covalently bound to the nanotubes, as it can be seen in Figures 2-43 2-44, while the un-modified MWCNTs do not show such a layer. (Figure 2-45).

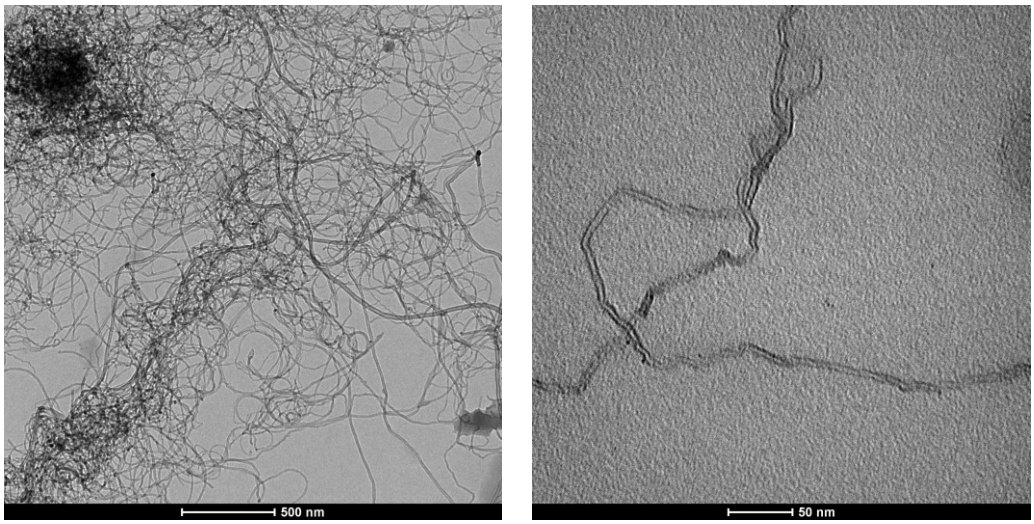

Figure 2-45: TEM images of pristine MWCNTs in-situ polymerized.

So It is evident that the cofunctionalization process can provide nanostructure with a much more complex combination of the desired properties. We have indeed, obtain MWCNTs enough soluble and with the right functionalities to be use efficiently in a grafring from polymerization reaction. The so obtain CNTs, covered by a polymeric layer could be really interesting for the preparation of composite material inside a polystyrene matrix. In this way the mechanical interaction between the CNSs and the polymer will be greatly enhanced. Further studies will also analyze the introduction of

other combination of functional groups, in order to obtain more complex, and sophisticated materials suitable for different applications.

2.3 Studies on the reaction of functionalization

As shown in this thesis, the chemical functionalization of CNSs is an efficient way to enhance their solubility, and to provide them useful functionalities. The addition of small organic moieties on the outer surface of the nanostructures can enhance the dispersability of the CNSs both thanks to specific interaction with the solvent, and to the aspecific steric hindrance. The Tour reaction is one of the most powerful method to obtain a good functionalization process. [13b]

Tour and Bahr in 2001, proposed the functionalization of CNTs based on the addition of aryl moieties thank to the decomposition of diazonium salts. These last reactive species were prepared, isolated as tetrafluoroborate, and after that let react with the nanomaterial at room temperature. The main problem with this procedure was the requirement to isolate the diazonium salts, that even if are more stable as tetrafluoroborate, are however a really reactive species that can be potentially explosive. To avoid this hazardous step it has been develop a synthesis that consist in the preparation *in situ* of the diazonium salt both in organic solvent with isopentylnitrite, and in water with sodium nitrite. [13b, c]

In aqueous environment the reaction pathway is well known and consist in the classic synthesis of a diazonium salt from the reaction between the corresponding aniline, and the sodium nitrite in acidic water. If in the solution are present CNSs, the formed salt can immediately react with them releasing nitrogen, and generating the aryl radical responsible of the addition.

It is believed that the reaction in organic environment follow a completely analogous pathway. Firstly the isopentylnitrite react with the aniline to form the diazonium salt which as before produce the aryl radical *in situ.*[78]

In figure 2-46 are illustrated the steps just described.

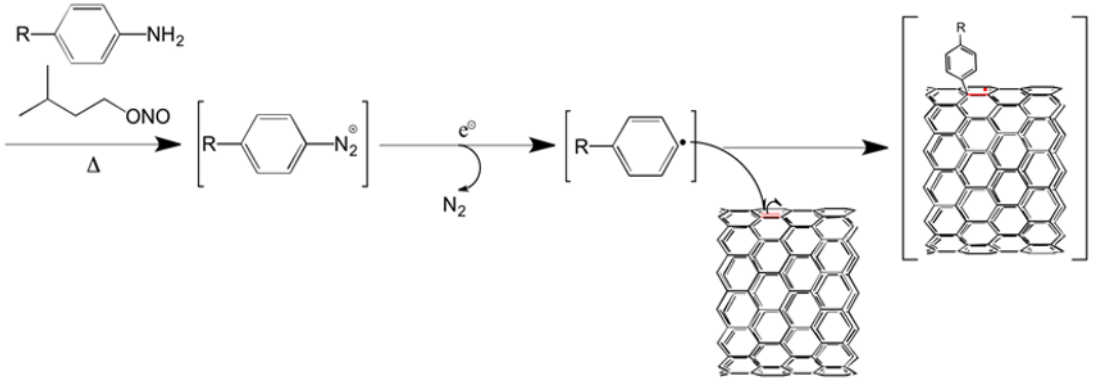

Figure 2-46: Tour reaction scheme.

Our research groups work a lot in the last years on the optimization of the reaction conditions of this reaction, working on MWCNTs in order to maximize their gain in solubility in common organic solvents. Our optimized procedure, used in almost all the reaction of this thesis, consist in the dispersion of the pristine CNSs in NCP through pulsed sonication. The reaction mixture is heated at 80 °C, and the aniline is added under magnetic stirring. At this point the isopentylnitrite is added, and the reaction is stopped after 15 minutes. To stop the reaction we add 10 volumes of methanol, that cause the precipitation of the functionalized CNSs. The final product is obtain through filtration.[22]

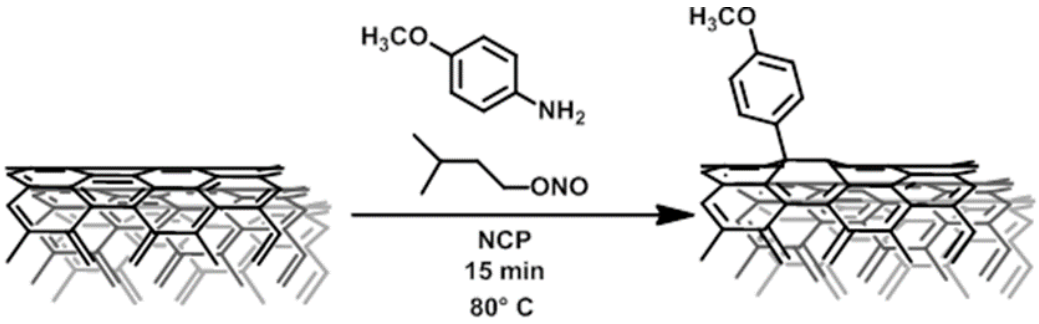

Figure 2-47: Scheme of functionalization of MWCNTs with 4-methoxyaniline.

In our studies, we noted that the efficiency of the reaction is strictly influenced by the temperature; in particular we demonstrated that in organic environment the reaction is much more slower if the temperature is under 80 °C. This fact is in some way difficult to explain looking at the reaction scheme described above. This temperature effect is so remarkable only with the synthesis "*in situ*" in organic environment; the one with the isolated diazonium salt is usually performed at a temperature of -20 / 0° C, indeed.

Looking at the scheme in figure 2-46 there are no solid explanation to this strong dependence over the reaction temperature. With this in mind, we performed a literature research based on reactions between anilines, and isopentylnitrite in organic solvents, and we found an interesting work published by William B. Smith and Oliver Chenpu Ho.[79]

2.3.1 **Through a more complex reaction scheme**

Smith and Ho, in 1990, published a paper in which they proved that it is possible to synthetize haloaryls from the reaction between the corresponding aniline and isopentylnitrite in a haloform.[79]

In figure 2-48, is presented the reaction pathway proposed by the authors.

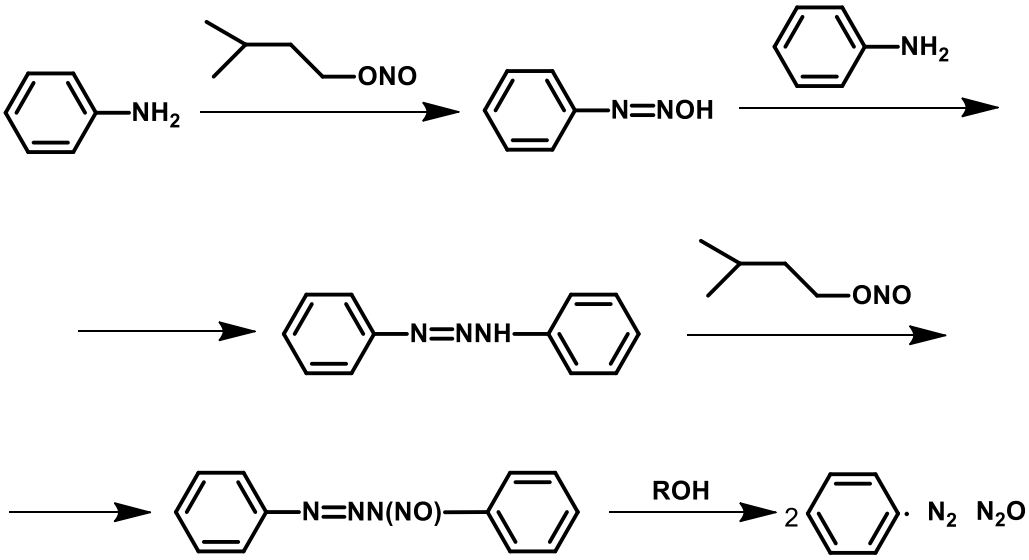

Figure 2-48: Reaction scheme reported by smith et all for the synthesis of haloaryls.[79]

In this article is reported that the reaction between the aniline and isopentyl nitrite take place also at room temperature, and bring to the formation of a diphenyltriazene that are enough stable to be isolated. They demonstrated that this species can react with a second equivalent of isopentylnitrite only at a temperature higher than 80 °C releasing two moles of aryl radicals. They also reported that diphenyltriazene is stable, even at temperatures higher than 80 °C, in absence of isopentylnitrite. In their synthesis the aryl radicals react immediately with the solvent to form the corresponding haloaryl.

There are many analogies between this case and our: the reactant and the stoichiometry are the same, the temperature found by Smith is the same that we found to be the best for the functionalization of CNTs, and in both the reaction at the end aryl radicals are formed. Starting from these considerations, we have hypothesized a possible reaction scheme characterized by a competition between two synthetic pathways: The “Tour” one, and the “Smith” one.

The general scheme hypothesized by us is shown in figure 2-49.

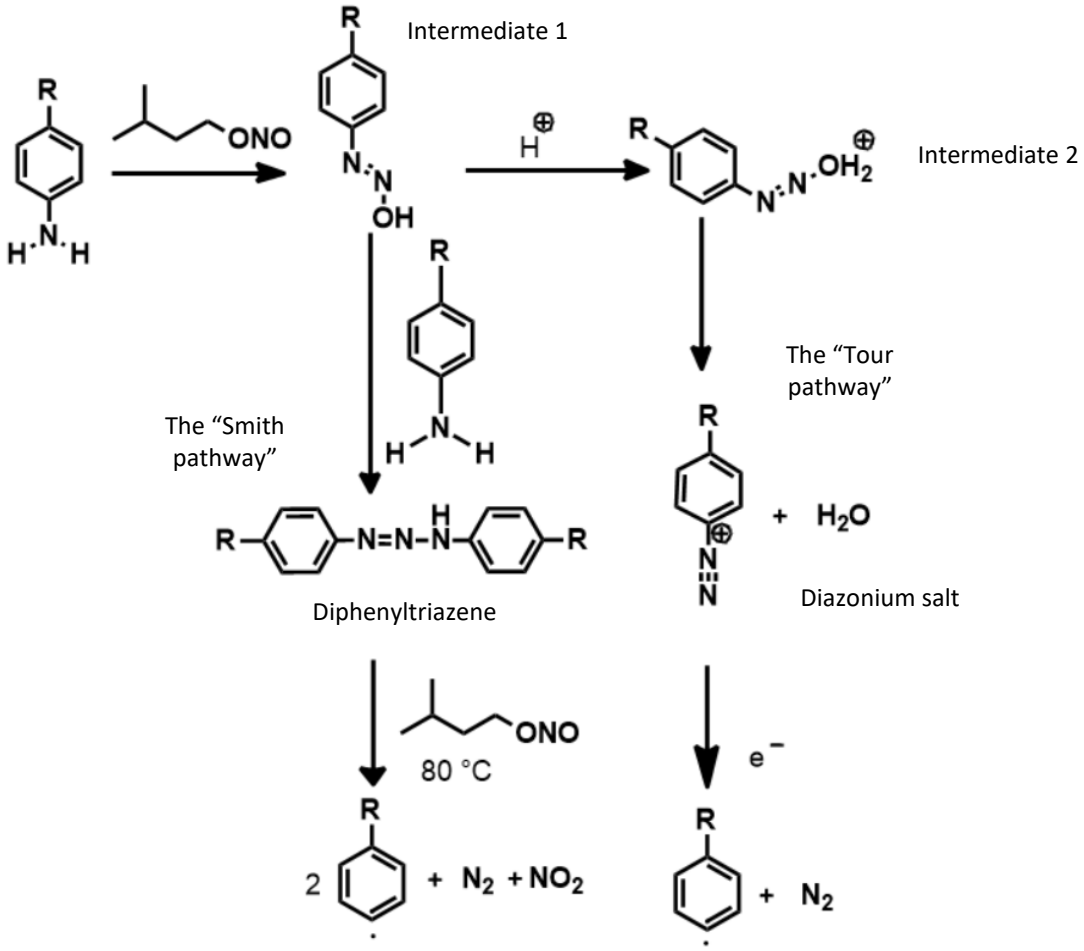

Figure 2-49: Our hypothesis of reaction scheme with two different pathways.

In our hypothesis, an aniline initially react with isopentylnitrite to form the intermediate 1. Indeed, this step is present in both the pathways. At this point if this intermediate 1 get protonated can form intermediate 2 that consequently bring to the formation of the diazonium salt, following the "Tour pathway".

If instead, the intermediate 1 do not get protonated can have the possibility to react with another equivalent of aniline to form the diphenyltriazene. At this point, the reaction can bring to the formation of the desired aryl radicals only at a temperature higher than 80° C and in the presence of isopentylnitrite ("Smith pathway").

Following this hypothesis the balance between the competition of the two different pathways will be controlled by the aforementioned protonation step, and so by the acidity or basicity of the reaction environment. To test our assumption we designed a chemical strategy to determine which intermediate (the diazonium salt or the diphenyltriazene) is formed in different acidic and basic environment. We studied the reaction between 4-methoxyaniline, and isopentylnitrite in the presence of N,N-dimethylaniline. This last species can react only with diazonium salts forming a stable

and isolable molecule. In this case it is 4-(dimetylamino)-4'-methoxyazobenzene, a diazo dye similar to dimethyl yellow. The reaction was performed in methanol in two different conditions: in one batch (R1) some drops of HCl_{aq} 1 M were added to the solution before the addition of isopentylnitrite, instead in the other (R2) some drops of $NaOH_{aq}$ 1 M were added.

If our hypothesis is true, the more acidic conditions of the reaction R1 should push the reaction through the "Tour pathway" and so to the formation of the diazonium salt and its consequent reaction with the dimethylaniline to form 4-(dimetylamino)-4'-methoxyazobenzene (P1). On the other hand the more basic conditions in R2 should bring to the formation of the diphenyltriazene (P2), leaving the dimethylaniline unreacted. This chemical strategy is presented in figure 2-50.

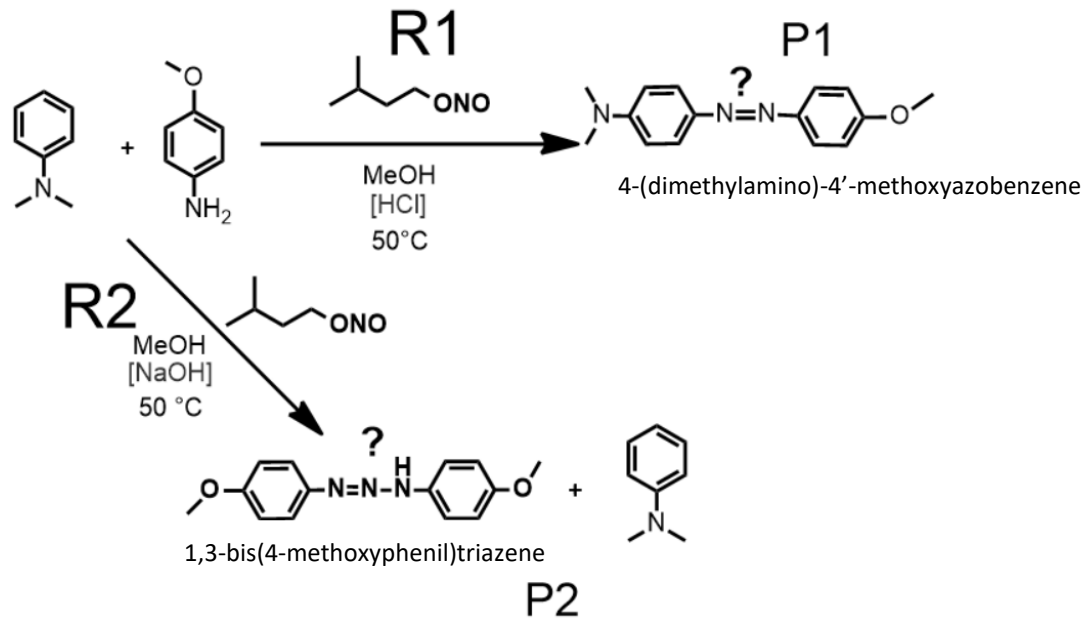

Figure 2-50: Scheme of the chemical strategy.

The two solutions were prepared as described above and let react at 50° C for 24 hours under magnetic stirring.

From a TLC analysis of the two reactions crude is evident that the two product are different as hypothesized. So we proceeded to the product isolation and characterization.

The product P1 obtained in the reaction R1 has been isolated through a sequence of chloroform and hexane extractions and characterized by ^{1}HNMR, and Uv-Vis absorption spectroscopy.

The Uv-Vis absorption spectrum of product P1 in ethanol is in good agreement with literature and present a peak at 405 nm, and a shoulder at 442 nm.[80] The ^{1}H-NMR spectrum in DMSO-d_6 reported in figure 2-51, presents the peaks of the 8 aromatic proton in the area between 8 and 6.5 ppm, and at 3.83 ppm the signal of the 3 methoxy protons. Finally at 3.05 ppm is visible the signal of the 6 methyl protons.

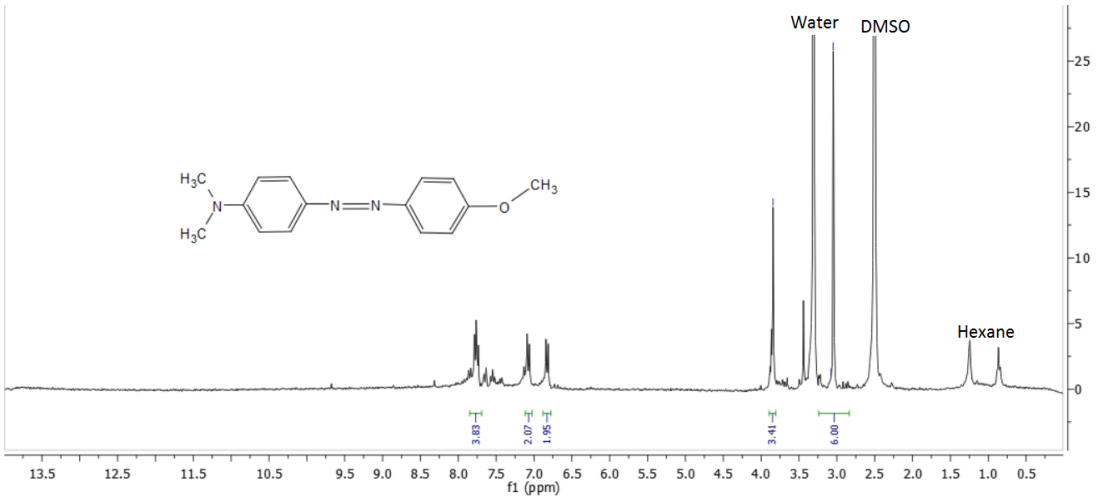

Figure 2-51: ^{1}H-NMR spectrum of P1 in DMSO-d_6.

The product P2 obtained in the reaction R2, instead, was treated with the same extraction procedure used for P1 and after that with a column chromatography, but it has been impossible to completely remove all the unreacted dimethylaniline. The product P2 has however been characterized by TLC, and Uv-Vis abortion spectroscopy.

So we proceed performing the reaction (R2*) in the same conditions as R2 but without the N,N-Dimethylaniline that in basic enviroment, in our hypothesis, should not participate to the reaction. The reaction crude has been extracted, and purified by column chromatography obtaining the product P2*. This product has been characterized by TLC, ^{1}HNMR, Uv-Vis, and FT-IR absorption spectroscopy.

From the TLC and Uv-Vis analysis is possible to state that product P2 and product P2* are the same species, confirming that the N,N-Dimethylaniline do not participate to reaction R2. The two products indeed, present the same Rf in the TLC, and moreover are characterized by the same absorption spectra presenting the characteristic peak at 356 nm.[81] Obviously in the characterizations of P2 is visible also the presence of the N,N-Dimethylaniline that was not completely remove.

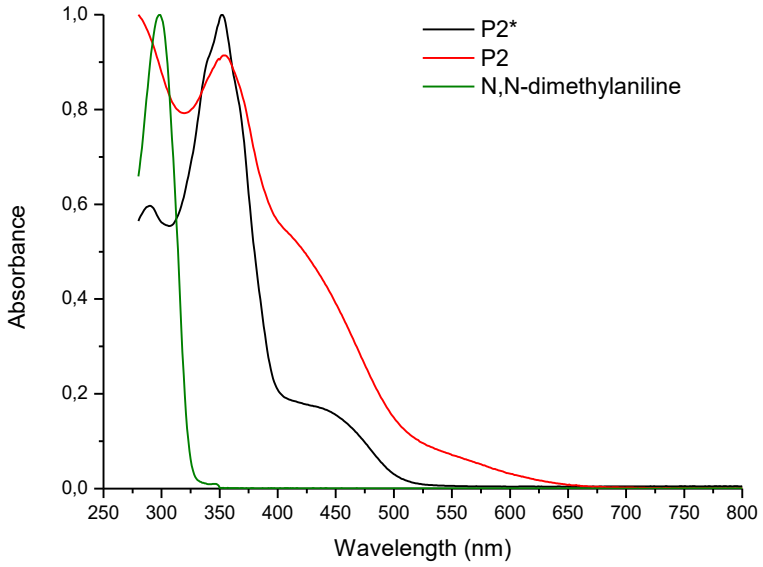

Figure 2-52: Superimposition of the Uv-Vis spectra of P2 (red curve), P2*(black curve) and N.N-Dimethylaniline (green curve) in cyclohexane.

In the Uv-Vis absorption spectrum of P2* in cyclohexane are clearly visible all the tree characteristic peak respectively at: 293 nm, 356 nm, and 440 nm.[81] Also the ^{1}H-NMR spectrum of P2* (in DMSO-d_6) presents all the expected peaks. The more characteristic is the one at 10.46 ppm relative to the triazene proton.[82]

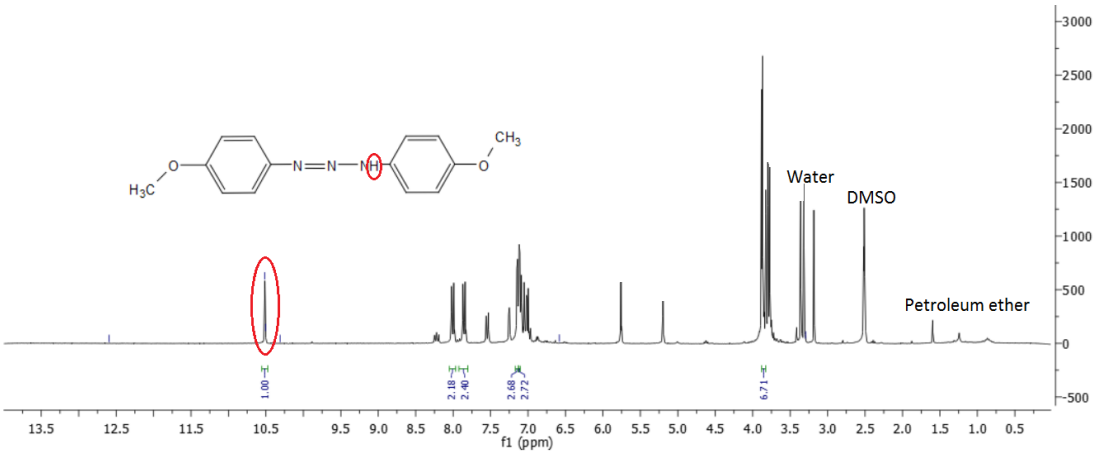

Figure 2-53: ^{1}H-NMR spectrum of P2* in DMSO-d_6.

In the FT-IR spectrum of the product P2* (figure 2-54) is present the peak at 1600 cm^{-1} that corresponds to the NH bending of the triazene group.[83]

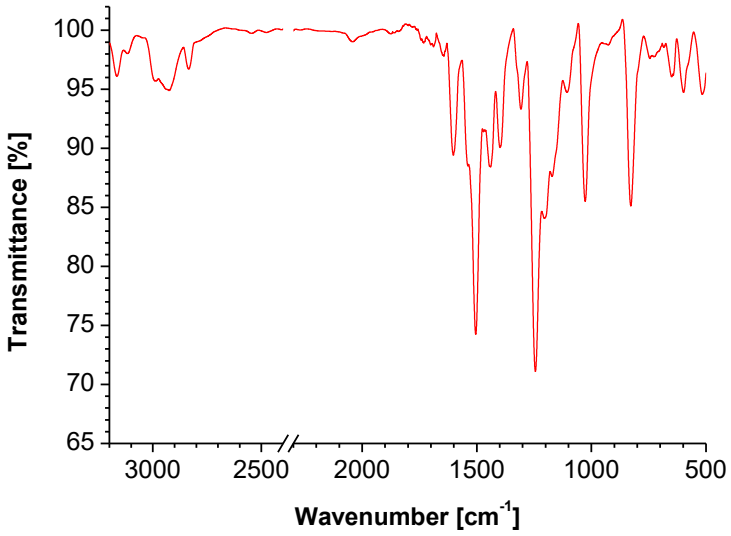

Figure 2-54: FT-IR spectrum in KBr of P2*.

With these tests we can state that the reaction between 4-methoxyaniline and isopentylnitrite in the presence of N,N-dimethylaniline bring to the formation of different product if is performed in different acidic and basic conditions. In particular, in more acidic conditions the product is 4-(dimethylamino)-4'-methoxyazobenzene, instead in more basic conditions the product is 1,3-bis(4-methoxyphenil)triazene and the N,N-dimethylaniline do not participate to the reaction. The fact that the product of R1 is that particular diazo compound tells us that during the reaction a diazonium salt is formed and so the pathway is mainly the "Tour" one. Instead obtaining the triazene from reaction R2 confirm Smith's results.

2.3.2 **CNSs functionalizations in different conditions**

Based on the results shown above we performed the functionalization of MWCNTs following our usual reaction protocol but in different acidic, and basic environment. The aim was to provide another proof to our hypothesis testing the effect on the functionalization efficiency in basic and acidic conditions.

We performed 4 functionalizations of MWCNTs in different environments: the "normal" one, the basic, the acidic, and a last one as control. All the reaction has been performed in NCP at 80 °C. For the acidic reaction some drops of HCl_{aq} 1 M were added to the NCP, for the basic one some drops of $NaOH_{aq}$ 1 M were added instead. As a control functionalization some drops of MilliQ water were added to the reaction mixture in order to verify that this addition do not interfere with the procedure. After the addition of the water solutions the reactions were performed as usual adding 0.5 equivalent of anisidine and after that 0.5 equivalent of isopentylnitrite. The

functionalized product were precipitated by the addition of 10 volumes of methanol, and then filtered, and washed.

In figure 2-55 are reported the resulting solubility in DMF of the functionalized MWCNTs obtain in each condition.

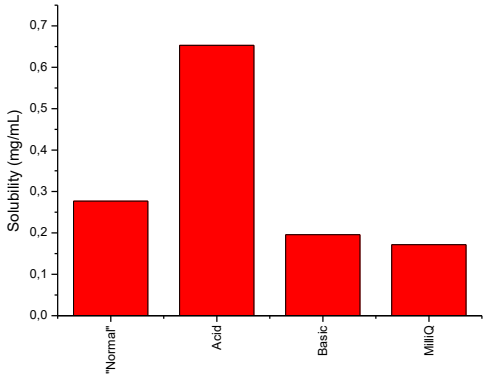

Figure 2-55: Solubility in DMF of the functionalized MWCNTs obtained in the 4 conditions.

From these results is evident that the addition of some drops of HCl_{aq} brings to a more efficient functionalization that provide a more soluble nanostructure. The reaction in which were added some drops of $NaOH_{aq}$ or MilliQ water results instead in nanotubes almost as soluble as the “normal” ones.

Also from the TGA analysis of these products is evident the big effect on the functionalization efficiency due to the acidic environment. Indeed, the functionalization degree (FD) of MWCNTs functionalized in the normal condition is 1/90, and the one for the nanotubes functionalized in acidic condition is 1/32. This means that onto this last product there are almost three times more functional groups than on the others.

It is therefore considered that the greater functionalization efficiency obtained in acidic conditions is the result of having forced the reaction through the “Tour pathway”. In this way, forcing the reaction to the formation of diazonium salts the functionalization is faster because these species are more reactive than the triazenes.

2.4 Conclusions

In this work functionalized-CNS@PLLA composites were thoroughly characterized in their thin film forms by assessing the variation in thermal, mechanical and, electrical properties as a function of CNSs loading over a range between 0.1 wt% and 5 wt%. The good quality of the CNS nanofillers dispersion within the polymer phase was stated, particularly for the MWCNT-based samples, for which an almost linear trend was found in the decrease of the crystallization temperature of the polymer as a function of the increased filler concentration.

The mechanical properties were found to be highly influenced by the presence of the 4-methoxyphenyl functional groups covalently bound to the CNSs surfaces, which confer to the functionalized fillers an unusual character of plasticizing agents rather than of reinforcing ones. The ductility of the composites is extremely improved with respect to bare PLLA for concentrations of CNSs around 0.5-1 wt%, even though for RGO-based samples the limits to obtain an improved plasticity are lower than for MWCNT and CNH-based samples, with the 5 wt% concentration already too high to furnish a durable material.

Electrical percolation in the composites was found to take place only with MWCNTs and RGO fillers, within the range of concentrations considered. Thresholds were differently located for the two cases, with the MWCNT-PhOMe@PLLA composites showing a sharp increase in conductivity at a lower CNSs concentration with respect to RGO-PhOMe@PLLA. The extent of conductivity after the percolation threshold was also significantly higher for the former as compared to the latter. A strong influence of the filler dimensionality on the electrical behavior of the composite is evident: monodimensional CNSs like MWCNTs are able to arrange in conductive domains within polymer chains much more effectively than bidimensional CNSs like RGO. Finally, zero-dimensional species such as CNHs likely require high concentrations to give rise to conductive pathways within an insulating matrix. The superior ability of CNTs to form conductive networks over a long distance is further confirmed by the CAFM data obtained on both film surfaces and along single nanofibers. Particularly for these last ones, a measurable current could be detected only for CNTs-based samples. This aspect of being able to originate long range percolation pathways along one single direction might be promising to provide next scaffold design with a selective guidance to neurites elongation.

Biocompatibility and bioactivity of our material were tested, confirming good properties for neural growth and differentiation. Neurons growing on our substrates tend to develop an higher number of longer neurites. Effect on the differentiation of

stem cell were also tested with the material containing 0.25% of MWCNTs. Our results here suggest an interesting effects on cell differentiation through neuronal lineage.

Starting from our results obtained on the biocompatibility of our materials we designed and obtained our first prototypes of nerve conduits, that we are now testing as implant in *in-vivo* operation on sciatic nerve of mice. Our preliminary results obtained on the first 10 animals are really promising in term or nerve regeneration, function restoration and inflammatory response.

In this work we proposed three different chemical modifications of MWCNTs performed by Tour reaction. The addition of *p*-carboxyphenyl groups afforded to MWCNT-PhCOOH with solubility as high as 0.31 *mg/mL* in water, while the unmodified nanostructure is not soluble. The presence of the carboxylic functionalities has been validated, not yet quantitatively, by XPS measurements and by studying pH-dependent solubility.

The amide coupling of a paramagnetic spin labeled molecules proved not only the presence of the carboxylic functionality but also its chemical availability for additional reactions. The controlled introduction of carboxylic functionalities on CNTs via Tour reaction is a valid alternative to the oxidation of the CNSs widely used in the literature at the moment. It allows a better control over the degree of functionalization, the selective introduction of the carboxylic functionality, and a higher overall quality of the product due to a lower extent of damages introduced by the reaction.

The addition of 4-methoxyphenyl groups resulted to be a reliable way to increase the solubility of functionalized -MWCNTs in DMF as demonstrated in previous studies. The possibility of taking advantage of this property has been demonstrated also when the 4-methoxyphenyl groups were added in combination with *p*-vinylphenyl functionalities. Making use of the vinyl functionality we were able to perform an *in-situ* polymerization on the co-functionalized MWCNT, and the cooperative work of the introduced functional groups resulted in an overall better decoration of the CNTs. TEM measurements show a polymeric coating on the *CNSs* which is absent when the polymerization is performed on un-modified MWCNTs. The influence of a covalent bond between polymer and nanofiller is not yet assessed, but future studies are in program to rigorously describe the relation.

Finally we start to analyze the reaction scheme of the Tour functionalization of CNSs, and we hypothesized that this process could be a balance between two different reaction pathways. We performed the reaction between an aniline and isopentylnitrite in the presence of N,N-dimethylaniline in different acidic and basic conditions obtaining different products. We also demonstrated that the functionalization of MWCNTs is more efficient in acidic condition, giving another proof to our hypothesis.

3 Experimental part

3.1 Solvents, reagents and starting materials

Commercial solvents and reagents are reported in Tables. Solvents and reagents were used without any further purification, unless specified.

Solvent	*MW [g/mol]*	*d [g/mL]*	*b.p. [°C]*	*Seller*
DMF	73.10	0.948	153 − 155	Sigma-Aldrich
Methanol	32.04	0.791	64.7	Sigma-Aldrich
Ethanol	46.06	0.789	78	Sigma-Aldrich
Ethyl acetate	88.11	0.901	77	Sigma-Aldrich
NCP	167.13	1.007	330	Sigma-Aldrich
THF	72.11	0.890	65 − 67	Sigma-Aldrich
Chloroform	119.38	1.492	60.5 − 61.5	Sigma-Aldrich
Dichloromethane	84.93	1.33	40	Sigma-Aldrich

Reagent	*MW [g/mol]*	*d [g/mL]*	*b.p. [°C]*	*Seller*
HCl (37%)	36.46	1.2	/	Sigma-Aldrich
4-methoxyaniline	123.15	/	240 − 243	Sigma-Aldrich
P-aminobenzoic acid	137.14	1.374	/	Sigma-Aldrich
4-vinylaniline	119.16	1.017	213 − 214	Sigma-Aldrich
Isopentylnitrite	117.15	0.872	99	Sigma-Aldrich
HBTU	379.24	/	/	Sigma-Aldrich
NHS	115.09	/	/	Sigma-Aldrich
EDC · HCl	191.70	/	/	Sigma-Aldrich
DIPEA	129.24	0.742	127	Sigma-Aldrich
4-amino-TEMPO	171.26	/	/	Sigma-Aldrich
Styrene	104.15	0.906	145 − 146	Sigma-Aldrich
Benzoyl peroxide	242.23	/	/	Fluka

CNSs	*Number of layers*	*Dimension*		*Seller*
MWCNTs	30	Length 3-6 (µm)	Diameter 4-5 (nm)	SouthWest NanoTechnologies
CNHs	1	Length 30-50 (nm)	Diameter 2-5 (nm)	Carbonium
RGO	5	Length 1 (µm)	Width 1(µm)	ACS

Polymer	*Averaged molecular weight (kg/mol)*	*Percentage of D residues*	*Density (g/cm^3)*	*Seller*
PLLA	5200	1.1-1.7	1.25	Unitika Co. Ltd. (Osaka, Japan).

3.2 Instruments and analytical procedures

3.2.1 **UV-Vis-NIR spectroscopy**

Uv-Visible spectra were acquired with a Varian Cary 5000 spectrometer, at room temperature, between 280 and 1500 nm, with interval 0.5 nm, scan speed 300 nm/min and spectral bandwidth 2 nm. Quartz cuvettes with 1 cm optical path were used for the measurements.

3.2.2 **FT-IR spectroscopy**

FT-IR spectra were acquired in a window between 4000 and 400 cm^{-1}. Transmission measurements were performed on a FT-IR Nicolet 5700 spectrometer.

3.2.3 **Raman spectroscopy**

Raman spectra were acquired with a Renishaw spectrometer equipped with 50x and 25x lenses, and low energy laser source (Physics 150m, Elio-Neon 633 nm). The samples are tested on glass slides (Corning).

3.2.4 **Thermogravimetric analysis**

TGA measurements were carried on a TGA Q5000IR (TA instruments). The analysis were performed with a 10◦C/min ramp from 100◦C to 1000◦C.

3.2.5 **Transmission electron microscopy**

TEM images were acquired with a Tecnai 12 (FEI) microscope at the Electronic Microscopy Service from the Biology Department of the University of Padova.

3.2.6 **Microtip sonication**

The dispersion of the nanostructures was performed with a Titanium tip Misonix 3000 sonicator. The sonication was performed with a 3s ON - 3s OFF period at power level 2.0 (4 − 6 Watt). The time was varied according to the specific procedure.

3.2.7 **Centrifugation**

The centrifugation was performed on a MR23i jouan (Thermo Scientific) centrifuge equipped with a variable angle rotor (model 11174711/11174720). 10 mL, conical bottom, Duran glass centrifuge tubes were used for the centrifugation procedures.

3.2.8 **Electron paramagnetic resonance spectroscopy**

All EPR measurements were performed in collaboration with Prof. Lorenzo Franco from the Chemical Sciences Department of the University of Padova.

3.2.9 **AFM measurements**

All the AFM analysis were performed in collaboration with Dr. M. Salerno from the IIT of Genova. The AFM images were 256 × 256 pixels and were acquired on an MFP-3D instrument (Asylum Research, US) in ambient air. For the conductive AFM (CAFM) measurements, a probe of type AC240TM-R3 (Olympus, Japan) was employed, with cantilever resonance frequency of 66.62 kHz and spring constant of 1.81 N/m. The tip had a Ti/Pt coating of ~20 nm thickness, and thus an effective apex diameter of ~60 nm. Further technical details about the CAFM measurements are reported in the Supplementary Data, for the sake of space. For SKPM a probe of type PPP-EFM (Nanosensors, Switzerland) was used, with resonance frequency of 95.90 kHz. The tip has a Ti/PtIr5 coating of ~25 nm thickness, and thus an effective apex diameter of ~70 nm. The AFM was operated in lift (Nap) mode, with Tapping tracking of the topography during the first pass, and at an elevation of 100 nm during the second pass. During the latter pass, a feedback was applied on the tip voltage, a sum of AC and DC components, such that the electrical force between tip and sample (set at virtual ground) was canceled out. In some cases, to provide better understanding of the electrical surface properties, the analysis was switched from SKPM to qualitative EFM mode. While this is also based on two-pass technique, during the second pass the cantilever is dithered mechanically and the open-loop changes in oscillation phase are observed. On average, lower local phase lags of the oscillating cantilever should correspond to net repulsive forces, while higher local phase lags should correspond to attractive forces. For the roughness measurements, Tapping mode AFM was carried out with a probe of type SSS-NCHR (Nanosensors, Switzerland), with cantilever resonance frequency of ~312.53 kHz. The most important amplitude parameter of surface roughness, namely 2-D root mean square (RMS) S_q has been extracted from the height distributions in the images, and averaged over all the images (N≥5).

3.2.10 **Biological method**

All the biological analysis were performed in collaboration with the research group of Prof. F. Filippini, and in particular with Yuriko S. Hernandez Gomez, from the department of biological science of the University of Padova. Exponential growing human neuroblastoma cells line SH-SY5Y [84] were cultured with Dulbecco's Modified Eagle Medium/Nutrient Mixture F-12 (DMEM/F-12) GlutaMAX™ supplement (Invitrogen) supplemented with 10% heat-inactivated fetal bovine serum (FBS, Euroclone) and 25μg/ml of gentamicin (growth medium), in a humidified atmosphere of 5% of CO_2 in air at 37 °C. Cells were subcultured - 900000 into 25 cm² flasks (Sarstedt)

- every 2 days (i.e. at 90% confluence approximately). In control, scaffold-free samples, cells were seeded in a 24-well plate (15000 cells/well) coated with a gelatine (porcine skin 0.005% in H_2O milliQ)/poly-L-lysine (Invitrogen, 1mg/ml) solution. Poly-L-lysine is widely used as a good substrate for neural cell adhesion and growth. PLLA and CNS@PLLA films were cut into round slices with 13 mm diameter for well positioning into 24-well plates. After sterilization by UV irradiation, the films were incubated for 24h in growth medium and then cells (15000/well) were seeded onto their surfaces. Cell death and proliferation were assessed at day 0 (24 h after cell seeding) and day 2 (72 h after cell seeding).

3.3 Synthesis an characterizations

3.3.1 **Functionalization of MWCNTs with *4*-methoxyaniline**

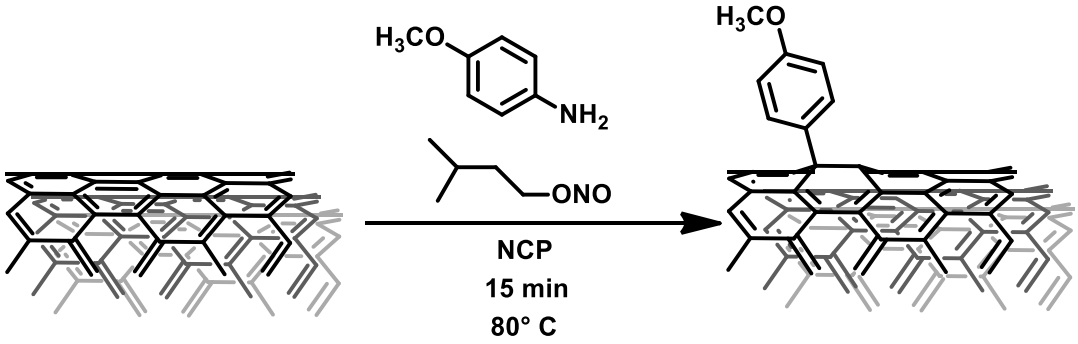

Reagent	***PM*** *[g/mol]*	***Weight*** *[mg]*	***Volume*** *[mL]*	***Moles*** *[mmol]*
MWCNTs	12.01[a]	225.0	/	18.73
4-methoxyaniline	123.15	1155.0	/	9.38
Isopentyl nitrite	117.15	1098.7	1.260	9.37
NCP (solvent)	167.25	/	150	/

[a] Moles calculated from the atomic weight of carbon, considering MWCNTs exclusively made of sp2 carbon.

The functionalization has been divided in 3 batches, all the conditions were the same as follow.

For each batch, the MWCNTs (75 mg, 6.25 mmol of C) were dispersed in NCP (35.0 mL) by pulsed microtip sonication for 10 minutes. (intensity 6W and interval 3s ON 3s OFF)

4-methoxyaniline (385.3 mg, 3.13 mmol, 0.5 eq) dissolved in NCP (15 mL) were added to this dispersion. The reaction mixture were heated at 80° C under nitrogen reflux. Once the temperature were reached isopentylnitrite (0.420 mL, 3.12 mmol) were added. The reaction went for 15 minutes under stirring and nitrogen reflux at 80° C. 500 mL of cold methanol were added to the crude of reaction and the dispersion was filtered on a Fluoropore 0.2µm membrane. The product were washed on the filter 4 times, each with 200 mL of methanol. The functionalized MWCNTs on the filters were dried in air.

A small amount of the product were extracted in DMF and characterized. The extraction procedure consist in the dispersion by pulsed microtip sonication for 1 minute (intensity 6W and interval 3s ON 3s OFF) followed by centrifugation (3500 rpm, 5 min, 20 °C). The so obtained solution have been characterized by Uv-vis, DLS, Raman and the concentration has been evaluated by TGA.

Solubility in DMF (mg/mL): 0.31

Raman [cm^{-1}](relative intensities): 1330 (1,61), 1607 (1), 2644 (0,20)

D/G ratio (from Raman spectra): 1.61

FD (weight loss at 500 °C, air): in DMF 1/90 (9,01%)

DLS in DMF (solvodynamic mean diameter): 25.6 nm

Combustion flex temperature (from TGA thermogram): 630.1 °C

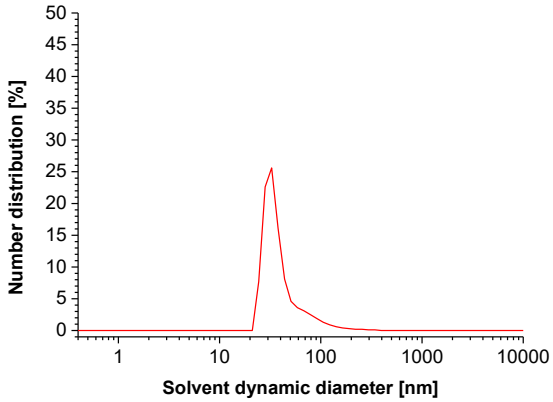

Figure 3-1:DLS Of the product MWCNT-PhOMe in DMF.

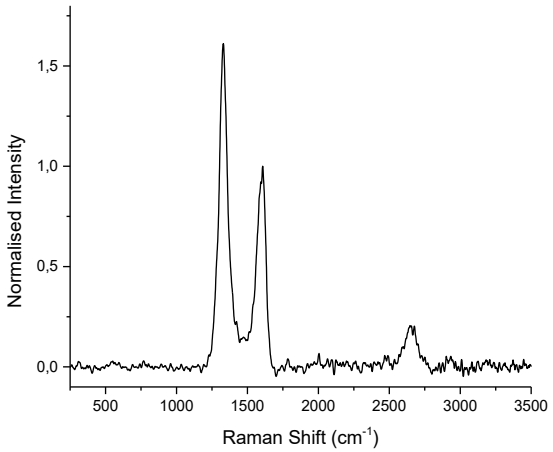

Figure 3-2: Raman spectrum of the product MWCNT-PhOMe.

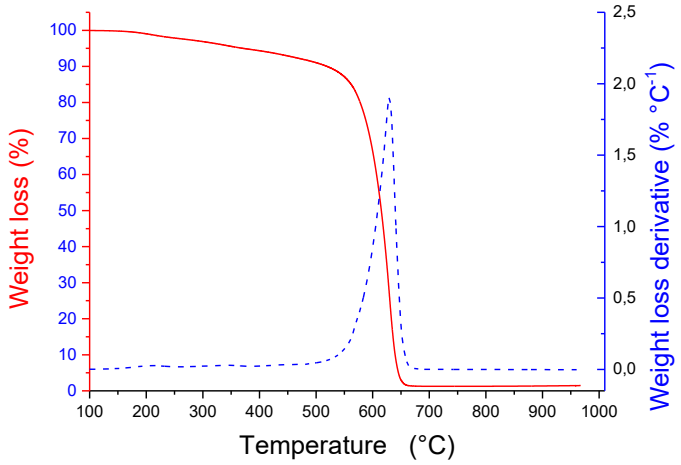

Figure 3-3: TGA of the product MWCNT-PhOMe in air (heating rate 10 °C min^{-1}).

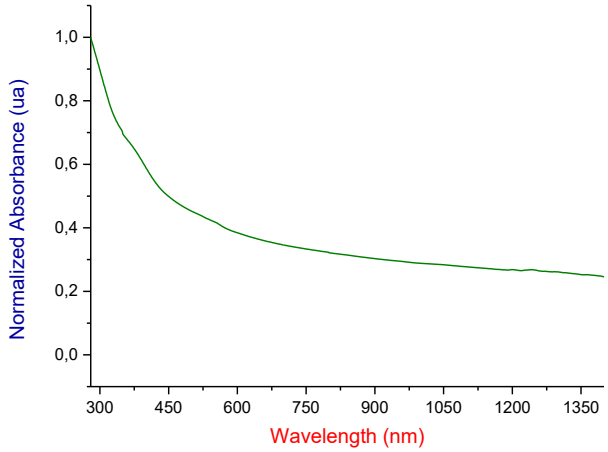

Figure 3-4: Uv-vis-NIR spectrum of the product MWCNT-PhOMe in DMF.

3.3.2 **Functionalization of CNHs with 4-methoxyaniline**

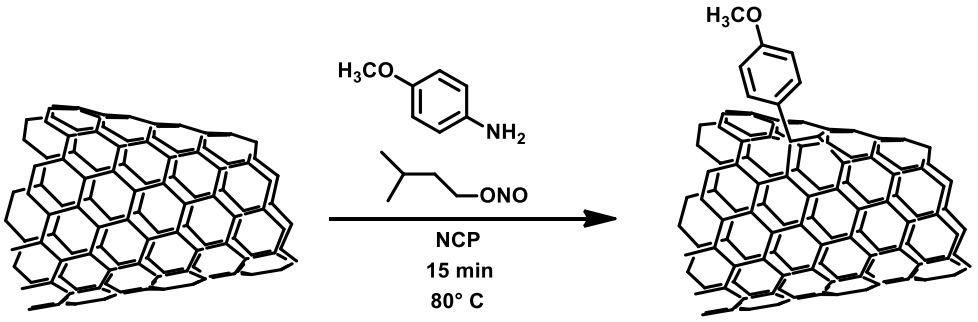

Reagent	***PM*** *[g/mol]*	***Weight*** *[mg]*	***Volume*** *[mL]*	***Moles*** *[mmol]*
CNHs	12.01[a]	225.0	/	18.75
4-methoxyaniline	123.15	2310.3	/	18.76
Isopentyl nitrite	117.15	2194.8	2.517	18.73
NCP (solvent)	167.25	/	150	/

[a] Moles calculated from the atomic weight of carbon, considering MWCNTs exclusively made of sp2 carbon.

The functionalization has been divided in 3 batches, all the conditions were the same as follow.

For each batch, the CNHs (75 mg, 6.25 mmol of C) were dispersed in NCP (35.0 mL) by pulsed microtip sonication for 10 minutes. (intensity 6W and interval 3s ON 3s OFF)

4-methoxyaniline (770.1 mg, 6.25 mmol, 1 eq) dissolved in NCP (15 mL) were added to this dispersion. The reaction mixture were heated at 80° C under nitrogen reflux. Once the temperature were reached isopentylnitrite (0.839 mL, 6.25 mmol) were added. The reaction went for 15 minutes under stirring and nitrogen reflux at 80° C. 500 mL of cold methanol were added to the crude of reaction and the dispersion was filtered on a Fluoropore 0.2µm membrane. The product were washed on the filter 4 times, each with 200 mL of methanol. The functionalized CNHs on the filters were dried in air.

A small amount of the product were extracted in DMF and characterized. The extraction procedure consist in the dispersion by pulsed microtip sonication for 1 minute (intensity 6W and interval 3s ON 3s OFF) followed by centrifugation (3500 rpm, 5 min, 20 °C). The so obtained solution have been characterized by Uv-vis, DLS, Raman and the concentration has been evaluated by TGA.

Solubility in DMF (mg/mL): 1.31

Raman [cm^{-1}](relative intensity): 1323 (1,09), 1597 (1), 2615 (0,15)

D/G ratio (from Raman spectra): 1.09

FD (weight loss at 500°C, air): in DMF 1/34 (20,75%)

DLS in DMF (solvodynamico mean diameter): 86 nm

Combustion flex temperature (from TGA thermogram): 660.2 °C

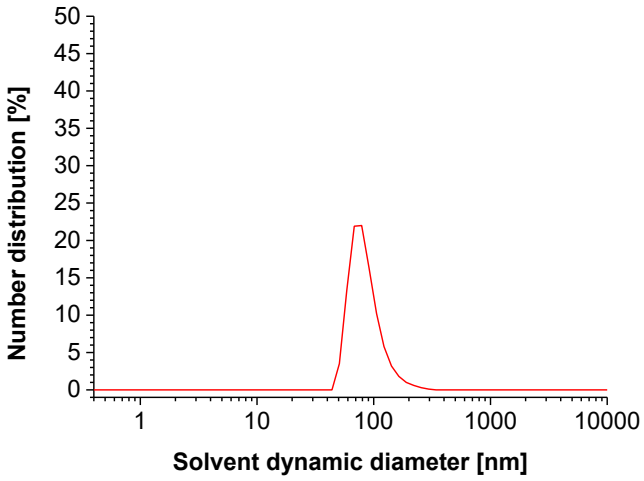

Figure 3-5: DLS Of the product CNH-PhOMe in DMF.

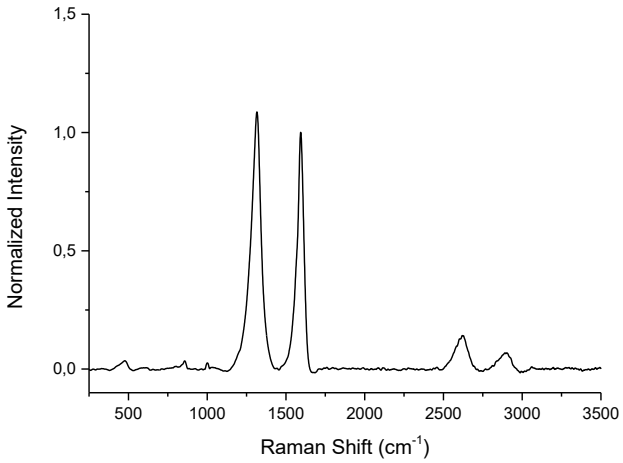

Figure 3-6: Raman spectrum of the product CNH-PhOMe.

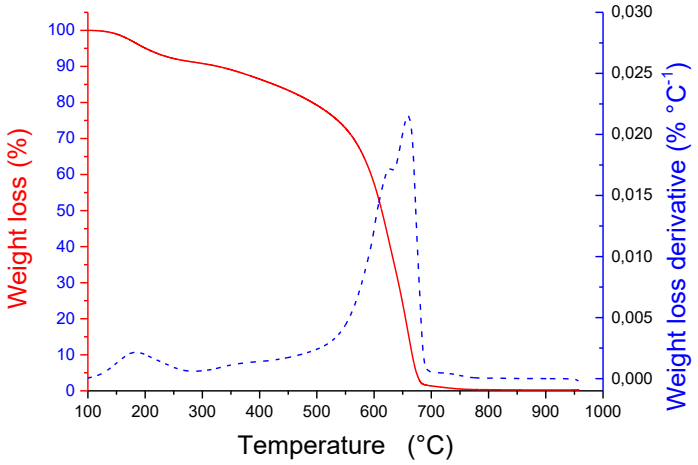

Figure 3-7: TGA of the product CNH-PhOMe in air (heating rate 10 °C min^{-1}).

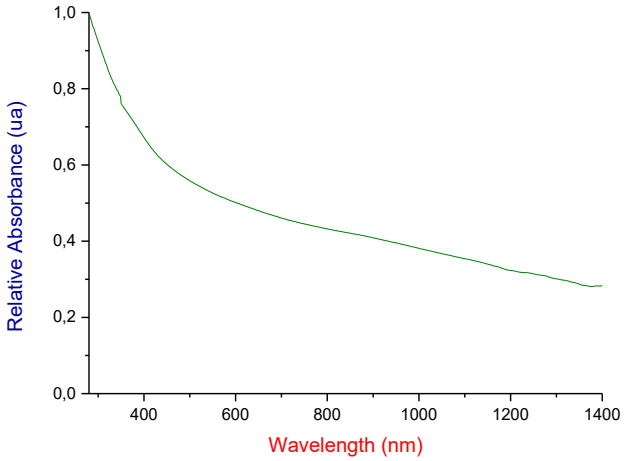

Figure 3-8: Uv-vis-NIR spectrum of the product CNH-PhOMe in DMF.

3.3.3 **Functionalization of RGO with 4-methoxyaniline**

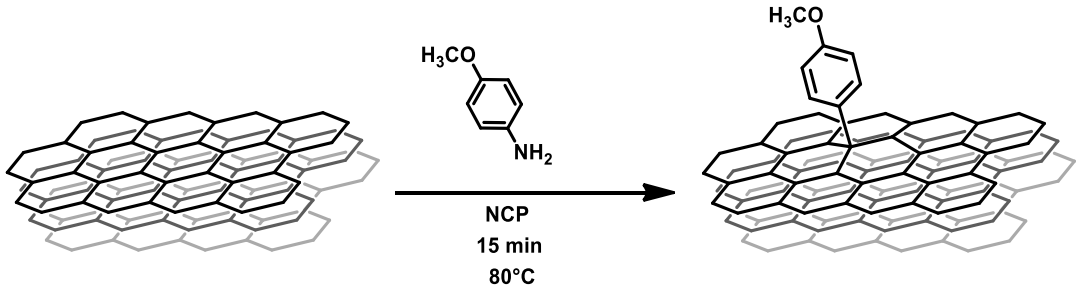

Reagent	***PM*** *[g/mol]*	***Weight*** *[mg]*	***Volume*** *[mL]*	***Moles*** *[mmol]*
RGO	12.01[a]	150.0	/	12.49
4-methoxyaniline	123.15	769.7	/	6.25
Isopentilnitrito	117.15	732.5	840	6.25
NCP (solvent)	167.25	/	120	/

[a] Moles calculated from the atomic weight of carbon, considering MWCNTs exclusively made of sp2 carbon.

The functionalization has been divided in 3 batches, all the conditions were the same as follow.

For each batch, the RGO (50 mg, 4.16 mmol di C) were dispersed in NCP (30.0 mL) by pulsed microtip sonication for 10 minutes. (intensity 6W and interval 3s ON 3s OFF)

4-methoxyaniline (256.6. mg, 2.08 mmol, 0,5 eq) dissolved in NCP (10 mL) were added to this dispersion. The reaction mixture were heated at 80° C under nitrogen reflux. Once the temperature were reached isopentylnitrite (0.280 mL, 2.08 mmol) were added. The reaction went for 15 minutes under stirring and nitrogen reflux at 80° C. 400 mL of cold methanol were added to the crude of reaction and the dispersion was filtered on a Fluoropore 0.2µm membrane. The product were washed on the filter 4 times, each with 150 mL of methanol. The functionalized RGO on the filters were dried in air.

A small amount of the product were extracted in DMF and characterized. The extraction procedure consist in the dispersion by pulsed microtip sonication for 1 minute (intensity 6W and interval 3s ON 3s OFF) followed by centrifugation (3500 rpm, 5 min, 20 °C). The so obtained solution have been characterized by Uv-vis, DLS, Raman and the concentration has been evaluated by TGA.

Solubility in DMF (mg/mL): 0.50

Raman [cm^{-1}](relative intensity): 1329 (0,90), 1591 (1), 2627 (0,05)

D/G ratio (from Raman spectra): 0,90

FD (weight loss at 500 °C, air): in DMF 1/33 (21,10 %)

DLS (solvodynamic mean diameter): 164 nm

Combustion flex temperature (from TGA thermogram): 600.4 °C

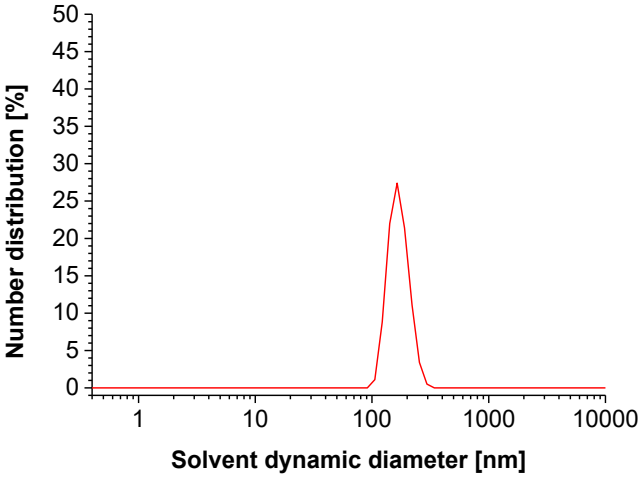

Figure 3-9: DLS Of the product RGO-PhOMe in DMF.

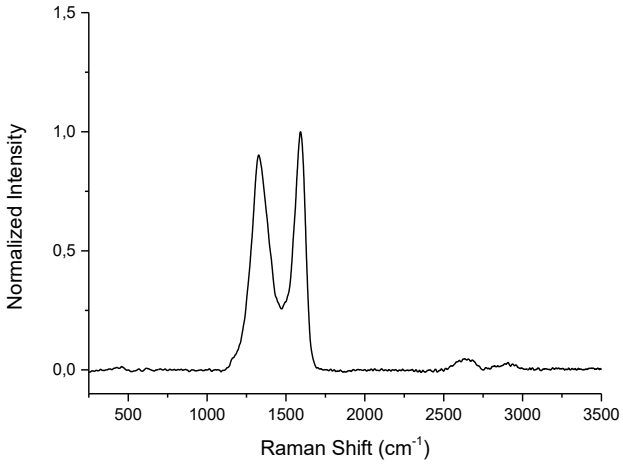

Figure 3-10: Raman spectrum of the product RGO-PhOMe.

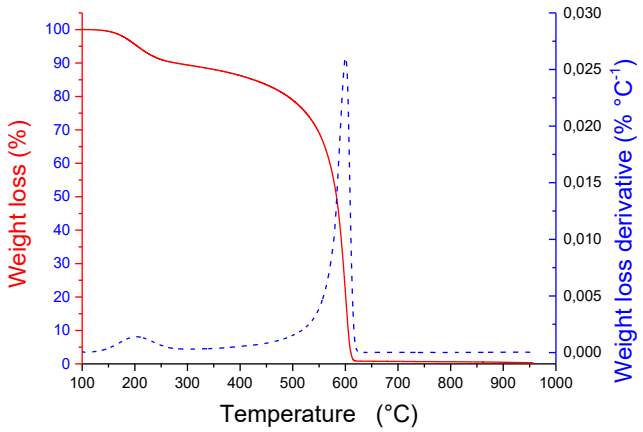

Figure 3-11: TGA of the product MWCNT-PhOMe in air (heating rate 10 °C min^{-1}).

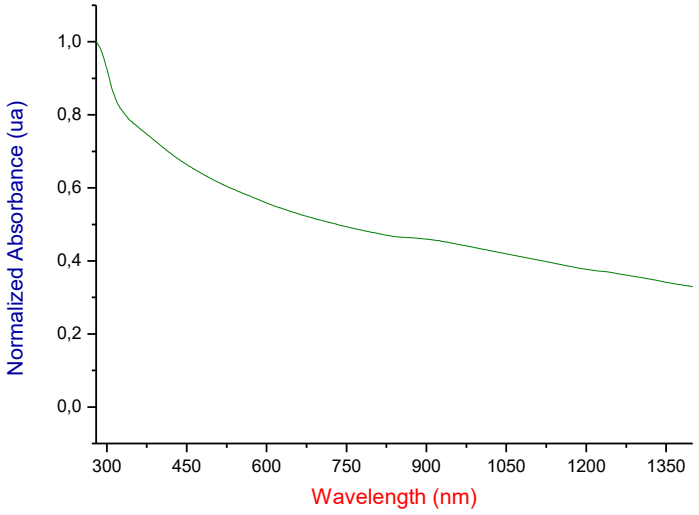

Figure 3-12: Uv-vis-NIR spectrum of the product CNH-PhOMe in DMF.

3.3.4 **Preparation of CNS-PhOMe@PLLA films composite materials**

3.3.4.1 Preparation of MWCNT-PhOMe@PLLA composite materials

MWCNT-PhOMe content	***MWCNT-PhOME***	***PLLA***	***Chloroform***
[% p/p]	[mg]	[g]	[g]
0,1	2,52	2,52	42
0,25	6,30	2,52	42
0,5	12,60	2,52	42
1	25,20	2,52	42
5	126,00	2,52	42

The product MWCNT-PhOMe obtained from the reaction described above were divided in 5 different batches (see table for detailed quantities) and dispersed in chloroform (42 g) by bath sonication for 30 minutes.

PLLA (2.52 g) were added at the dispersion and let dissolve for one day under stirring.

The composite material solution so obtained were poured into a glass Petri dish (diameter 5.75 cm) and put in a preheated hoven at 50 °C. After 5 hours, the dried product were removed from the Petri dish as a freestanding film.

The material were characterized by TGA, DSC, Uv-vis and Raman. Also the electrical resistance of the material were measured. After that the films were cut into small speciments (4 cm x 1 cm) for the Stress-Strain mechanical characterizations.

Figure 3-13: Images of the five types of MWCNT-PhOMe@PLLA composites having different concentrations of nanofillers in the polymer phase.

DSC analysis of MWCNT@PLLA

	1st melting peak			***1st crystallization peak***		
CNS content *(% w/w)*	**Tmax** (°C)	**Tonset** (°C)	**ΔH** (J/g)	**Tmax** (°C)	**Tonset** (°C)	**ΔH** (J/g)
0,1	154,71	150,60	25,70	111,30	99,60	-23,43
0,25	154,95	150,50	23,47	110,30	98,32	-22,55
0,5	154,96	150,06	25,11	107,78	97,98	-20,74
1	154,97	149,73	22,62	103,50	94,14	-18,28
5	154,76	148,99	24,09	101,87	92,33	-16,90

	2nd melting peak				
CNS content *(% w/w)*	**Tmax** (°C)	**Tonset** (°C)	**ΔH** (J/g)	**Tg** (°C)	**Crystallinity (1st peak)** (%)
0,1	155,17	151,60	23,50	56,56	27,2
0,25	155,38	151,38	22,67	56,61	25,3
0,5	155,12	151,44	22,91	56,43	26,3
1	149,90	150,81	20,76	56,16	24,3
5	151,50	150,12	21,63	56,12	25,9

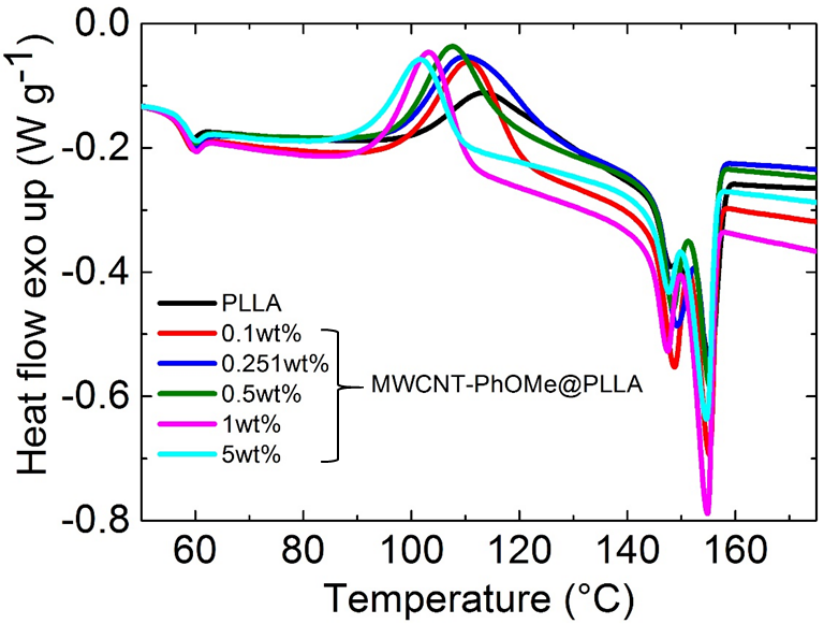

Figure 3-14: DSC traces for the five types of MWCNT-PhOMe@PLLA composites having different concentrations of nanofillers in the polymer phase and for pure PLLA.

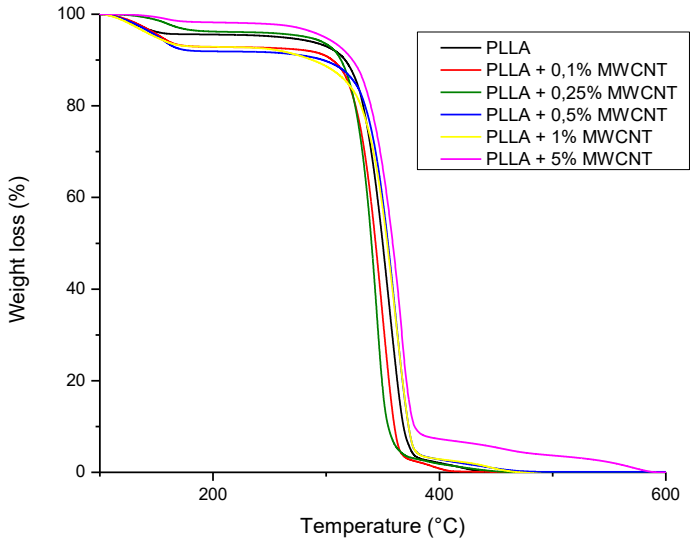

Figure 3-15: TGA for the MWCNT-PhOMe@PLLA composites having different concentrations of nanofillers in the polymer phase and for pure PLLA.

Stress/Strain analysis of MWCNT@PLLA

Conc.	***Young modulus***	***Tenacity***	***Stress Snerv.***	***Defor. Snerv***	***Def. Max.***	***Stress break***
(% w/w)	(MPa)	(Mpa)	(Mpa)	(%)	(%)	(Mpa)
0,1	745,4	33,9	25,6	13,0	149,5	0,2
0,25	741,0	41,6	23,8	6,6	204,5	0,3
0,5	699,1	46,0	23,9	9,2	219,5	0,2
1	587,0	35,5	22,6	15,9	171,7	0,2
5	782,0	7,1	28,5	13,0	29,1	0,2

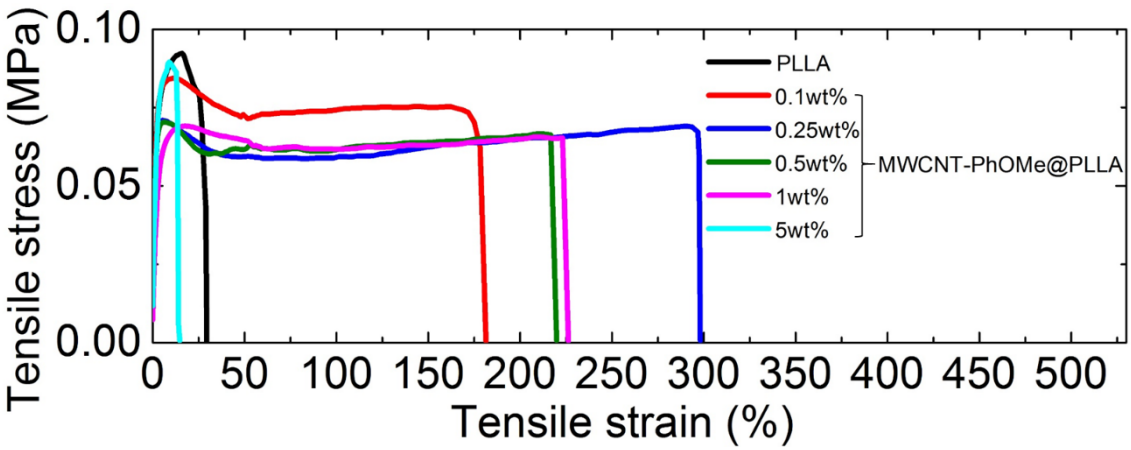

Figure 3-16: Tensile stress-strain curves for the MWCNT-PhOMe@PLLA composites having different concentrations of nanofillers in the polymer phase and for pure PLLA.

Electric resistance of MWCNT@PLLA

CNS content *(% w/w)*	***Resistance***	***St. Dev.***	***Error***
0,1	(Ω)	(Ω)	(Ω)
0,25	2,918E+14	7,249E+12	2,292E+12
0,5	7,000E+05		2,000E+04
1	1,000E+05		2,000E+04
5	7,000E+03		2,000E+02
5,00	1,200E+02		2,000E+01

Film absorbance at 1000 nm of MWCNT@PLLA

CNS content *(% w/w)*	***Absorbance (1000 nm)***
0,1	
0,25	0,78643
0,5	2,03076
1	3,86773
5	

Raman analysis of MWCNT@PLLA

CNS Content *(% w/w)*	***Peaks***							
0,1	***Raman shift****(cm^{-1})*	875	1327	1453	1603	1766	2660	2984
	Relative intensity	4,33	2,46	2,49	1,00	3,06	-	15,91
0,25	***Raman shift****(cm^{-1})*	871	1333	1453	1603	1767	2661	2948
	Relative intensity	0,24	1,57	0,18	1,00	0,08	0,28	0,81
0,5	***Raman shift****(cm^{-1})*	871	1323	1453	1602	1766	2660	2948
	Relative intensity	1,30	1,30	0,14	1,00	0,26	9,25	1,04
1	***Raman shift****(cm^{-1})*	8,73	1333	1448	1603	1766	2660	2948
	Relative intensity	0,08	1,45	0,14	1,00	0,45	0,25	0,27
5	***Raman shift****(cm^{-1})*	873	1323	1450	1603	1766	2661	2948
	Relative intensity	-	1,58	-	1,00	0,03	0,18	0,04

3.3.4.2 Preparation of CNH-PhOMe@PLLA composite materials

CNH-PhOMe content	***CNH-PhOME***	***PLLA***	***Chloroform***
[% w/w]	[mg]	[g]	[g]
0,1	2,52	2,52	42
0,25	6,30	2,52	42
0,5	12,60	2,52	42
1	25,20	2,52	42
5	126,00	2,52	42

The product CNH-PhOMe obtained from the reaction described above were divided in 5 different batches (see table for detailed quantities) and dispersed in chloroform (42 g) by bath sonication for 30 minutes.

PLLA (2.52 g) were added at the dispersion and let dissolve for one day under stirring.

The composite material solution so obtained were poured into a glass Petri dish (diameter 5.75 cm) and put in a preheated hoven at 50 °C. After 5 hours, the dried product were removed from the Petri dish as a freestanding film.

The material were characterized by TGA, DSC, Uv-vis and Raman. Also the electrical resistance of the material were measured. After that the films were cut into small speciments (4 cm x 1 cm) for the Stress-Strain mechanical characterizations.

Figure 3-17: Images of the five types of CNH-PhOMe@PLLA composites having different concentrations of nanofillers in the polymer phase.

DSC analysis of CNH@PLLA

	1st melting peak			1st crystallization peak		
CNS content (% w/w)	**Tmax** (°C)	**Tonset** (°C)	**ΔH** (J/g)	**Tmax** (°C)	**Tonset** (°C)	**ΔH** (J/g)
0,1	154,90	150,06	24,23	116,95	103,35	-23,04
0,25	154,97	150,07	23,40	116,45	103,03	-22,41
0,5	154,96	149,62	23,18	116,85	102,59	-20,33
1	154,06	150,06	24,17	117,39	103,30	-22,09
5	154,89	150,21	23,70	107,35	105,54	-23,83

	2nd melting peak				
CNS content (% w/w)	**Tmax** (°C)	**Tonset** (°C)	**ΔH** (J/g)	**Tg** (°C)	**Crystallinity (1st peak)** (%)
0,1	155,57	150,86	23,41	56,65	26,1
0,25	155,25	150,60	22,95	56,33	25,2
0,5	155,63	149,60	23,11	56,32	24,9
1	155,58	150,84	23,77	56,24	25,9
5	155,80	150,60	23,83	55,94	25,4

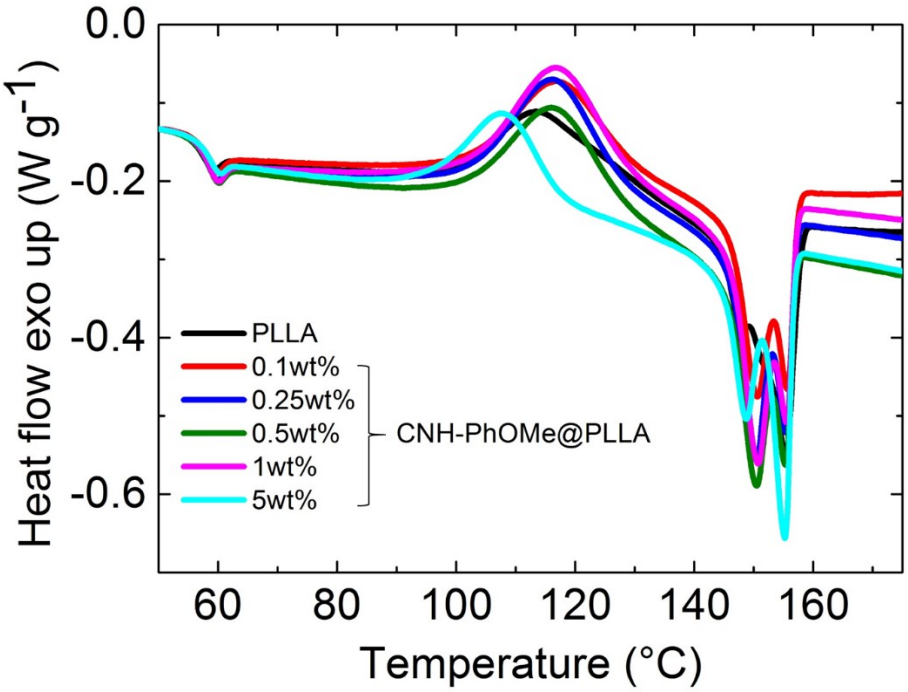

Figure 3-18: DSC traces for the five types of CNH-PhOMe@PLLA composites having different concentrations of nanofillers in the polymer phase and for pure PLLA..

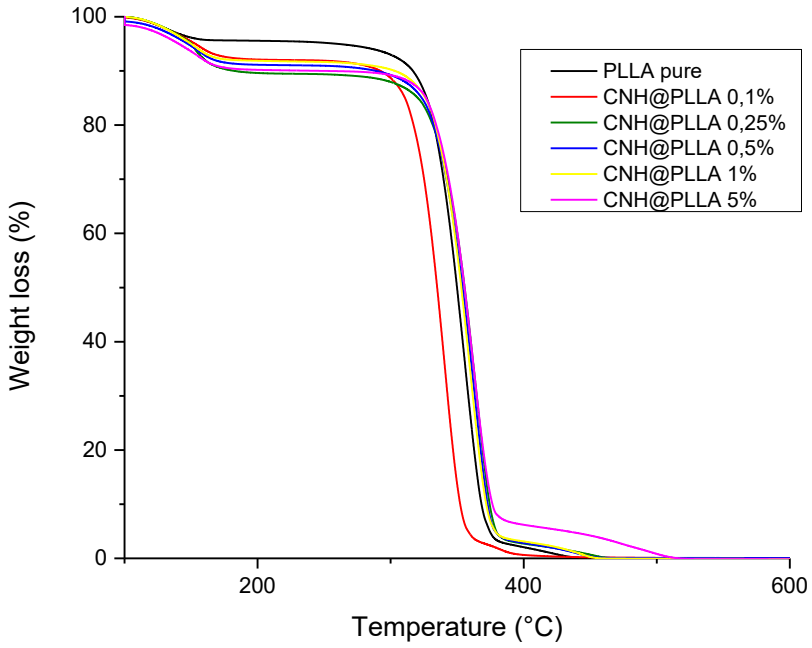

Figure 3-19: TGA for the CNH-PhOMe@PLLA composites having different concentrations of nanofillers in the polymer phase and for pure PLLA.

Stress/Strain analysis of CNH@PLLA

CNS content	***Young Modulus***	***Tenacity***	***Stress Snerv.***	***Defor. Snerv***	***Def. Max.***	***Stress break***
(% w/w)	(MPa)	(Mpa)	(Mpa)	(%)	(%)	(Mpa)
0,1	458,2	28,0	18,8	14,1	161,8	0,2
0,25	351,8	23,1	13,6	17,5	178,4	0,1
0,5	534,7	41,9	24,0	14,7	195,5	0,2
1	500,9	50,2	22,9	14,3	245,8	0,2
5	490,6	39,7	21,7	15,0	206,9	0,2

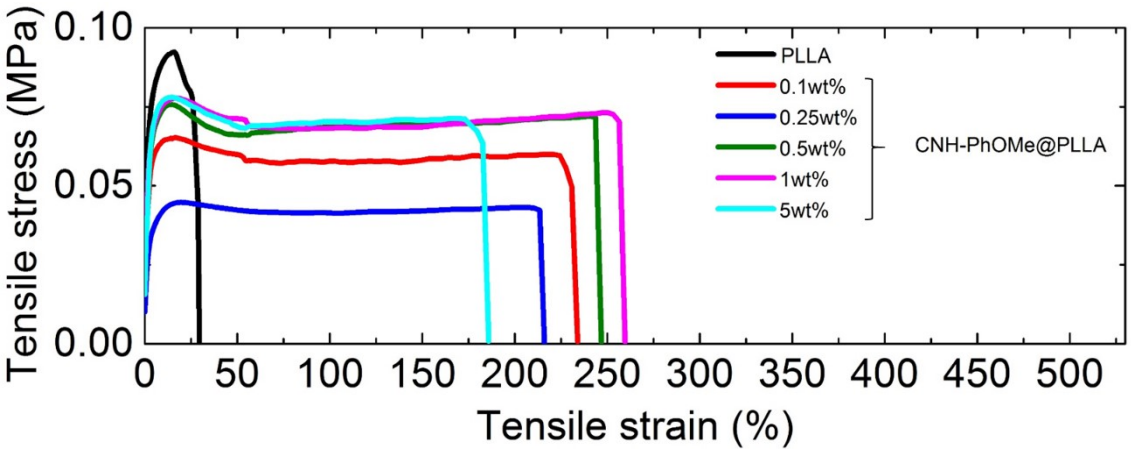

Figure 3-20: Tensile stress-strain curves for the CNH-PhOMe@PLLA composites having different concentrations of nanofillers in the polymer phase and for pure PLLA.

Electric resistance of CNH@PLLA

CNS content	***Resistance***	***St. Dev.***	***Error***
(% w/w)	(Ω)	(Ω)	(Ω)
0,10	6,741E+14	2,189E+14	6,921E+13
0,25	1,602E+14	2,913E+13	9,213E+12
0,50	2,966E+15	7,761E+13	2,454E+13
1,00	5,744E+14	7,761E+13	2,454E+13
5,00	2,458E+15	1,909E+14	6,037E+13

Film absorbance at 1000 nm of CNH@PLLA

CNS content	***Absorbance(1000 nm)***
% w/w	
0,1	0,95166
0,25	2,36679
0,5	-

Raman analysis of CNH@PLLA

CNS content	***Peaks***							
(% p/p)								
0,1	***Raman shift*** *(cm^{-1})*	874	1316	1454	1600	1766	260	2948
	Relative intensity	0,32	0,93	0,18	1,00	0,20	-	1,07
0,25	***Raman shift*** *(cm^{-1})*	871	1319	1450	1598	1767	2634	2946
	Relative intensity	0,10	0,99	0,04	1,00	0,02	0,12	0,52
0,5	***Raman shift*** *(cm^{-1})*	873	1318	1458	1598	1766	2624	2950
	Relative intensity	0,06	1,06	0,12	1,00	0,04	0,22	0,41
1	***Raman shift*** *(cm^{-1})*	873	1317	1458	1601	1764	2630	2950
	Relative intensity	0,02	1,10	0,08	1,00	0,01	0,12	0,11
5	***Raman shift*** *(cm^{-1})*	872	1317	1450	1596	1766	2627	2948
	Relative intensity	0,02	1,14	-	1,00	-	0,13	0,05

3.3.4.3 Preparation of RGO-PhOMe@PLLA composite materials

RGO-PhOMe content	*RGO-PhOME*	*PLLA*	*Chloroform*
[% p/p]	[mg]	[g]	[g]
0,1	2,52	2,52	42
0,25	6,30	2,52	42
0,5	12,60	2,52	42
1	25,20	2,52	42
5	63,00	1,26	21

The product RGO-PhOMe obtained from the reaction described above were divided in 5 different batches (see table for detailed quantities) and dispersed in chloroform (42 g or 21 g) by bath sonication for 30 minutes.

PLLA (2.52 g or 1.26 g) were added at the dispersion and let dissolve for one day under stirring.

The composite material solution so obtained were poured into a glass Petri dish (diameter 5.75 cm or 2.75 cm) and put in a preheated hoven at 50 °C. After 5 hours, the dried product were removed from the Petri dish as a freestanding film.

The material were characterized by TGA, DSC, Uv-vis and Raman. Also the electrical resistance of the material were measured. After that the films were cut into small speciments (4 cm x 1 cm) for the Stress-Strain mechanical characterizations

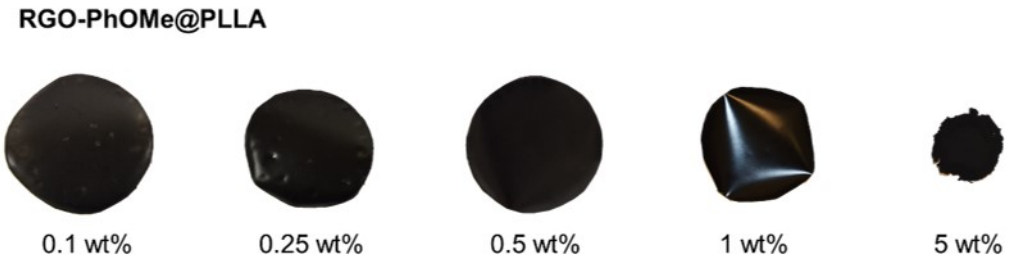

Figure 3-21: Images of the five types of RGO-PhOMe@PLLA composites having different concentrations of nanofillers in the polymer phase.

DSC analysis of RGO@PLLA

	1st melting peak			*1st crystallization peak*		
CNS content	**Tmax**	**Tonset**	**ΔH**	**Tmax**	**Tonset**	**ΔH**
(% w/w)	(°C)	(°C)	(J/g)	(°C)	(°C)	(J/g)
0,1	154,96	149,84	24,34	114,36	102,10	-20,54
0,25	154,93	150,10	23,99	113,60	101,47	-23,19

0,5	154,79	150,33	23,67	110,29	100,97	-22,13
1	154,99	150,06	24,52	107,36	97,65	-22,08
5	154,22	147,53	20,07	109,49	98,13	-10,73

2nd melting peak

CNS content *(% w/w)*	**Tmax** (°C)	**Tonset** (°C)	**ΔH** (J/g)	**Tg** (°C)	**Crystallinity (1st peak)** (%)
0,1	155,60	151,80	23,63	55,78	26,2
0,25	155,81	152,14	24,41	56,22	25,8
0,5	155,48	151,64	21,88	56,31	25,5
1	155,24	151,61	22,87	56,47	26,5
5	155,10	149,28	16,68	56,92	21,5

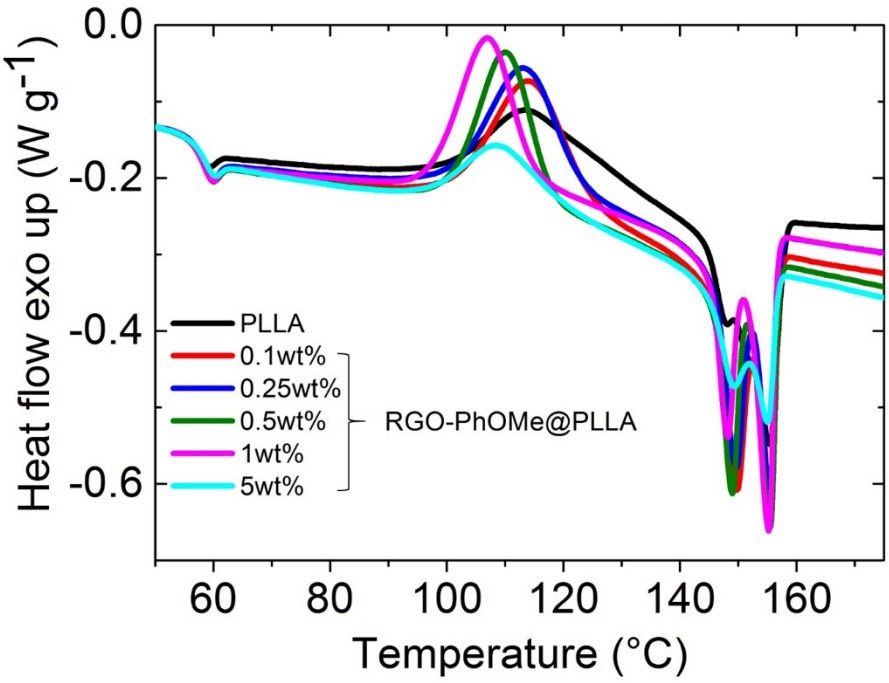

Figure 3-22: DSC traces for the five types of RGO-PhOMe@PLLA composites having different concentrations of nanofillers in the polymer phase and for pure PLLA.

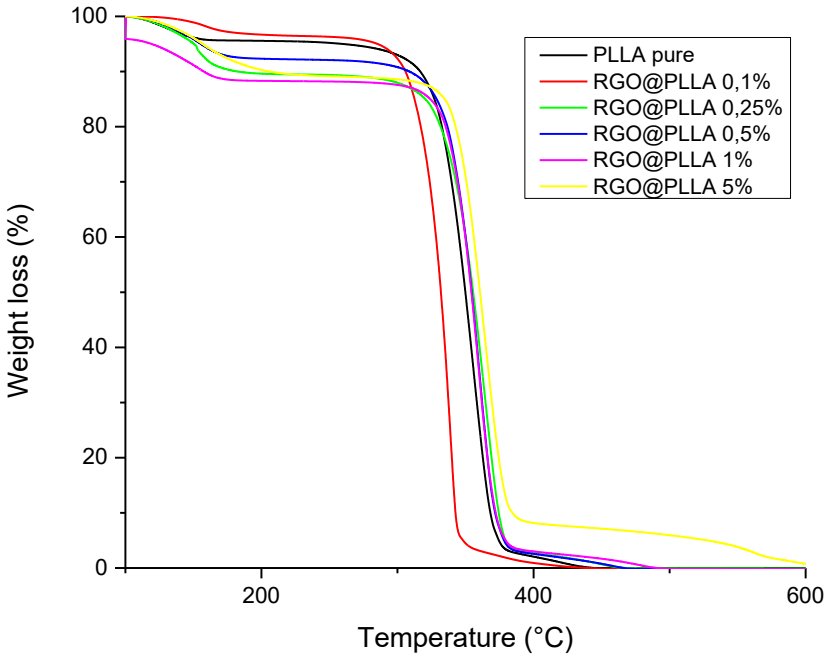

Figure 3-23: TGA for the RGO-PhOMe@PLLA composites having different concentrations of nanofillers in the polymer phase and for pure PLLA.

Stress/Strain analysis of RGO@PLLA

CNS content	***Young***	***Tenacity***	***Stress Snerv.***	***Defor. Snerv***	***Def. Max.***	***Stress break***
(% w/w)	(MPa)	(Mpa)	(Mpa)	(%)	(%)	(Mpa)
0,1	538,2	22,0	19,2	14,6	134,5	0,2
0,25	551,9	32,4	18,9	12,4	188,4	0,2
0,5	510,1	36,6	19,4	13,8	211,1	0,1
1	508,5	4,5	18,9	9,9	18,3	0,1

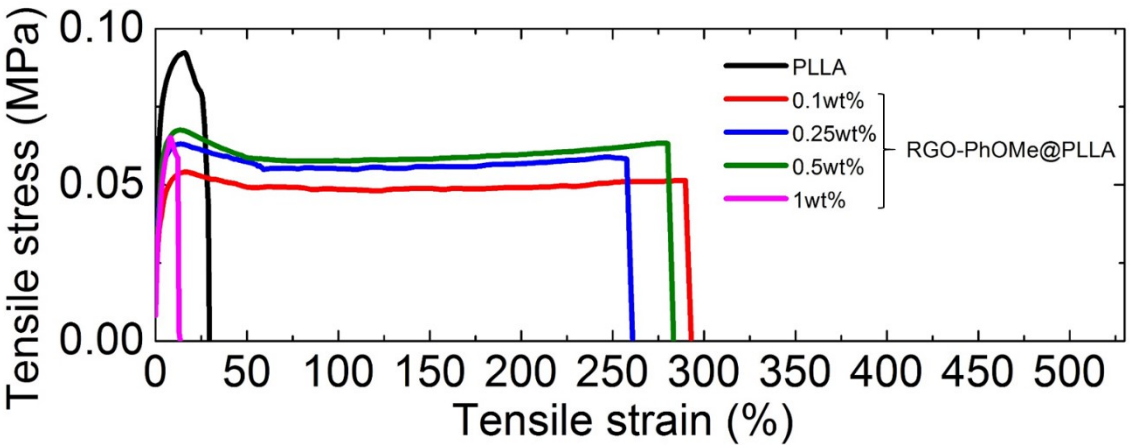

Figure 3-24: Tensile stress-strain curves for the RGO-PhOMe@PLLA composites having different concentrations of nanofillers in the polymer phase and for pure PLLA.

Electric resistance of RGO@PLLA

CNS content	***Resistance***	***St. Dev.***	***Error***
(% w/w)	(Ω)	(Ω)	(Ω)
0,10	2,066E+15	2,189E+14	6,921E+13
0,25	1,159E+15	7,934E+13	2,509E+13
0,50	2,182E+14	2,691E+12	8,511E+11
1,00	3,500E+07		2,000E+06
5,00	2,000E+04		2,000E+02

Film absorbance at 1000 nm of RGO@PLLA

CNS content	***Absorbance (1000 nm)***
% w/w	
0,1	1,01863
0,25	1,67593
0,5	-

Raman analysis of RGO@PLLA

CNS content	***Peaks***						
(% w/w)							
0,1	***Raman shift*** *(cm^{-1})*	874	1326	1450	1600	1773	2946
	Relative intensity	1,32	0,63	0,83	1,00	0,68	3,62
0,25	***Raman shift*** *(cm^{-1})*	875	1338	1450	1600	1774	2947
	Relative intensity	0,13	0,90	0,49	1,00	0,12	0,52
0,5	***Raman shift*** *(cm^{-1})*	874	1338	1451	1598	1774	2950
	Relative intensity	0,10	0,88	0,48	1,00	0,03	0,35
1	***Raman shift*** *(cm^{-1})*	873	1317	1458	1601	1764	2950
	Relative intensity	0,13	0,98	1,01	1,00	-	0,15
5	***Raman shift*** *(cm^{-1})*	872	1317	1450	1596	1766	2948
	Relative intensity	-	0,98	0,49	1,00	-	0,06

Measured film thicknesses for the functionalized-CNS@PLLA films.[a]

wt%	***MWCNT-PhOMe@PLLA*** *[µm]*	***CNH-PhOMe@PLLA*** *[µm]*	***RGO-PhOMe@PLLA*** *[µm]*
0.1	325	330	331
0.25	320	338	325
0.5	305	331	340
1	323	340	345
5	322	345	-[b]

[a] For the pure PLLA film a thickness of 335 µm was measured. [b] Not measurable due to extreme fragility of the specimen.

3.3.5 **Preparation of CNS-PhOMe@PLLA fibers composite materials**

All the electrospinning procedures have been performed in the laboratories of Prof. C. Marega.

Small amount of the 0.25% and 5% CNS-PhOMe@PLLA films were used for the preparation of the analogous fibers by electrospinning. The solid composite materials were dissolved in a mixture of chloroform and DMF (9:1 v/v) in order to obtain solutions (20 ml each) at 6% w/w as concentration. All the mixture were kept under agitation for 3 days in sealed vials, in order to obtain a complete rehomogenization of the material. The so obtained solution were spun using an home made electrospinning apparatus set at 18kV as voltage, 0.03mL/min as flow rate and 15 cm as distance between the needle and the collecting plate.

Transmission electron microscopy (TEM) images were recorded on samples spun directly onto TEM copper grids for 60 seconds with a Tecnai G2 microscope (FEI) operating at 100 kV. AFM images were recorded on samples spun onto Graphene Supermarket silicon prime wafers (oxide thickness: 285 nm) for 60 seconds (see AFM details later in the appendix).

TEM images of the electrospun MWCNT@PLLA 5%

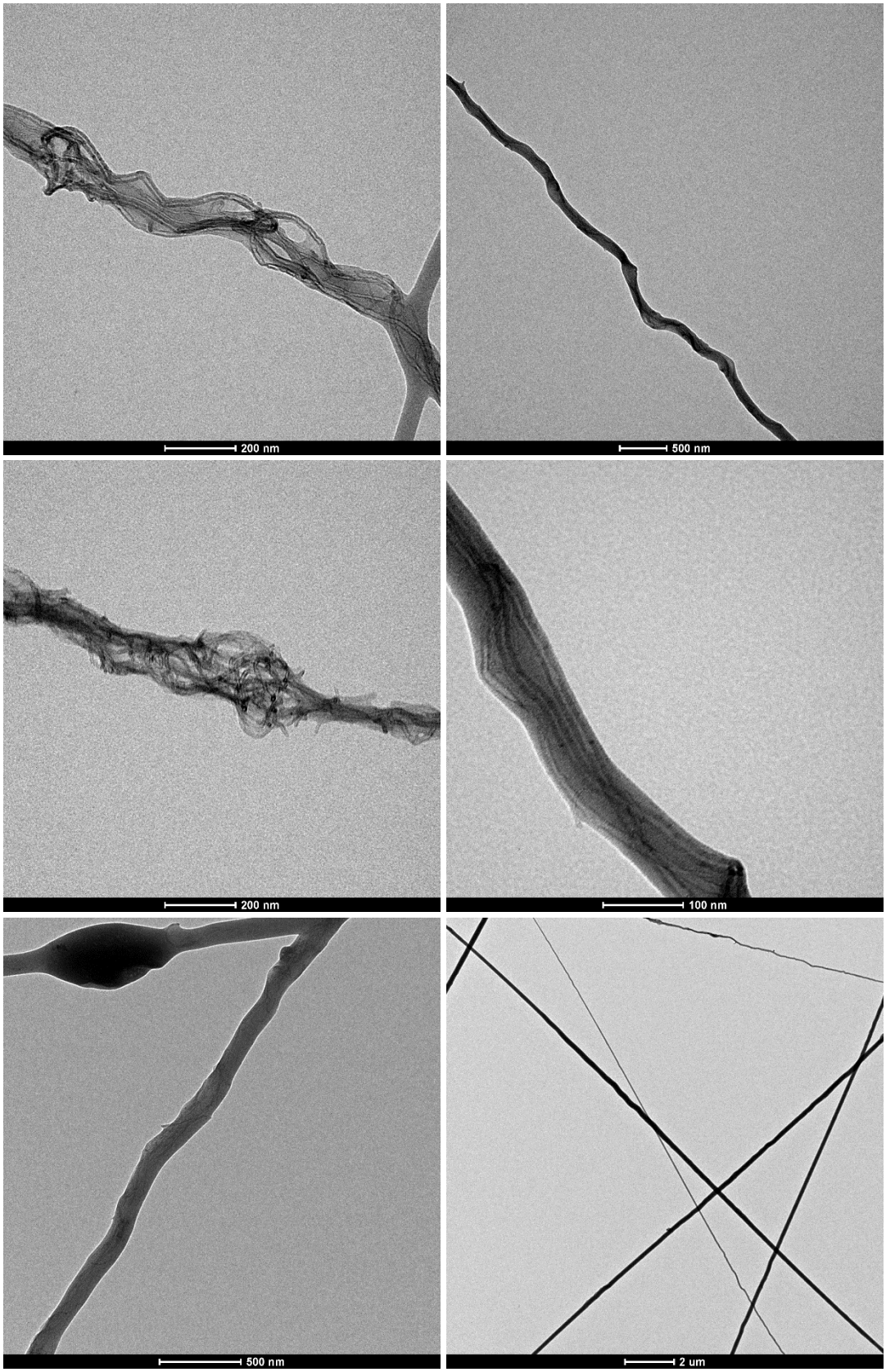

TEM images of the electrospun CNH@PLLA 5%

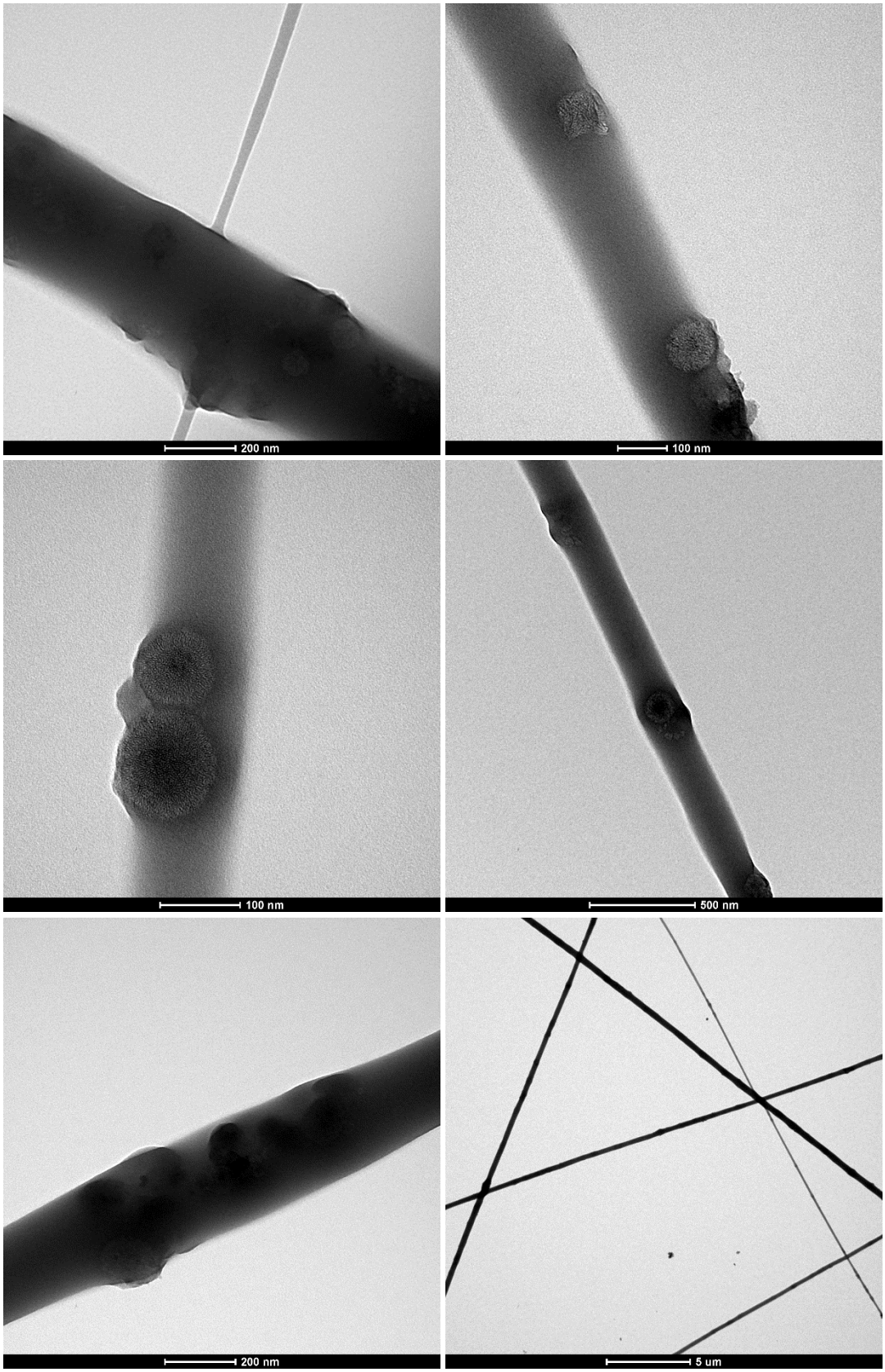

TEM images of the electrospun RGO@PLLA 5%

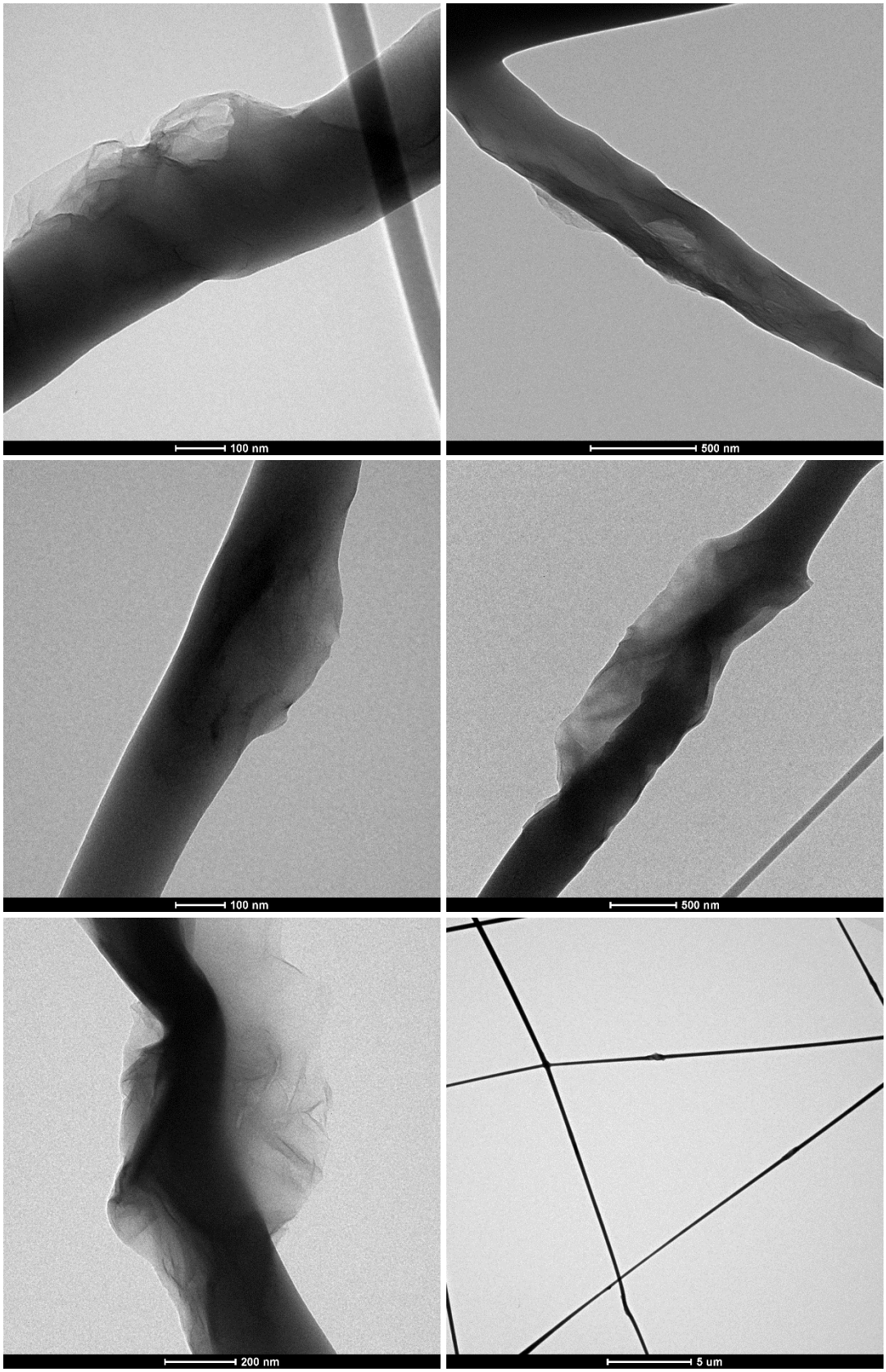

3.3.6 **Functionalizations with 4-aminobenzoic acid**

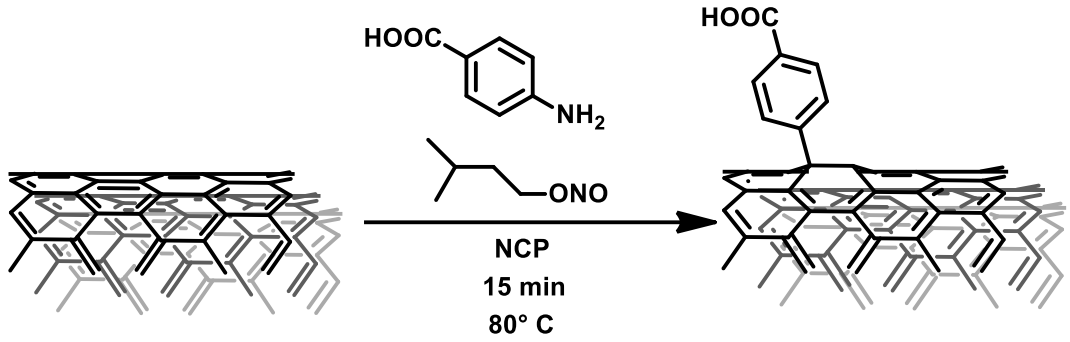

Reagent	***Weight*** *[mg]*	***Volume*** *[mL]*	***Moles*** *[mmol]*
MWCNTs	21	/	1.75[a]
4-*aminobenzoic acid*	572	/	4.37
Isopentyl nitrite	/	0.6	4.37
NCP	/	40	/

[a]: Moles calculated from the atomic weight of carbon, considering MWCNTs exclusively made of sp2 carbon.

21 mg of MWCNTs were dispersed in 30 mL of NCP by microtip sonication for 10 minutes, intensity 6*W* and interval 3*s* ON 3*s* OFF.

The dispersion was transferred in a 250 mL 3 neck round bottom flask and additional 10 mL of CHP were used to disperse the residue on the bottom of the vial and complete the transfer. From this moment the dispersion was kept under stirring and nitrogen flux.

572 mg of 4-aminobenzoic acid were added and the dispersion was sonicated in the bath sonicator for 5 minutes to ease the dispersion of the reagents. After heating the mixture to 80°*C*, 0.6 mL of isopentylnitrite were added. The reaction went for 15 minutes at 80°*C* under stirring and nitrogen flux. 200 mL of cold methanol were added to the crude of reaction and the dispersion was filtered on a *Fluoropore* 0.2*μm* membrane.

The product was washed with 100 mL of methanol, then dispersed in 70 mL of DMF using the bath sonicator for 5 minutes and filtered on the same filter, previously washed. The product was washed again with a sonication-filtration procedure twice, dispersing in 70 mL of methanol and filtering on the same membrane previously washed.

After the last filtration the product was washed with additional 75mL of methanol, dried and characterized.

TGA (nitrogen) 9.4% weight loss at 550°*C*.

3.3.6.1 Solubility dependence on pH

3 mg of dry product were dispersed in 8 mL of deionized water by ultrasonication for 10 minutes in the bath sonicator. The dispersion was centrifuged at 3500*rpm* for 5 minutes and the supernatant was collected. Three vials were filled with 2 mL each of the supernatant. One was kept with the as-prepared solution, the other two were treated respectively with 10*μL* of a 0.1*M* solution of NaOH for the base treatment, and 10*μL* of a 0.1*M* solution of HCl for the acid treatment.

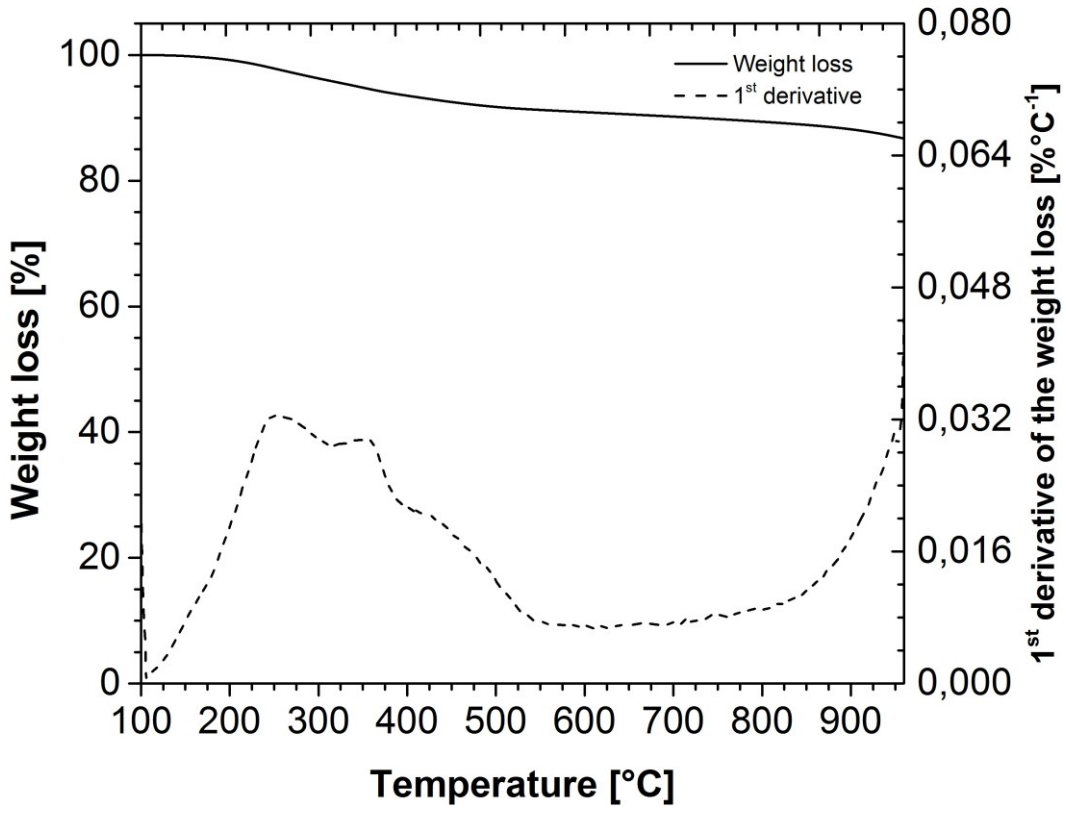

Figure 3-25: TGA of MWCNT-PhCOOH in nitrogen atmosphere.

3.3.7 **Amidation reaction with amino-TEMPO on the MWCNT-PhCOOH**

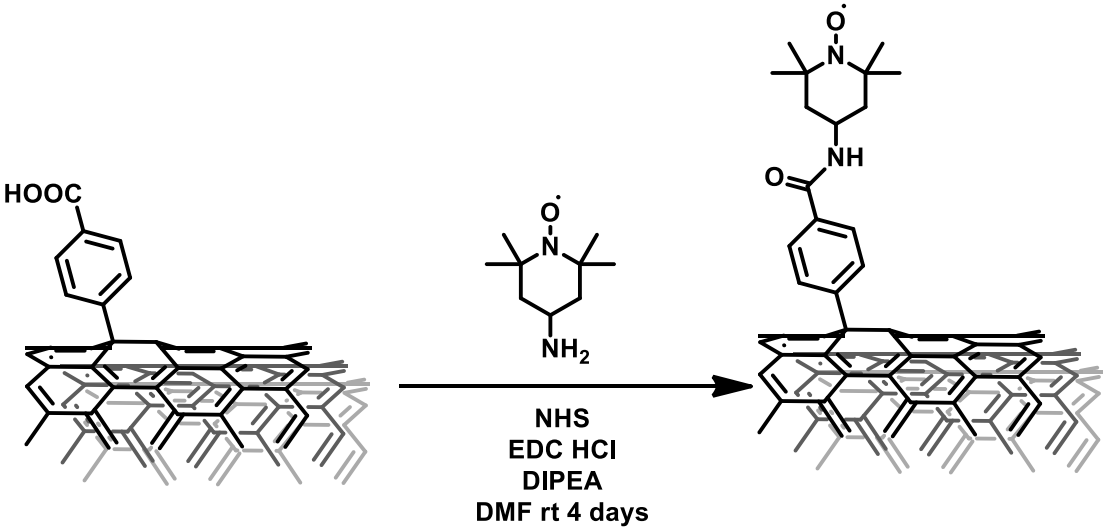

Reagent	***Weight*** *[mg]*	***Volume*** *[mL]*	***Moles*** *[mmol]*
MWCNT-PhCOOH	5	/	0.004[a]
4-amino-TEMPO	8.2	/	0.05
EDC·HCl	8.6	/	0.05
DIPEA	/	0.01	
NHS	13.5	/	0.12
a-DMF	/	83	/

[a]: the moles are calculated from the functional group weight loss in the TGA

The most soluble fraction of MWCNT-PhCOOH was extracted dispersing 2 mg of product in 10 mL of MilliQ water by ultrasonication. The dispersion was then centrifuged at 3500*rpm* for 5 minutes and the supernatant was collected. This procedure was repeated until all the sample was extracted. The collection of the supernatants was freeze dried. The estimated mass of the extracted product is 5 mg.

The dried product was transferred in a flask put under nitrogen flux. 60 mL of anhydrous DMF were added with a syringe and the mixture was sonicated for 10 minutes in the bath sonicator.

A solution of 13.5 mg of N-Hydroxysuccinimide in 10 mL of anhydrous DMF and 10*μL* of DIPEA was added and the mixture was sonicated for 10 minutes. A solution of 8.6 mg of *EDC·HCl* in 8 mL of anhydrous DMF was added and the mixture was sonicated for 10 minutes.

Finally a solution of 8.2 mg of 4-amino-TEMPO in 5 mL of anhydrous DMF was added. The reaction went for 4 days at room temperature under stirring and nitrogen flux.

The product was filtered on a *Fluoropore* 0.2μm membrane and washed with 50 mL of DMF, 100 mL of methanol, 100 mL of chloroform and 50 mL more of methanol.

The solid was dispersed in 70 mL of methanol by sonication and the dispersion was split in two falcons with 35 mL of dispersion each. The dispersion was centrifuged at 12000*rpm* for 30 minutes. The supernatant was separated and stored while the solid on the bottom was disperse again in 35 mL of fresh methanol and centrifuged; the procedure was repeated 3 times.

A last dispersion in 70 mL of methanol was performed and the solid was collected by filtration on a *Fluoropore* 0.2μm membrane.

The wastewater from each step was concentrated evaporating the solvent resulting in 150μL of solution. The concentrated solutions were analyzed by EPR spectroscopy.

The product was characterized by EPR spectroscopy.

3.3.8 **Amidation reaction with TEMPO-peptide on the MWCNT-PhCOOH**

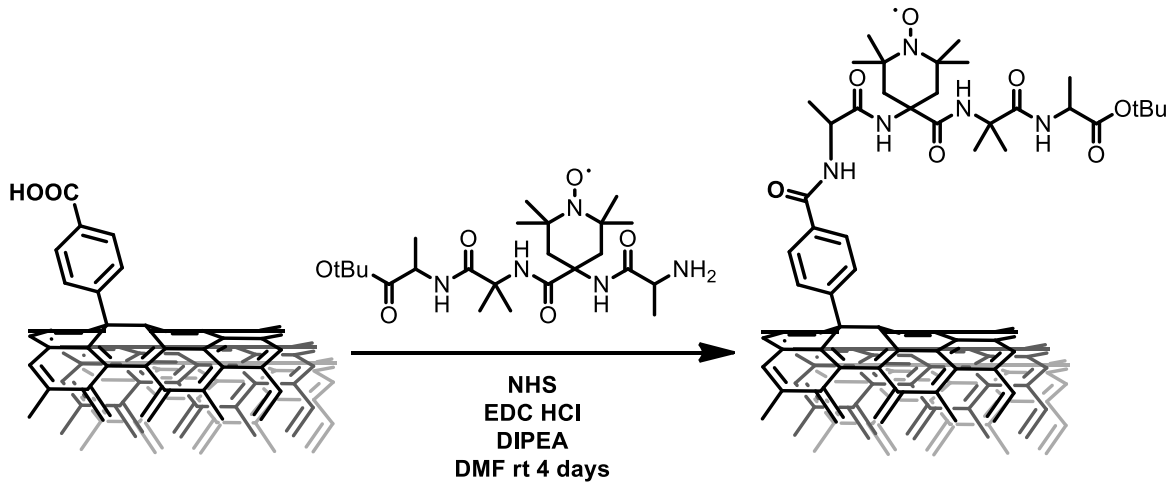

Reagent	***Weight*** *[mg]*	***Volume*** *[mL]*	***Moles*** *[mmol]*
MWCNT-PhCOOH	10	/	0.008[a]
TEMPO-Peptide	50	/	0.1
EDC·HCl	17.2	/	0.1
DIPEA	/	0.02	
NHS	27	/	0.24
a-DMF	/	90	/

[a]: the moles are calculated from the functional group weight loss in the TGA

The most soluble fraction of MWCNT-PhCOOH was extracted dispersing 2 mg of product in 10 mL of MilliQ water by ultrasonication. The dispersion was then centrifuged at 3500*rpm* for 5 minutes and the supernatant was collected. This procedure was repeated until all the sample was extracted. The collection of the supernatants was freeze dried. The estimated mass of the extracted product is 10 mg.

The dried product was transferred in a flask put under nitrogen flux. 60 mL of anhydrous DMF were added with a syringe and the mixture was sonicated for 10 minutes in the bath sonicator.

A solution of 27 mg of N-Hydroxysuccinimide in 10 mL of anhydrous DMF and 20*μL* of DIPEA was added and the mixture was sonicated for 10 minutes. A solution of 17.2 mg of *EDC · HCl* in 8 mL of anhydrous DMF was added and the mixture was sonicated for 10 minutes.

Finally a solution of 50 mg of TEMPO-peptide in 10 mL of anhydrous DMF was added. The reaction went for 4 days at room temperature under stirring and nitrogen flux.

The product was filtered on a *Fluoropore* 0.2*µm* membrane and washed with 100 mL of DMF, 200 mL of methanol, 200 mL of chloroform and 100 mL more of methanol.

The solid was dispersed in 50 mL of methanol by sonication and the dispersion was centrifuged at 12000*rpm* for 30 minutes. The supernatant was separated while the solid on the bottom was disperse again in 50 mL of fresh methanol and centrifuged; the procedure was repeated 3 times.

The product after the third centrifugation step was dried and characterized by EPR spectroscopy and TGA.

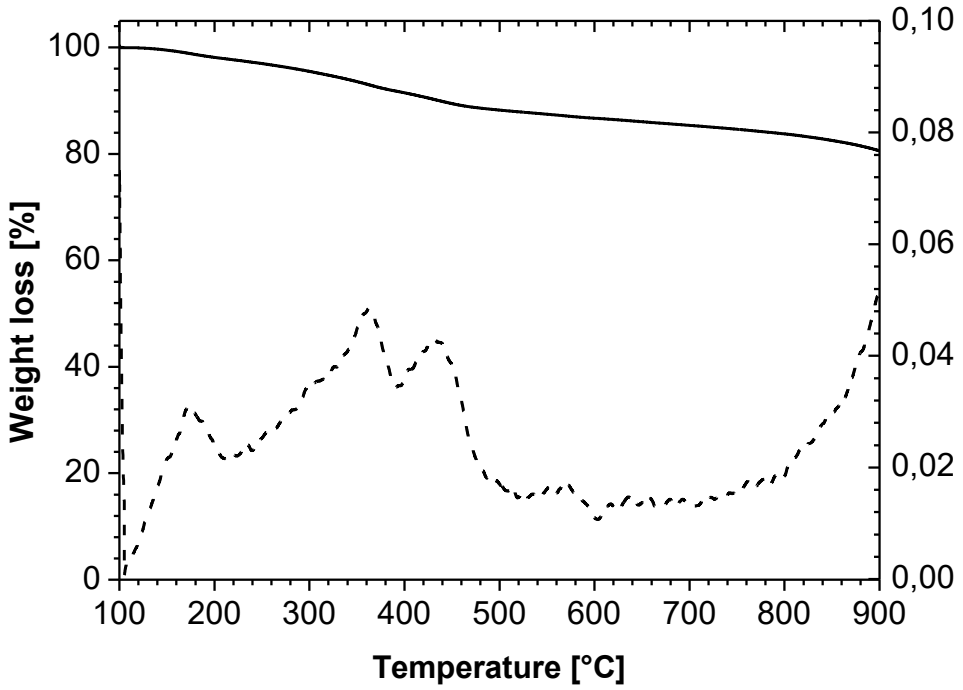

Figure 3-26: TGA of MWCNT-Peptide in nitrogen atmosphere.

3.3.9 **Functionalizations with p-vinyl aniline**

3.3.9.1 Synthesis of MWCNT-Cof-A

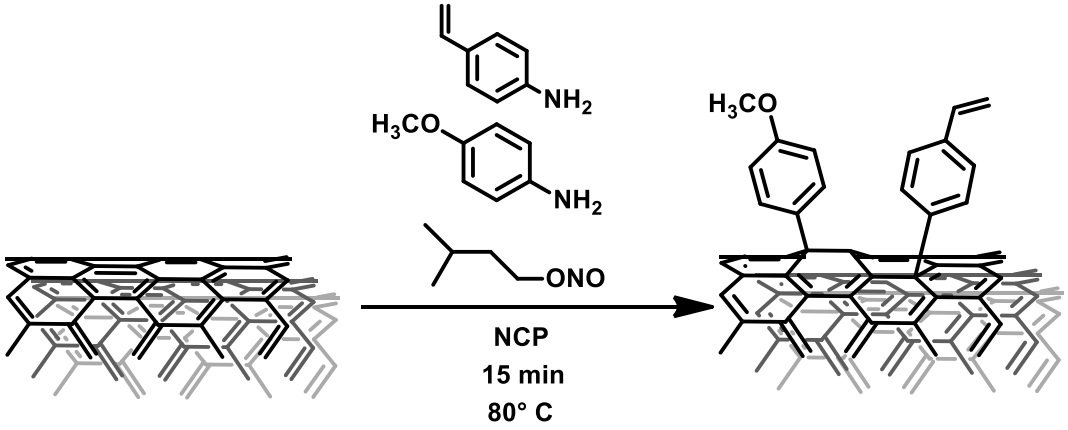

Reagent	***Weight*** *[mg]*	***Volume*** *[mL]*	***Moles*** *[mmol]*
MWCNTs	21	/	1.75[a]
p-*vinylaniline*	/	316	2.6
4-*methoxyaniline*	108	/	0.88
Isopentyl nitrite	/	0.47	3.5
NCP	/	40	/

[a]: Moles calculated from the atomic weight of carbon, considering MWCNTs exclusively made of sp2 carbon.

21 mg of MWCNTs were dispersed in 30 mL of NCP by microtip sonication for 10 minutes, intensity 6*W* and interval 3*s* ON 3*s* OFF.

The dispersion was transferred in a 250mL 3 neck round bottom flask using additional 10 mL of CHP to disperse the residue on the bottom of the vial and complete the transfer. From now on the dispersion was kept under stirring and nitrogen flux.

108 mg of *4*-methoxyaniline and 316 mL of 4-vinylaniline were added to the dispersion and sonicated in the bath sonicator for 5 minutes to ease the dispersion of the reagents.

After heating the mixture to 80°*C*, 0.471 mL of isopentyl nitrite were added.

The reaction went for 15 minutes under stirring and nitrogen flux at 80°*C*. 200 mL of cold methanol were added to the crude of reaction and the dispersion was filtered on a *Fluoropore* 0.2*µm* membrane.

The filtered solid was washed with 100 mL of methanol, then dispersed in 75 mL of DMF using the bath sonicator for 5 minutes, and filtered on the same filter, previously

washed. The moiety left on the bottom of the becker that was not dispersed in DMF was sonicated in 20 mL of MeOH and filtered. This procedure was repeated multiple times until all the solid was dispersed and then filtered. A total of 120 mL of MeOH were used for this procedure. Finally the product on the filter was rinsed with 50 mL of MeOH, dried and characterized.

TGA (nitrogen) 14.3% weight loss at 500°*C*.

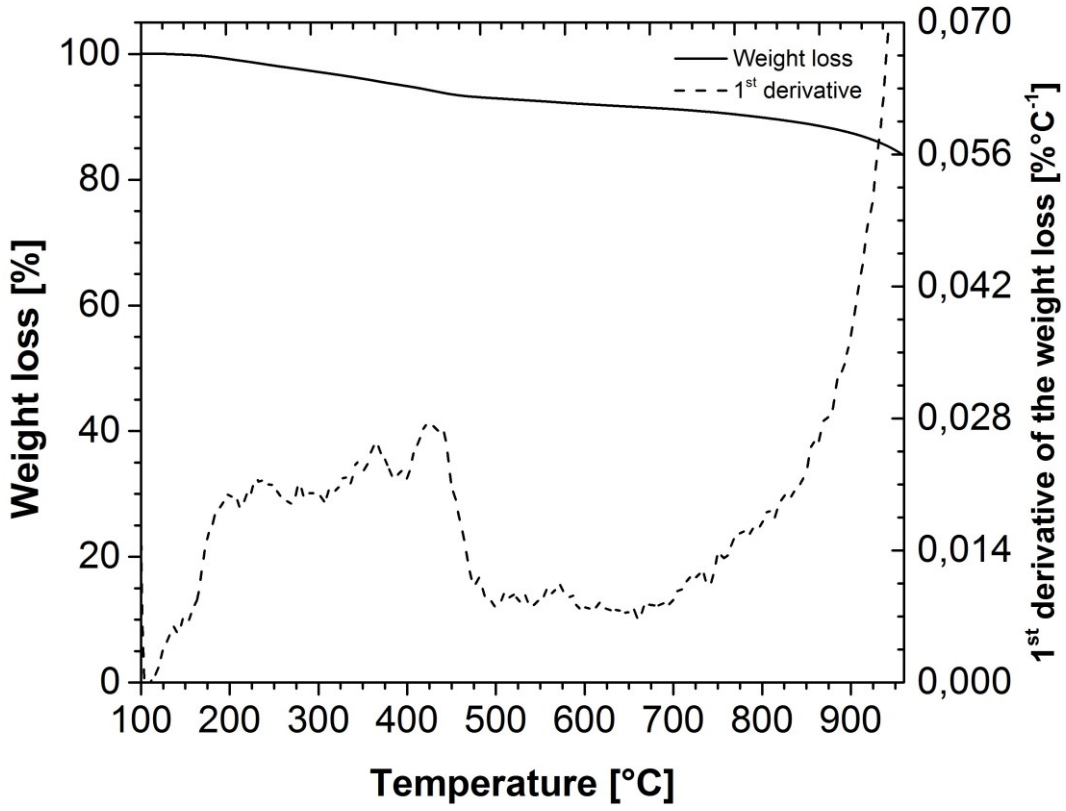

Figure 3-27: TGA of MWCNT-Cof-A in nitrogen atmosphere.

3.3.9.2 Synthesis of MWCNT-Cof-B

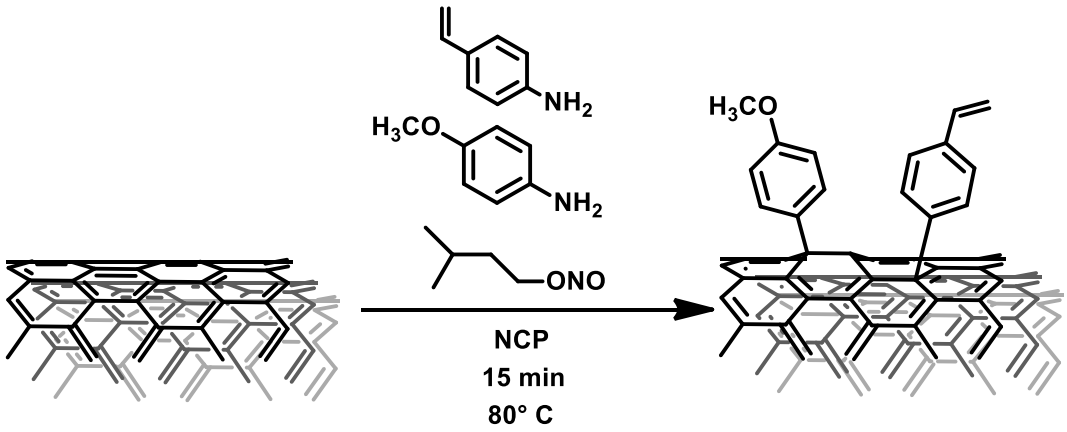

Reagent	*Weight* [mg]	*Volume* [mL]	*Moles* [mmol]
MWCNTs	23	/	1.92[a]
p-*vinylaniline*	/	0.242	1.92
4-*methoxyaniline*	236	/	1.92
Isopentyl nitrite	/	0.47	3.8
NCP	/	40	/

[a]: Moles calculated from the atomic weight of carbon, considering MWCNTs exclusively made of sp2 carbon.

23 mg of MWCNTs were dispersed in 30 mL of NCP by microtip sonication for 10 minutes, intensity 6*W* and interval 3*s* ON 3*s* OFF.

The dispersion was transferred in a 250mL 3 neck round bottom flask using additional 10 mL of CHP to disperse the residue on the bottom of the vial and complete the transfer. From now on the dispersion was kept under stirring and nitrogen flux.

236 mg of *4*-methoxyaniline and 0.242 mL of 4-vinylaniline were added to the dispersion and sonicated in the bath sonicator for 5 minutes to ease the dispersion of the reagents.

After heating the mixture to 80° *C*, 0.515 m*L* of isopentylnitrite were added.

The reaction went for 15 minutes under stirring and nitrogen flux at 80° *C*. 200 mL of cold methanol were added to the crude of reaction and the dispersion was filtered on a *Fluoropore* 0.2 *µm* membrane.

The filtered solid was washed with 100 mL of methanol, then dispersed in 80 mL of DMF using the bath sonicator for 5 minutes, and filtered on the same filter, previously washed. The moiety left on the bottom of the becker that was not dispersed in DMF was sonicated in 20 mL of MeOH and filtered. This procedure was repeated multiple

times until all the solid was dispersed and then filtered. A total of 100 mL of MeOH were used for this procedure. Finally the product on the filter was rinsed with 50 mL of MeOH, dried and characterized.

TGA (nitrogen) 11.8% weight loss at 500° *C*.

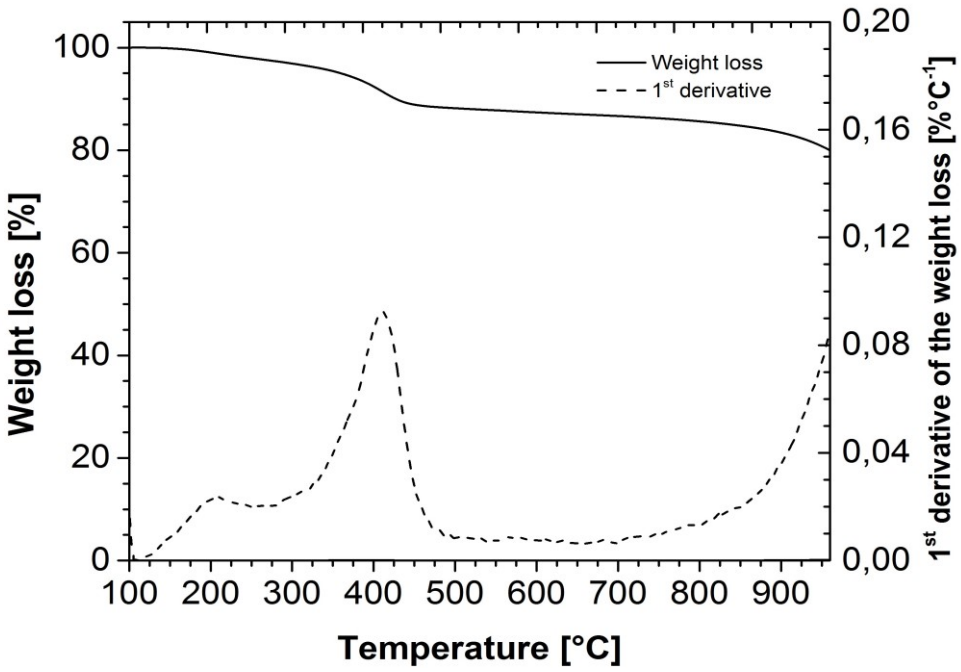

Figure 3-28: TGA of MWCNT-Cof-B in nitrogen atmosphere.

3.3.10 **Grafting from of polystyrene**

Table reports the reagent amounts and reaction times for the in-situ polymerizations. The reactions were carried under stirring at 80°*C* in an oil bath.

f-MWCNTs	***Styrene*** *[g]*	***Benzoyl peroxide*** *[mg]*	***Reaction time***
30 mg pristine MWCNTs	3	60	4 hours
≈3 mg of MWCNT-Cof-A	6	120	4 hours
≈3 mg of MWCNT-Cof-B	6	120	4 hours

After the solidification of the polymer, the composite was dissolved in THF in a ratio 1 : 3 (w/w) under stirring overnight. Then 5 volumes of methanol were added to precipitate the composite. The mixture was sonicated while manually stirring to ease the complete precipitation and avoid lumps of wet composite. The precipitate was filtered and dried.

3.3.11 **Synthesis and characterization of 4-(4-methoxyphenilazo)-N,N-dimethylaniline**

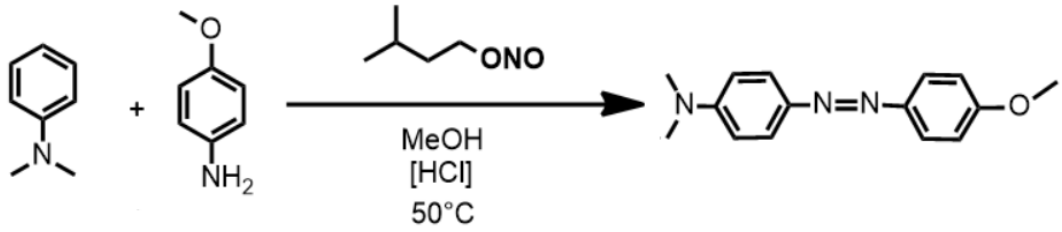

Reagent	***MW*** *[g/mol]*	***Weight*** *[g]*	***Volume*** *[mL]*	***Moles*** *[mmol]*
N,N-dimethylaniline	121.19	0.491	0.514	4.05
4-methoxyaniline	123.15	0.503	/	4.08
Isopentyl nitrite	117.15	0.471	0.540	4.01
MeOH (solvent)	32.04	/	40	/
HCl 1 M	36.46	/	0.5	/

The N,N-dimethylaniline (0.491 g, 4.05 mmol) were mixed with the 4-methoxyaniline (0.503 g, 4.08 mmol) in MeOH (40 mL). The reaction mixture were heated at 50 ° C and under magnetic agitation were added a small amount of HCl 1 M (2.5 mL).

At this point the isopentylnitrite (0.540 mL, 4.01 mmol) were added and the reaction went for 24 hours.

The reaction mixture were died under vacuum to remove the solvent and other volatile species like the unreacted isopentylnitrite. The crude dry product were dissolved in chloroform (100 mL) and extracted 3 times with acidic water (100 mL). The organic fraction were dried and the dry product were dissolved in MeOH(100 mL) and extracted 3 times with hexane (100 mL). The organic fraction were dried and the obtained product were characterized by TLC (petroleum ether/Ethyl acetate 2:3), Uv-vis and H-NMR.

3.3.12 **Synthesis and characterization of 1,3-bis(4-methoxyphenil)triazene**

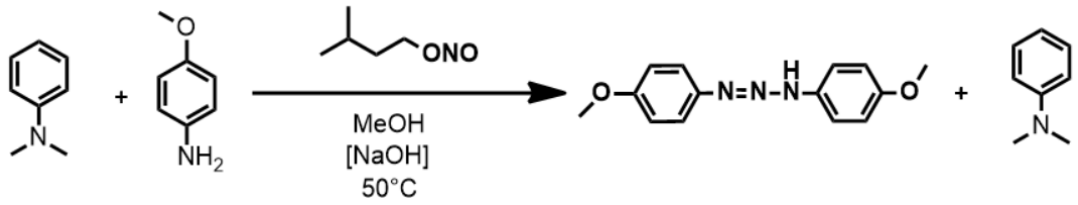

Reagent	***MW*** *[g/mol]*	***Weight*** *[g]*	***Volume*** *[mL]*	***Moles*** *[mmol]*
N,N-dimethylaniline	121.19	0.910	0.952	7.50
4-methoxyaniline	123.15	0.928	/	7.51
Isopentyl nitrite	117.15	0.872	1	7.49
MeOH (solvent)	32.04	/	80	/

NaOH 1 M	39.99	/	1	/

The N,N-dimethylaniline (0.910 g, 7.50 mmol) were mixed with the 4-methoxyaniline (0.928 g, 7.51 mmol) in MeOH (80 mL). The reaction mixture were heated at 50 ° C and under magnetic agitation were added a small amount of HCl 1 M (1 mL).

At this point the isopentylnitrite (0.872 mL, 7.49 mmol) were added and the reaction went for 24 hours.

The reaction mixture were dried under vacuum. The crude product were purified by column chromatography (petroleum ether/ethyl acetate 2:3). The fractions containing the clean product were dried and characterized by Uv-vis.

3.3.13 **Synthesis and characterization of 1,3-bis(4-methoxyphenil)triazene**

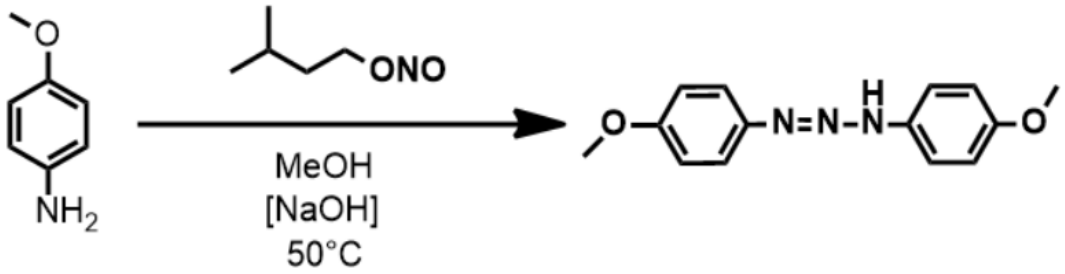

Reagent	***MW*** *[g/mol]*	***Weight*** *[g]*	***Volume*** *[mL]*	***Moles*** *[mmol]*
4-methoxyaniline	123.15	0.926	/	7.51
Isopentyl nitrite	117.15	0.872	1	7.44
MeOH (solvent)	32.04	/	80	/
NaOH 1 M	40.00	/	1	/

The 4-methoxyaniline (0.926 g, 7.51 mmol) were dissolved in MeOH (80 mL). The reaction mixture were heated at 50 ° C and under magnetic agitation were added a small amount of HCl 1 M (1 mL).

At this point the isophentylnitrite (0.872 mL, 7.49 mmol) were added and the reaction went for 24 hours.

The reaction mixture were dried under vacuum. The crude product were purified by column chromatography (petroleum ether/ethylacetate 2:3). The fractions containing the clen product were dried and characterized by Uv-vis, H-NMR, FT-IR.

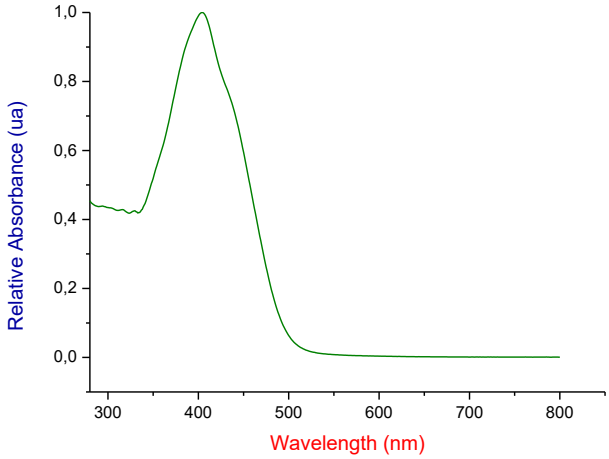

Figure 3-29: Uv-Vis spectrum of P1 in EtOH.

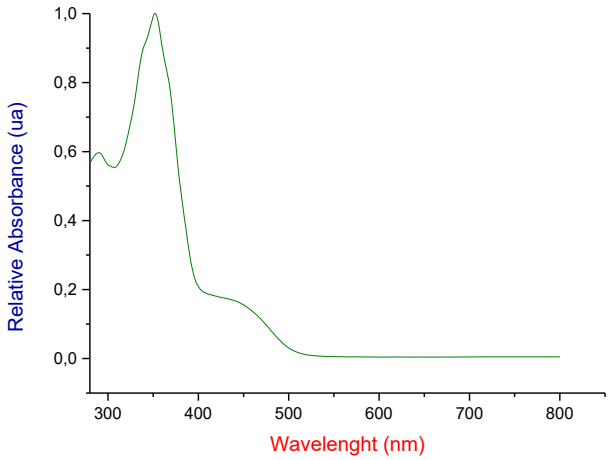

Figure 3-30:Uv-Vis spectrum of P2* in cyclohexane.

4 Appendix

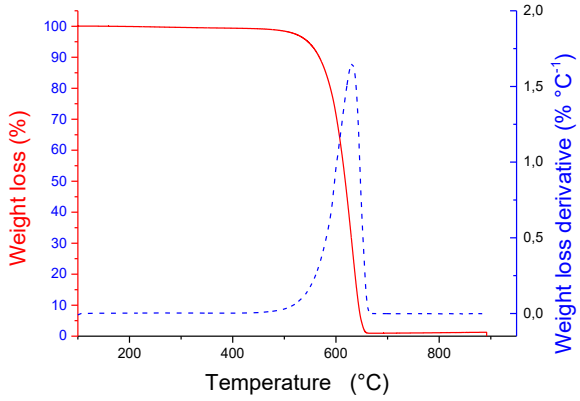

Figure 4-1: TGA of a sample of pristine MWCNTs in air (heating rate 10 °C min^{-1}).

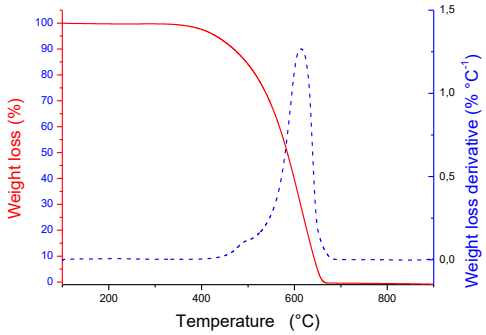

Figure 4-2 TGA of a sample of pristine CNHs in air (heating rate 10 °C min^{-1}).

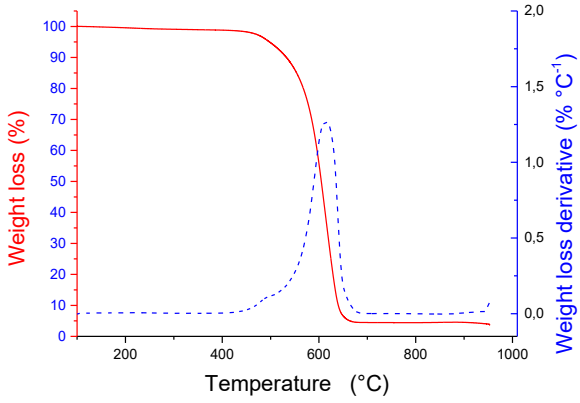

Figure 4-3 TGA of a sample of pristine RGO in air (heating rate 10 °C min^{-1}).

Characterization of the pure PLLA film

DSC analysis of pure PLLA

1st melting peak			***1st crystallization peak***		
Tmax (°C)	**Tonset** (°C)	**ΔH** (J/g)	**Tmax** (°C)	**Tonset** (°C)	**ΔH** (J/g)
155,60	151,12	25,66	113,61	101,31	15,84

2nd melting peak				
Tmax (°C)	**Tonset** (°C)	**ΔH** (J/g)	**Tg** (°C)	**Crystallinity (1st peak)** (%)
155,46	149,15	27,97	55,22	30,08

Stress/strain analysis of pure PLLA

Young modulus	***Tenacity***	***Stress Snerv.***	***Defor. Snerv***	***Def. Max.***	***Stress break***
(MPa)	(Mpa)	(Mpa)	(%)	(%)	(Mpa)
871,2	15,2	28,1	14,3	65,2	0,3

Electrical resistance of pure PLLA

Resistance *(Ω)*	***Dev. St.*** *(Ω)*	***Error*** *(Ω)*
3,34E+15	3,98E+14	1,25E+14

Raman analysis of pure PLLA

Peaks				
Raman shift *(cm^{-1})*	874	1452	1768	2948
Relative intensity	0,29	0,16	0,17	1,00

Details of AFM measurements

The nanoscale electrical conductivity was assessed within the range of process parameters accessible for this DC based technique (±10 V maximum sample bias with tip set to virtual ground, and current detection limit down to ~ 1 pA level). The current mapping measurements were carried out at the lowest possible, yet stable, vertical contact force (~0.1 V in arbitrary deflection value, corresponding to ~18 nN) that allowed to measure some current level, in order not to damage either the sample or the tip. The CAFM was equipped with a dual-gain Orca probe-holder (Asylum Research, US), with two current converters and amplifiers of sensitivities 1 V/μA and 1 V/nA for the C2 and Cu channels, respectively, to be used in the current ranges (absolute values) of 10 nA-10 μA and 0-10 nA, respectively. Only when no current was detected at even the highest possible bias (±10 V to the sample, with tip at virtual ground) on the more sensitive Cu channel, was the contact force increased up to a factor of 4, to check for possible conductance. Both current images and local I-V curves at given points of conductive film, as previously identified in a current image, were acquired. By using the contact mode, at the base of CAFM, with fast scan at 90° with respect to the cantilever axis, the lateral deflection (so-called lateral force) images were also collect and the qualitative tip-surface friction was mapped (by making the calculation of lateral deflection trace minus lateral deflection retrace, divided by 2). This channel was used to check for possible chemical inhomogeneity of the surface, correlated to either the sample composition or possible ambient contaminants.

Figures 4-4b (EFM) and 4-4c (SKPM) of the bare PLLA fibers sample show very good correlation, exhibiting contrast at both the (insulating) fibers and at a contamination on the substrate (probably due to a dried drop of some liquid, e.g. solvents). Figure 4-4c in particular is quantitative, and described better the excess accumulation of charge at the large polymer beads formed during electrospinning at the fiber on the left hand side. On fibers of CNH and RGO containing composites similar results were obtained, with only bright contrast at the fibers (no voltage drop i.e. electrical conduction detected). For the images of CNT containing composite fibers, instead, regions with either local lower contrast at some fibers (e.g. that on the right in Figure 4-4e or even no contrast (top-left in Figure 4-4g) appeared. There, some loss of potential probably due to either conductive fillers or conduction along the fiber obviously occurred. In Figure 4-4h the potential of panel 4-4g has been overlaid as color on the 3D topography of panel 4-4f, showing more clearly the effect of spread of EFM/SKPM contrast around the structure, due to the long range of the electrostatic forces in-plane (and partly also to the effect of the elevation height).

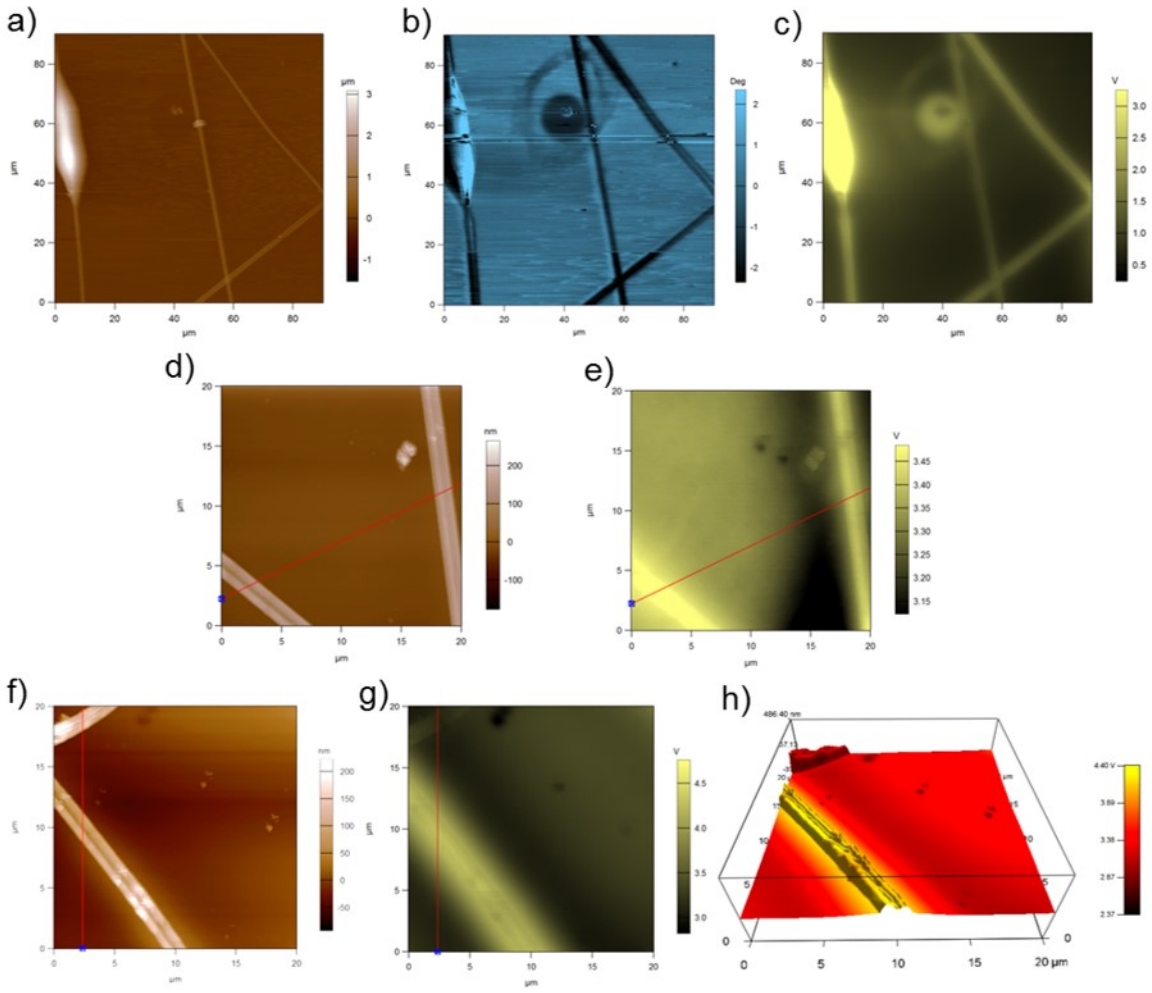

Figure 4-4: Examples of EFM/SKPM images of fiber composite samples. a-c) bare PLLA fibers: a) is the topography, b) is the phase of the Nap pass i.e. the EFM image; c) is the SKPM image of surface potential on the same region. d,e) and f-h): two regions of a samples of MWCNT composite fibers, (with combined topographic-potential rendering of the second region in h).

Finally, in Figure 4-5 the same region of the SKPM images in Figure 2-12 is shown again, when subsequently imaged in EFM mode. A substantial qualitative agreement in assignment of the filler regions appear in the phase of oscillation, Figure 4-5b, with SKPM surface potential image of Figure 2-12b, with only a reversal of contrast for the present signal, where the fillers appear as 'bright' phase regions, as compared to the 'dark' potential regions in Figure 2-12b. This is probably a mechanical effect due to the higher stiffness of the CNTs as compared to the PLLA fiber matrix. Also, the occasionally invasive effect of repeated scanning appears in Figure 4-5, as a suspended fiber having been picked by the scanning tip at some point during the scan and deflected (according to the arrow direction) up to forming a sharp right corner.

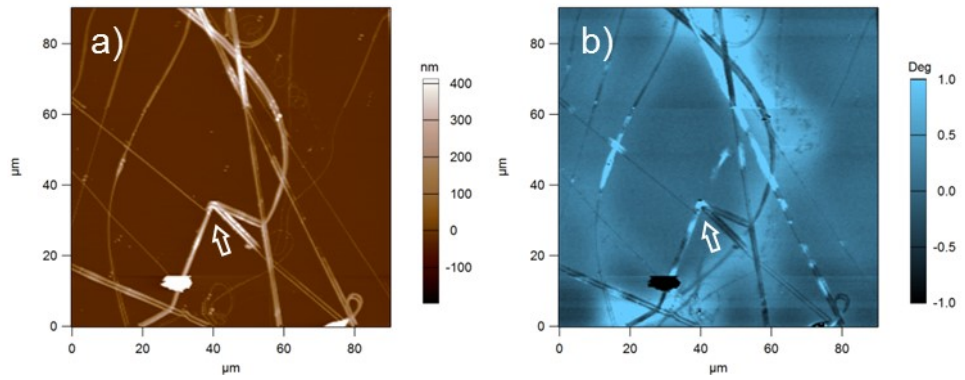

Figure 4-5: EFM images of the same region as shown in Figure 2-12; a) topography, b) phase of cantilever oscillation. Filler identification consistent with SKPM technique of Figure 2-12 emerges, along with demonstration of possible invasive tip-fiber interaction upon repeated scanning of the samples of deposited fibers.

For the roughness measurement, standard Tapping mode imaging with a standard (i.e. not metal coated) tip was carried out, not to degrade the spatial resolution of the images. Also, the S_q was calculated over surface areas of 20×20 µm^2, and averaged over five similar images from different regions of the samples.

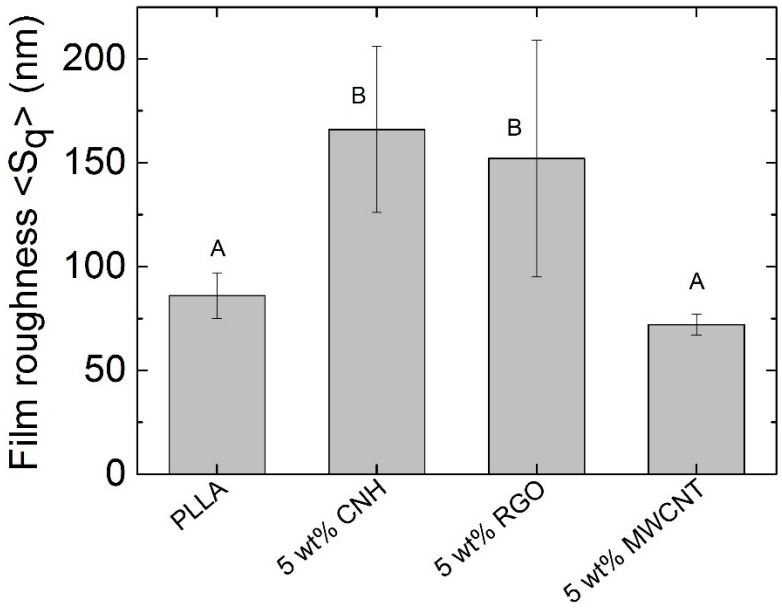

Figure 4-6: Root-mean-square of the height images, i.e. 2D roughness parameter Sq, for the films of different material composites (red columns), together with the bare PLLA (black column). The bars heights are the means, and the error bars extend ±1 standard error of the mean (SEM). The groups that present statistically significant differences (p<0.05) have been identified by different letter labels.

Cell death and proliferation assessment

Resazurin reduction assay was performed to quantify the metabolically active living cells and thus to monitor how do the scaffolds affect proliferation of the cell populations tested. The assay is based on reduction of the indicator dye, resazurin (not fluorescent), to the highly fluorescent resorufin (Ex. 569 nm, Em. 590 nm) by viable cells. Non-viable cells rapidly lose their metabolic capacity to reduce resazurin and, thus, do not produce fluorescent signals anymore. Briefly, the culture medium was replaced by 500 µL of resazurin solution (Resazurin Sigma 15 µg/mL in complete medium without phenol red) and cells were incubated for 4 h in dark at 37°C and 5% CO_2. Then, 200 µL of resazurin solution were removed twice from each well and transfer to a 96 well plate (technical duplicates). Fluorescence, directly correlated with cell quantity, was read in a plate reader (Ascent Fluoroscan, excitation 540 nm, emission 590 nm). Background values from wells without cells were subtracted and average values for the duplicates calculated. Cell proliferation was calculated from a calibration curve by linear regression using Microsoft Excel. The CytoTox-ONE™ Homogeneous Membrane Integrity Assay (Promega) was used to quantify the lactate dehydrogenase (LDH) release by cells having lost membrane integrity. Briefly, 100 µL of culture medium were transferred to a new 96 well plate. 50 µL of the reaction solution from the kit, containing the detection dye and the catalyst were then added to culture supernatants and fluorescence was measured after 10 minutes in the plate reader as reported above. Cell death was calculated from a calibration curve by linear regression after 100% cell lysis of known cell quantities.

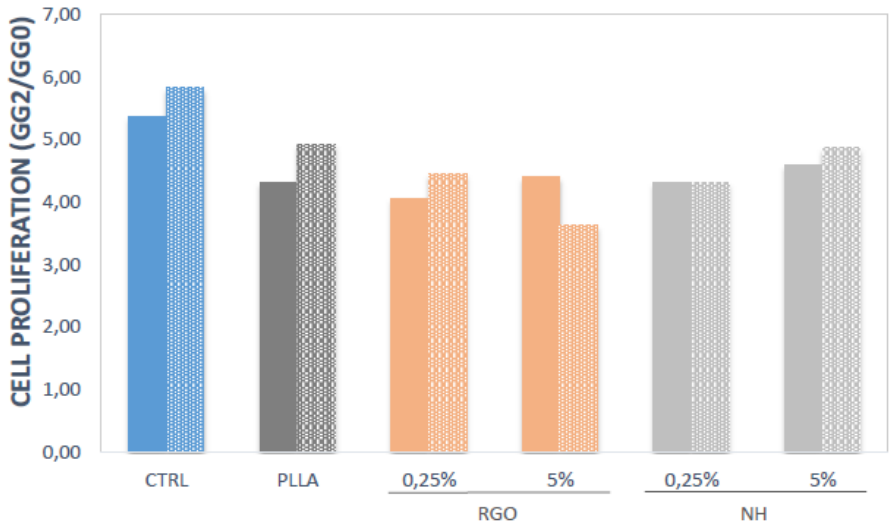

Figure 4-7: Cell proliferation on CNH@PLLA and RGO@PLLA films at 2 different CNSs concentrations. As reference are reported the results obtain for a polylisine coated control and for pure PLLA. All the experiment are performed both in absence (full bar) and in presence of retinoic acid (dotted bar).

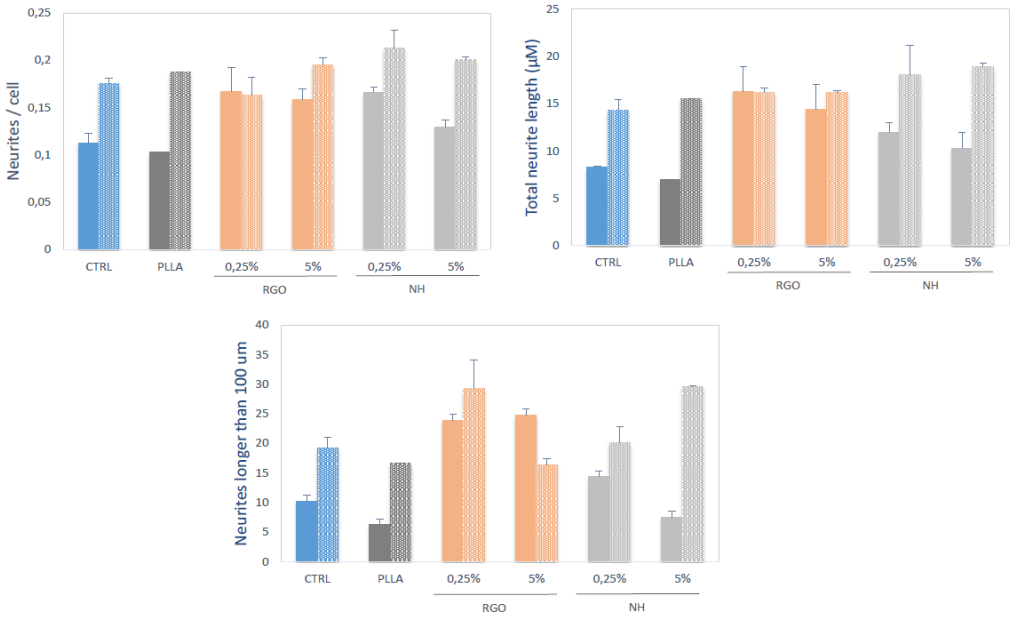

Figure 4-8: Morphological parameter evaluated on cells growing on CNH@PLLA and RGO@PLLA films at different concentration. As reference are reported the results obtain for a polylisine coated control and for pure PLLA. All the experiment are performed both in absence (full bar) and in presence of retinoic acid (dotted bar).

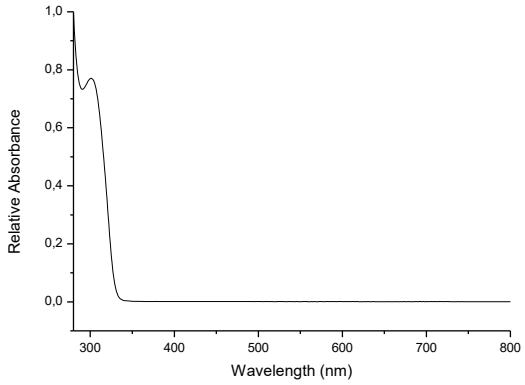

Figure 4-9: Uv-vis absorption spectrum of p-methoxyaniline in cyclohexane.

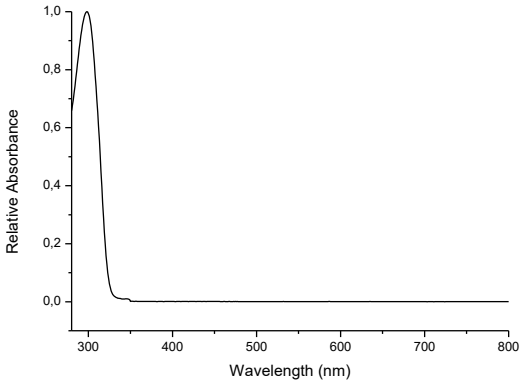

Figure 4-10: Uv-vis absorption spectrum of N,N-dimethylaniline in cycloexane.

Ringraziamenti

Inizio ovviamente con il ringraziare il Prof. E. Menna e la Prof. C. Marega per la loro gentile e importante supervisione iniziata con la mia tesi magistrale e continuata per questi tre anni di dottorato. Hanno sempre saputo guidarmi e spingermi nella giusta direzione e senza di loro nulla di tutto ciò che è stato fatto sarebbe stato possibile. Ringrazio quindi Giorgia, Tommaso e Sasha, i tre "colleghi" diventati subito grandi amici che hanno lavorato direttamente insieme a me a questo progetto. Il loro nome purtroppo è relegato solo qui quando invece potrebbe benissimo essere in copertina insieme al mio. Ci tengo quindi a ringraziare anche Patrizio, che è stato in grado di far sviluppare in me la grande passione per questo lavoro che mi ha consentito di arrivare fin qui e che porterò sempre con me. Infine voglio ringraziare tutte le persone che hanno collaborato e lavorato con me in questi anni a partire dai colleghi biotecnologi il Prof. F. Filippini, Yurico, Mattia e Giorgia continuando con Alex, il Prof L. Franco, il Dr. F. Sedona, il Prof. A. Moretto e il Prof. T. Carofiglio.

Bibliography

[1] S. Iijima, *Nature* **1991**, *354*, 56-58.
[2] N. Hamada, S.-i. Sawada and A. Oshiyama, *Physical Review Letters* **1992**, *68*, 1579-1581.
[3] E. Del Canto, K. Flavin, D. Movia, C. Navio, C. Bittencourt and S. Giordani, *Chemistry of Materials* **2011**, *23*, 67-74.
[4] E. Menna, F. Della Negra, M. Dalla Fontana and M. Meneghetti, *Physical Review B* **2003**, *68*, 193412.
[5] S. Niyogi, M. A. Hamon, H. Hu, B. Zhao, P. Bhowmik, R. Sen, M. E. Itkis and R. C. Haddon, *Accounts of Chemical Research* **2002**, *35*, 1105-1113.
[6] a) D. Tasis, N. Tagmatarchis, A. Bianco and M. Prato, *Chemical Reviews* **2006**, *106*, 1105-1136; b) C. Backes and A. Hirsch in *Noncovalent Functionalization of Carbon Nanotubes*, *Vol.* Eds.: T. Akasaka, F. Wudl and S. Nagase), John Wiley & Sons, Ltd, Chichester, UK. , **2010**, pp. 1-48; c) V. Georgakilas, M. Otyepka, A. B. Bourlinos, V. Chandra, N. Kim, K. C. Kemp, P. Hobza, R. Zboril and K. S. Kim, *Chem. Rev.* **2012**, *112*, 6156-6214; d) T. S. Sreeprasad and V. Berry, *Small* **2013**, *9*, 341-350; e) V. Georgakilas in *Covalent Attachment of Organic Functional Groups on Pristine Graphene*, *Vol.* Wiley-VCH Verlag GmbH & Co. KGaA, Weinheim, Germany, **2014**, pp. 21-58.
[7] Y. Lin, M. J. Meziani and Y.-P. Sun, *J. Mater. Chem.* **2007**, *17*, 1143-1148.
[8] V. Georgakilas, D. Voulgaris, E. Vázquez, M. Prato, D. M. Guldi, A. Kukovecz and H. Kuzmany, *J. Am. Chem. Soc.* **2002**, *124*, 14318-14319.
[9] a) M. A. Hamon, M. E. Itkis, S. Niyogi, T. Alvaraez, C. Kuper, M. Menon and R. C. Haddon, *J. Am. Chem. Soc.* **2001**, *123*, 11292-11293; b) L. Rodriguez-Perez, M. a. A. Herranz and N. Martin, *Chem. Commun.* **2013**, *49*, 3721-3735.
[10] a) M. Maggini, G. Scorrano and M. Prato, *J. Am. Chem. Soc.* **1993**, *115*, 9798-9799; b) V. Georgakilas, K. Kordatos, M. Prato, D. M. Guldi, M. Holzinger and A. Hirsch, *J. Am. Chem. Soc.* **2002**, *124*, 760-761; c) N. Tagmatarchis and M. Prato, *J. Mater. Chem.* **2004**, *14*, 437-439.
[11] a) P. Salice, P. Maity, E. Rossi, T. Carofiglio, E. Menna and M. Maggini, *Chemical Communications* **2011**, *47*, 9092-9094; b) M. Maggini, E. Menna, T. Carofiglio, E. Rossi, A. Pace and P. Salice in *Method for synthesis of functionalised carbon nanotubes by cycloaddition under continuous flow conditions and apparatus for the method*, *Vol. WO/2012/156297* **2012**; c) P. Salice, E. Rossi, A. Pace, P. Maity, T. Carofiglio, E. Menna and M. Maggini, *Journal of Flow Chemistry* **2014**, *4*, 79-85.
[12] F. E. Valera, M. Quaranta, A. Moran, J. Blacker, A. Armstrong, J. T. Cabral and D. G. Blackmond, *Angew. Chem.-Int. Edit.* **2010**, *49*, 2478-2485.
[13] a) J. L. Bahr, J. Yang, D. V. Kosynkin, M. J. Bronikowski, R. E. Smalley and J. M. Tour, *J. Am. Chem. Soc.* **2001**, *123*, 6536-6542; b) J. L. Bahr and J. M. Tour, *Chemistry of Materials* **2001**, *13*, 3823-3824; c) J. L. Hudson, M. J. Casavant and J. M. Tour, *Journal of the American Chemical Society* **2004**, *126*, 11158-11159; d) M. Castelain, P. S. Shuttleworth, C. Marco, G. Ellis and H. J. Salavagione, *Phys. Chem. Chem. Phys.* **2013**, *15*, 16806-16811.
[14] P. Salice, D. Fenaroli, C. C. De Filippo, E. Menna, G. Gasparini and M. Maggini, *Chemistry Today* **2012**, *30*, 37-39.
[15] a) K. P. Loh, Q. Bao, P. K. Ang and J. Yang, *J. Mater. Chem.* **2010**, *20*, 2277-2289; b) D. R. Dreyer, A. D. Todd and C. W. Bielawski, *Chem. Soc. Rev.* **2014**, *43*, 5288-5301.

[16] C. Gadermaier, E. Menna, M. Meneghetti, W. J. Kennedy, Z. V. Vardeny and G. Lanzani, *Nano Letters* **2006**, *6*, 301-305.
[17] a) E. Vázquez and M. Prato, *ACS Nano* **2009**, *3*, 3819-3824; b) F. Langa and P. de la Cruz in *Application of Microwave Irradiation in Carbon Nanostructures*, *Vol.* Wiley-VCH Verlag GmbH & Co. KGaA, **2012**, pp. 1059-1098; c) F. D. Negra, M. Meneghetti and E. Menna, *Fullerenes, Nanotubes and Carbon Nanostructures* **2003**, *11*, 25-34.
[18] M. S Strano, C. A Dyke, M. L Usrey, P. Barone, M. J Allen, H. Shan, C. Kittrell, R. Hauge, J. Tour and R. E Smalley, *Electronic Structure Control of Single-Walled Carbon Nanotube Functionalization*, **2003**, p. 1519-1522.
[19] M. R. Heinrich, *Chemistry – A European Journal* **2009**, *15*, 820-833.
[20] Q. H. Wang, C.-J. Shih, G. L. C. Paulus and M. S. Strano, *J. Am. Chem. Soc.* **2013**, *135*, 18866-18875.
[21] P. Salice, E. Fabris, C. Sartorio, D. Fenaroli, V. Figà, M. P. Casaletto, S. Cataldo, B. Pignataro and E. Menna, *Carbon* **2014**, *74*, 73-82.
[22] P. Salice, E. Fabris, C. Sartorio, D. Fenaroli, V. Figà, M. P. Casaletto, S. Cataldo, B. Pignataro and E. Menna, *Carbon* **2014**, *74*, 73-82.
[23] a) C. Backes, C. D. Schmidt, K. Rosenlehner, F. Hauke, J. N. Coleman and A. Hirsch, *Adv. Mater.* **2010**, *22*, 788-802; b) Y. Sun, W. Fu, Z. Li and Z. Wang, *Langmuir* **2014**, *30*, 8615-8620; c) A. Di Crescenzo, S. Cambré, R. Germani, P. Di Profio and A. Fontana, *Langmuir* **2014**, *30*, 3979-3987; d) H. Kato, A. Nakamura and M. Horie, *RSC Adv.* **2014**, *4*, 2129-2136.
[24] a) M. Zheng, A. Jagota, E. D. Semke, B. A. Diner, R. S. McLean, S. R. Lustig, R. E. Richardson and N. G. Tassi, *Nat Mater* **2003**, *2*, 338-342; b) G. Yu, L. Hu, N. Liu, H. Wang, M. Vosgueritchian, Y. Yang, Y. Cui and Z. Bao, *Nano Lett.* **2011**, *11*, 4438-4442; c) Y. Liu, C. Chipot, X. Shao and W. Cai, *J. Phys. Chem. B* **2010**, *114*, 5783-5789; d) P. Bilalis, D. Katsigiannopoulos, A. Avgeropoulos and G. Sakellariou, *RSC Advances* **2014**, *4*, 2911-2934; e) S. K. Samanta, M. Fritsch, U. Scherf, W. Gomulya, S. Z. Bisri and M. A. Loi, *Accounts of Chemical Research* **2014**, *47*, 2446-2456; f) R. Si, L. Wei, H. Wang, D. Su, S. H. Mushrif and Y. Chen, *Chem. Asian J.* **2014**, *9*, 868-877; g) C. Sciascia, R. Castagna, M. Dekermenjian, R. Martel, A. R. Srimath Kandada, F. Di Fonzo, A. Bianco, C. Bertarelli, M. Meneghetti and G. Lanzani, *J. Phys. Chem. C* **2012**, *116*, 19483-19489.
[25] H. Paloniemi, T. Ääritalo, T. Laiho, H. Liuke, N. Kocharova, K. Haapakka, F. Terzi, R. Seeber and J. Lukkari, *J. Phys. Chem. B* **2005**, *109*, 8634-8642.
[26] C. Ehli, D. M. Guldi, M. Angeles Herranz, N. Martin, S. Campidelli and M. Prato, *J. Mater. Chem.* **2008**, *18*, 1498-1503.
[27] D. R. Paul and L. M. Robeson, *Polymer* **2008**, *49*, 3187-3204.
[28] a) M. R. Bockstaller, R. A. Mickiewicz and E. L. Thomas, *Advanced Materials* **2005**, *17*, 1331-1349; b) S. S. Ray, *Macromolecular Chemistry and Physics* **2014**, *215*, 1162-1179; c) J. L. Suter, D. Groen and P. V. Coveney, *Adv. Mater.* **2015**, *27*, 966-984.
[29] a) P. Grady, *Carbon Nanotube-Polymer Composites: Manufacture, Properties, and Applications*, John Wiley & Sons, New York, **2011**, p. 352; b) R. Andrews and M. C. Weisenberger, *Current Opinion in Solid State and Materials Science* **2004**, *8*, 31-37; c) A. Schlierf, P. Samori and V. Palermo, *Journal of Materials Chemistry C* **2014**, *2*, 3129-3143; d) Z. Spitalsky, D. Tasis, K. Papagelis and C. Galiotis, *Progress in Polymer Science* **2010**, *35*, 357-401; e) H. Bai, C. Li and G. Shi, *Advanced Materials* **2011**, *23*, 1089-1115; f) D. Ponnamma, K. K. Sadasivuni, Y. Grohens, Q. Guo and S. Thomas, *Journal of Materials Chemistry C* **2014**,

2, 8446-8485; g) K. Hu, D. D. Kulkarni, I. Choi and V. V. Tsukruk, *Progress in Polymer Science* **2014**, *39*, 1934-1972.
[30] P. M. Ajayan, O. Stephan, C. Colliex and D. Trauth, *Science* **1994**, *265*, 1212-1214.
[31] V. Thavasi, G. Singh and S. Ramakrishna, *Energy & Environmental Science* **2008**, *1*, 205-221.
[32] S. Agarwal, J. H. Wendorff and A. Greiner, *Polymer* **2008**, *49*, 5603-5621.
[33] D. Liang, B. S. Hsiao and B. Chu, *Advanced Drug Delivery Reviews* **2007**, *59*, 1392-1412.
[34] D. Garlotta, *Journal of Polymers and the Environment* **2001**, *9*, 63-84.
[35] P. Pan and Y. Inoue, *Progress in Polymer Science* **2009**, *34*, 605-640.
[36] S. Wang, Y. Zhang, H. Wang, G. Yin and Z. Dong, *Biomacromolecules* **2009**, *10*, 2240-2244.
[37] a) T. Dvir, B. P. Timko, D. S. Kohane and R. Langer, *Nat Nano* **2011**, *6*, 13-22; b) J. Thiele, Y. Ma, S. M. C. Bruekers, S. Ma and W. T. S. Huck, *Advanced Materials* **2014**, *26*, 125-148.
[38] a) N. Bhattarai, J. Gunn and M. Zhang, *Advanced Drug Delivery Reviews* **2010**, *62*, 83-99; b) B. L. Banik and J. L. Brown in *Chapter 23 - Polymeric Biomaterials in Nanomedicine*, *Vol.* (Ed. S. G. K. T. L. Deng), Elsevier, Oxford, **2014**, pp. 387-395.
[39] a) G. Southard and G. Murray in *Molecularly Imprinted Polymer Receptors for Sensors and Arrays*, *Vol.* (Ed. M. Zourob), Springer New York, **2010**, pp. 751-775; b) Z. Wang and Z. Dai, *Nanoscale* **2015**, *7*, 6420-6431.
[40] a) M. Shahinpoor in *Chapter 6 - Muscular Biopolymers*, *Vol.* Eds.: A. Lakhtakia and R. J. Martín-Palma), Elsevier, Boston, **2013**, pp. 139-160; b) L. G. Gómez-Mascaraque, R. Palao-Suay and B. Vázquez in *12 - The use of smart polymers in medical devices for minimally invasive surgery, diagnosis and other applications*, *Vol.* Eds.: M. R. Aguilar and J. S. Román), Woodhead Publishing, **2014**, pp. 359-407.
[41] E. Ruiz-Hitzky, M. Darder, P. Aranda and K. Ariga, *Advanced Materials* **2010**, *22*, 323-336.
[42] A. Battigelli, C. Menard-Moyon and A. Bianco, *Journal of Materials Chemistry B* **2014**, *2*, 6144-6156.
[43] a) S. Bhattacharya and S. K. Samanta, *Chemical Reviews* **2016**, *116*, 11967-12028; b) Z. Spitalsky, D. Tasis, K. Papagelis and C. Galiotis, *Progr. Polym. Sci.* **2010**, *35*, 357-401; c) A. Sherif, M. Qingshi, Z. Liqun, Z. Izzuddin, M. Peter and M. Jun, *Nanotechnology* **2015**, *26*, 112001; d) M. Wang, X. Duan, Y. Xu and X. Duan, *ACS Nano* **2016**, *10*, 7231-7247; e) J. Du and H.-M. Cheng, *Macromol. Chem. Phys.* **2012**, *213*, 1060-1077.
[44] a) Z. Jun Han, A. E. Rider, M. Ishaq, S. Kumar, A. Kondyurin, M. M. M. Bilek, I. Levchenko and K. Ostrikov, *RSC Advances* **2013**, *3*, 11058-11072; b) C. Chung, Y.-K. Kim, D. Shin, S.-R. Ryoo, B. H. Hong and D.-H. Min, *Acc. Chem. Res.* **2013**, *46*, 2211-2224; c) W. Nakanishi, K. Minami, L. K. Shrestha, Q. Ji, J. P. Hill and K. Ariga, *Nano Today* **2014**, *9*, 378-394; d) E. L. Hopley, S. Salmasi, D. M. Kalaskar and A. M. Seifalian, *Biotechnology Advances* **2014**, *32*, 1000-1014; e) S. Goenka, V. Sant and S. Sant, *Journal of Controlled Release* **2014**, *173*, 75-88; f) M. Nurunnabi, K. Parvez, M. Nafiujjaman, V. Revuri, H. A. Khan, X. Feng and Y.-k. Lee, *RSC Adv.* **2015**, *5*, 42141-42161.
[45] a) A. Bianco, *Angewandte Chemie International Edition* **2013**, *52*, 4986-4997; b) M. Ghiazza, G. Vietti and I. Fenoglio in *8 - Carbon nanotubes: properties, applications, and toxicity*, *Vol.* Eds.: J. Njuguna, K. Pielichowski and H. Zhu), Woodhead Publishing, **2014**, pp. 147-174.

[46] a) J. Di, X. Wang, Y. Xing, Y. Zhang, X. Zhang, W. Lu, Q. Li and Y. T. Zhu, *Small* **2014**, *10*, 4606-4625; b) M. C. Serrano, M. C. Gutiérrez and F. del Monte, *Progress in Polymer Science* **2014**, *39*, 1448-1471.
[47] a) S. Attal, R. Thiruvengadathan and O. Regev, *Analytical Chemistry* **2006**, *78*, 8098-8104; b) S. H. Jeong, K. K. Kim, S. J. Jeong, K. H. An, S. H. Lee and Y. H. Lee, *Synthetic Metals* **2007**, *157*, 570-574.
[48] S. M. Bachilo, M. S. Strano, C. Kittrell, R. H. Hauge, R. E. Smalley and R. B. Weisman, *Science* **2002**, *298*, 2361-2366.
[49] M. S. Dresselhaus, G. Dresselhaus, R. Saito and A. Jorio, *Physics Reports* **2005**, *409*, 47-99.
[50] N. Vicentini, T. Gatti, P. Salice, G. Scapin, C. Marega, F. Filippini and E. Menna, *Carbon* **2015**, *95*, 725-730.
[51] a) T. Gatti, N. Manfredi, C. Boldrini, F. Lamberti, A. Abbotto and E. Menna, *Carbon* **2017**, *115*, 746-753; b) T. Gatti, S. Casaluci, M. Prato, M. Salerno, F. Di Stasio, A. Ansaldo, E. Menna, A. Di Carlo and F. Bonaccorso, *Advanced Functional Materials* **2016**, *26*, 7443-7453.
[52] Z.-J. Zhang, W. Cui, H. Xu, L. Xie, H. Liu, L.-M. Zhu, H. Li and R. Ran, *RSC Advances* **2015**, *5*, 16604-16610.
[53] M. Kaseem, K. Hamad, F. Deri and Y. G. Ko, *Polymer Bulletin* **2016**, 1-17.
[54] B. W. Chieng, N. A. Ibrahim, W. M. Z. Wan Yunus, M. Z. Hussein and Y. Y. Loo, *Journal of Thermal Analysis and Calorimetry* **2014**, *118*, 1551-1559.
[55] M. Moniruzzaman and K. I. Winey, *Macromolecules* **2006**, *39*, 5194-5205.
[56] N. K. Shrivastava and B. B. Khatua, *Carbon* **2011**, *49*, 4571-4579.
[57] P. Salice, C. Sartorio, A. Burlini, R. Improta, B. Pignataro and E. Menna, *Journal of Materials Chemistry C* **2015**, *3*, 303-312.
[58] S. Gnavi, B. E. Fornasari, C. Tonda-Turo, G. Ciardelli, M. Zanetti, S. Geuna and I. Perroteau, *Materials Science and Engineering: C* **2015**, *48*, 620-631.
[59] J. Landers, J. T. Turner, G. Heden, A. L. Carlson, N. K. Bennett, P. V. Moghe and A. V. Neimark, *Advanced Healthcare Materials* **2014**, *3*, 1745-1752.
[60] a) V. Lovat, D. Pantarotto, L. Lagostena, B. Cacciari, M. Grandolfo, M. Righi, G. Spalluto, M. Prato and L. Ballerini, *Nano Letters* **2005**, *5*, 1107-1110; b) E. Lizundia, J. R. Sarasua, F. D'Angelo, A. Orlacchio, S. Martino, J. M. Kenny and I. Armentano, *Macromolecular Bioscience* **2012**, *12*, 870-881.
[61] a) Y.-S. Chen and G.-H. Hsiue, *Biomaterials* **2013**, *34*, 4936-4944; b) L. Bareket-Keren and Y. Hanein, *Front. Neural Circuits* **2013**, *6*, 122.
[62] D. Debanne, E. Campanac, A. Bialowas, E. Carlier and G. Alcaraz, *Physiological Reviews* **2011**, *91*, 555-602.
[63] a) G. Tamir, B.-D. Moti, K. Itshak, S. Raya, R. A. Ze'ev, B.-J. Eshel and H. Yael, *Nanotechnology* **2007**, *18*, 035201; b) E. W. Keefer, B. R. Botterman, M. I. Romero, A. F. Rossi and G. W. Gross, *Nat Nano* **2008**, *3*, 434-439.
[64] a) J. H. Lee, J.-Y. Lee, S. H. Yang, E.-J. Lee and H.-W. Kim, *Acta Biomaterialia* **2014**, *10*, 4425-4436; b) H. Hu, Y. Ni, V. Montana, R. C. Haddon and V. Parpura, *Nano Letters* **2004**, *4*, 507-511; c) T. Gabay, E. Jakobs, E. Ben-Jacob and Y. Hanein, *Physica A: Statistical Mechanics and its Applications* **2005**, *350*, 611-621.
[65] M. A. Tischfield, H. N. Baris, C. Wu, G. Rudolph, L. Van Maldergem, W. He, W.-M. Chan, C. Andrews, J. L. Demer, R. L. Robertson, D. A. Mackey, J. B. Ruddle, T. D. Bird, I. Gottlob, C.

Pieh, E. I. Traboulsi, S. L. Pomeroy, D. G. Hunter, J. S. Soul, A. Newlin, L. J. Sabol, E. J. Doherty, C. E. de Uzcátegui, N. de Uzcátegui, M. L. Z. Collins, E. C. Sener, B. Wabbels, H. Hellebrand, T. Meitinger, T. de Berardinis, A. Magli, C. Schiavi, M. Pastore-Trossello, F. Koc, A. M. Wong, A. V. Levin, M. T. Geraghty, M. Descartes, M. Flaherty, R. V. Jamieson, H. U. Møller, I. Meuthen, D. F. Callen, J. Kerwin, S. Lindsay, A. Meindl, M. L. Gupta Jr, D. Pellman and E. C. Engle, *Cell* **2010**, *140*, 74-87.
[66] L. Dehmelt and S. Halpain, *Genome Biology* **2004**, *6*, 204.
[67] G. Scapin, T. Bertalot, N. Vicentini, T. Gatti, S. Tescari, V. De Filippis, C. Marega, E. Menna, M. Gasparella, P. P. Parnigotto, R. Di Liddo and F. Filippini, *Nanomedicine* **2016**, *11*, 1929-1946.
[68] a) T. Jiang, E. J. Carbone, K. W. H. Lo and C. T. Laurencin, *Progress in Polymer Science* **2015**, *46*, 1-24; b) K. M. Oprych, R. L. D. Whitby, S. V. Mikhalovsky, P. Tomlins and J. Adu, *Advanced Healthcare Materials* **2016**, *5*, 1253-1271.
[69] a) S. H. Oh, J. R. Kim, G. B. Kwon, U. Namgung, K. S. Song and J. H. Lee, *Tissue Engineering. Part C, Methods* **2013**, *19*, 233-243; b) D. Arslantunali, T. Dursun, D. Yucel, N. Hasirci and V. Hasirci in *Peripheral nerve conduits: technology update*, *Vol. 7* **2014**, pp. 405-424.
[70] M. Yang, K. Flavin, I. Kopf, G. Radics, C. H. A. Hearnden, G. J. McManus, B. Moran, A. Villalta-Cerdas, L. A. Echegoyen, S. Giordani and E. C. Lavelle, *Small* **2013**, *9*, 4194-4206.
[71] G. Scapin, P. Salice, S. Tescari, E. Menna, V. De Filippis and F. Filippini, *Nanomedicine: Nanotechnology, Biology and Medicine* **2015**, *11*, 621-632.
[72] W. Zhang, A. Nefedov, M. Naboka, L. Cao and C. Woll, *Physical Chemistry Chemical Physics* **2012**, *14*, 10125-10131.
[73] Y.-C. Chiang, W.-H. Lin and Y.-C. Chang, *Applied Surface Science* **2011**, *257*, 2401-2410.
[74] S. Campestrini, C. Corvaja, M. De Nardi, C. Ducati, L. Franco, M. Maggini, M. Meneghetti, E. Menna and G. Ruaro, *Small* **2008**, *4*, 350-356.
[75] B. L. Bales, M. Meyer, S. Smith and M. Peric, *The Journal of Physical Chemistry A* **2008**, *112*, 2177-2181.
[76] J. M. Yuan, Z. F. Fan, X. H. Chen, X. H. Chen, Z. J. Wu and L. P. He, *Polymer* **2009**, *50*, 3285–3291.
[77] M. Radtke and A. Ignaszak, *Electroanalysis* **2016**, *28*, 2900-2909.
[78] M. S. Strano, C. A. Dyke, M. L. Usrey, P. W. Barone, M. J. Allen, H. Shan, C. Kittrell, R. H. Hauge, J. M. Tour and R. E. Smalley, *Science* **2003**, *301*, 1519-1522.
[79] W. B. Smith and O. C. Ho, *The Journal of Organic Chemistry* **1990**, *55*, 2543-2545.
[80] E. Sawicki, *The Journal of Organic Chemistry* **1957**, *22*, 915-919.
[81] B. F. Day, T. W. Campbell and G. M. Coppinger, *Journal of the American Chemical Society* **1951**, *73*, 4687-4688.
[82] N. Chen, M. Barra, I. Lee and N. Chahal, *The Journal of Organic Chemistry* **2002**, *67*, 2271-2277.
[83] H. Adibi, M. B. Majnooni, A. Mostafaie, K. Mansouri and M. Mohammadi, *Iranian Journal of Pharmaceutical Research : IJPR* **2013**, *12*, 695-703.
[84] R. A. Ross, B. A. Spengler and J. L. Biedler, *JNCI: Journal of the National Cancer Institute* **1983**, *71*, 741-747.